# Semiconductor Growth on an Oxide Using a Metallic Surfactant and Interface Studies for Potential Gate Stacks from First Principles

Dissertation
zur Erlangung des Grades
eines Doktors der Naturwissenschaften

vorgelegt von

**Andrei Reyes Huamantinco**
aus Moskau

genehmigt von der
Fakultät für Natur- und Materialwissenschaften
der Technische Universität Clausthal

Tag der mündlichen Prüfung:
09. Mai 2008

Die Arbeit wurde angefertigt am Institut für Theoretische Physik
der Technischen Universität Clausthal.

Vorsitzender der Promotionskommission: Prof. Dr. Albrecht Wolter

Hauptberichterstatter: Prof. Dr. Peter E. Blöchl

Berichterstatter: Prof. Dr. Tom Kirchner

Reyes Huamantinco, Andrei Datum:

# EIDESSTATTLICHE ERKLÄRUNG

Hiermit erkläre ich an Eides Statt, dass die eingereichte Dissertation weder in Teilen noch in Ihrer Gesamtheit einer anderen Hochschule zur Begutachtung vorliegt oder vorgelegen hat und dass ich bisher noch keinen Promotionsversuch unternommen habe.

Unterschrift

Hiermit erkläre ich an Eides Statt, dass ich die bei der Fakultät für Material- und Naturwissenschaften der Technischen Universität Clausthal eingereichte Dissertation selbständig und ohne unerlaubte Hilfe verfasst und die benutzten Hilfsmittel vollständig angegeben habe.

Datum: Unterschrift

*to my mum Alicia, my dad José, grandpa Andrés,*
*and grandmas Petronila and Rosa*

*"... I equate the rational attitude (towards a problem of the natural sciences or philosophy) and the critical attitude. The point is that whenever we try to propose a solution to a problem, we ought to try as hard as we can to overthrow our solution, rather than defend it. Few of us, unfortunately, practise this precept; but other people, fortunately, will supply the criticism for us if we fail to supply it ourselves. Yet criticism will be fruitful only if we state our problem as clearly as we can and put our solution in a sufficiently definite form-a form in which it can be critically discussed."*

***Karl Raimund Popper*, The Logic of Scientific Discovery, *1959***

# Acknowledgements

To Prof. Dr. Peter E. Blöchl for giving me the great opportunity to work in a challenging project (the European Project IST-ET4US "Epitaxial Technologies for Ultimate Scaling"), which allowed me to interact closely with experienced experimental researchers and to participate in fruitful scientific meetings.

To Dr. Marco Fanciulli, Dr. Alessandro Molle, Dr. Kabir Bhuiyan and Dr. Grazia Tallarida from the Laboratorio MDM-INFM Milan for the valuable scientific exchange regarding their experimental studies on germanium epitaxial growth on strontium hafniate.

To Dr. Athanasios Dimoulas, Dr. Jean Fompeyrine, and Dr. Maria Seo, scientific partners in the ET4US Project, for valuable discussions on the germanium epitaxial growth on strontium hafniate.

To Dr. Christophe Rossel from the IBM Laboratory in Zurich for the invitation that gave me the opportunity to discuss my work with him and his colleagues.

To Dr. Clemens Först and Dr. Christopher Ashman for guiding me through the initial stages of my work and life in Clausthal with care and generosity.

To the members of my group, Christian Walter, Sascha Hemmen, Alexander Poddey, Sineng Sun, Emanuel Hofmann, Daniel Grieger, for valuable help and enjoyable moments in and out of the institute, and especially to Dr. Jürgen Noffke and our secretary Frau Frömmel for continuous support and care during the time of my studies. To the members of the IT-Team, Axel Ehrich, Björn Drude, Benjamin Lüken, Dennis Harig, Sandra Bergmann for continuous support with computer-related issues.

To Dr. Luis Fernandez Menchero for providing an enjoyable environment in the office we share, and for his patience.

To Prof. Dr. Tom Kirchner for many enjoyable discussions and valuable advice.

To the members of Prof. Kirchner's group, especially Matthias Popp and Tobias Spranger, for many enjoyable moments and help.

To Clausthal University of Technology for providing me with good working conditions.

To the Norddeutsche Verbund für Hoch und Höchstleistungsrechner for providing me with adequate amounts of computer time during the entire period of my studies, and to Dr. Kallies for his continuous advice on the efficient use of their computational resources.

To the many people that have accompanied me during the length of my studies for making life in Clausthal much more enjoyable and for helping me to discover myself. Especially to Heiko Liebhart, Raul Cecilia, Tilman Antons, Gerald Schenk, Llorenc Taus, Henry Mangkusasono for their beautiful friendship.

To my girlfriend Eva Nutz for her partnership, support and wisdom, that allowed me to stay focused on my work and other important aspects of life.

Finally, I would like to thank my family for their continuous support, you are my strength and inspiration in life.

# Abstract

In this work the epitaxial growth of germanium on $SrHfO_3(001)$, and the $La_2Hf_2O_7$/Si(001) and $SrTiO_3$/GaAs(001) interfaces were studied theoretically using the *Projector-Augmented Wave* (PAW) method. The studied systems have great technological interest in the context of the development of future transistors. The PAW method is based on *Density Functional Theory* and it is implemented in the Car-Parrinello Ab-Initio Molecular Dynamics. It is an *all-electron* method that treats explicitly the core and valence electrons and gives access to the complete (also close to the nucleus) wave function.

The goal of the germanium growth on $SrHfO_3(001)$ is to form a germanium film with low density of defects and smooth morphology, to be used as channel in a transistor. Such a film can not be formed by direct growth due to the fact that germanium grows in three dimensional islands on the oxide substrate. Therefore, in this work, the feasibility of using a third material to achieve germanium layer-by-layer growth was investigated. It was found that antimony does not wet the oxide substrate and therefore can not be used to initiate epitaxial growth of germanium. On the other hand, strontium is an interesting candidate, since previous studies have demonstrated that 1/2ML passivates the Si(001) surface. The formation of an ordered strontium film on a SrO-terminated oxide substrate, to be used as template for germanium overgrowth, was studied. It was found that careful control of the experimental conditions, in a growth chamber where the only sources are strontium and germanium, may lead to the formation of a strontium 1ML film. On the other hand, the formation of an ordered 1/2ML film is unlikely. The strontium 1ML film increases the surface reactivity, and it is important to avoid oxidation because it leads to germanium clustering. It has been found that oxidation from the oxide subsurface is thermodynamically unfavorable. However, insignificant oxygen contamination in the growth chamber is necessary. Deposition of germanium on the strontium 1ML template results in wetting and thus a change of the growth mode to layer-by-layer. A germanium adatom binds strongly to the surface at the hollow site. Moreover, germanium remains at the surface and does not diffuse into the substrate

below. Nevertheless, the diffusion barrier of germanium on the strontium surface is larger than the atomization energy of the strontium film, so that germanium diffusion can not be activated at coverages up to 1/4ML. Under these growth conditions, the formation of a uniform 1/4ML film is not possible and regions with lower and higher coverage coexist on the surface. At coverages higher than 1/2ML, the Ge adatoms occupy the hollow sites but also form short chains. The short chain structure is stable at 3/4ML coverage, and it is part of the first and second layers of the Ge(001) 2ML film. Therefore, the first germanium epitaxial layers do not form in a layer-by-layer fashion. Moreover, it has been found that at germanium coverages between 1ML and 2ML, (interfacial) strontium atoms from the template diffuse to the germanium surface. The germanium surface is then passivated and a germanium compound is initially formed with strontium at the surface and interface. At this stage, a thermal treatment may be beneficial for the formation of a uniform germanium film on the oxide substrate. Finally, at 3ML coverage, the obtained stable surface configuration consists of a germanium epitaxial film passivated on both surfaces by strontium 1/2ML. Therefore, during germanium deposition, the strontium 1ML template has separated into two halves: 1/2ML has segregated to the surface and the remaining 1/2ML forms the interface. The strontium 1/2ML-interface has unpinned Fermi level and its calculated band offsets are suitable for transistor applications. On the germanium surface, the strontium 1/2ML film may in principle be used as surfactant, since it passivates the Ge(001) surface and it is expected to have low incorporation in bulk germanium due to the large atomic radius of strontium. Furthermore, the strontium film may also be used as template for heteroepitaxial growth of a strontium-based perovskite on Ge(001).

The interfacial structure and valence band offsets of the $La_2Hf_2O_7$/Si(001) crystalline system were studied. It was found that the $La_3HfO_5$ class of interfaces unpin the Fermi level. A surface structure with a large relaxation of an interfacial oxygen atom into the oxide has a calculated valence band offset of $1.81 \pm 0.27$ eV. On the other hand, a degenerate structure without the interfacial oxygen relaxation and with a different relative orientation of the silicon substrate, has an estimated valence band offset of $2.37 \pm 0.02$ eV. The large difference in the band offset is due to the electric dipole perpendicular to the interface originated by the relaxation of the interfacial oxygen atom. Both valence band offsets are larger than 1 eV, which is a suitable value for transistor applications. This study indicates that a variety of interfacial structures may coexist, moreover, the calculated valence band offsets overlap with the experimental data for the amorphous system.

The $SrTiO_3$/GaAs(001) crystalline interfaces with unpinned Fermi level

were investigated. It was found that the unoxidized Sr 1/4ML interface has a valence band offset of $0.97 \pm 0.25$ eV, and the oxidized Sr 3/4ML interface, a valence band offset of $1.53 \pm 0.25$ eV. The atomic structure of the latter interface is qualitatively similar to the experimental Z-contrast image for the crystalline system.

# Contents

# Chapter 1

# Introduction

Metal-oxide-semiconductor-field-effect-transistors (MOSFETs) are at the heart of today's computers, but also at the heart of today's society and lifestyle. Modern transportation, communications, commerce and entertainment depend on computers. The development of MOSFETs and microelectronics has been fast and continuous during the last few decades providing cheaper, faster, smaller and less power consuming transistors. The so-called mobile technology is a direct consequence of this development and it has had a profound impact on society, revolutionizing the way we interact with other people. Today's society demands for further improvement of the MOSFETs performance to satisfy its growing computational needs. But is there a limit for this improvement? In 1965, Gordon Moore [1] reviewed the then current state of development in microelectronics and proposed a development trend for semiconductor integrated circuit technology. This trend is known today as Moore's law, and predicts that the shrinking of the transistor's dimensions and the improvement of its performance approach a linear dependence with time. Nowadays the International Technology Roadmap for Semiconductors [2] dictates the new trends and technologies in the semiconductor industry. The apparently unlimited performance improvement of a MOSFET has indeed a limit imposed by quantum mechanical effects. To clarify the reason for this limitation it is necessary to have a general idea of the operation of a MOSFET.

## 1.1 The MOS capacitor and the MOSFET

A traditional metal-oxide-semiconductor (MOS) capacitor (Figure 1.1) consists of a silicon (Si) substrate, a silicon dioxide film ($SiO_2$), and a metal plate. Its operation is similar to that of a capacitor with the metal plate and

the Si substrate being the metal plates of the capacitor. The substrate is not made of pure Si but it is alloyed (doped) with small quantities of another material that can act as an electron acceptor (e.g. boron, aluminum, gallium) or an electron donor (phophorous, arsenic, antimony). Depending on the type of material that dopes the Si substrate it is called p-type (acceptor-like doping) or n-type (donor-like doping). The p-type substrate has a majority of holes as charge carriers, whereas in the n-type, the electrons are the charge carriers. Additionally, there are two zones in the substrate which are doped with the opposite type of materials as the substrate, and they are called source and drain. So, when a voltage is applied on the metal plate it will affect electrostatically the substrate surface and charge carriers can accumulate at or be repelled from the substrate. If a voltage is then applied between the source and drain during accumulation of charges at the substrate surface, the MOSFET is on the "off state" and there is no charge transport between the source and drain. On the other hand, if the majority charges are repelled from the surface substrate an inversion layer can form with the minority carriers which are of the same type as the source and drain, and the the MOSFET will be on the "on state". The gate dielectric, $SiO_2$, must isolate the charge carriers in the two metal plates of the MOSFET capacitor, diffusion through the gate dielectric must not occur.

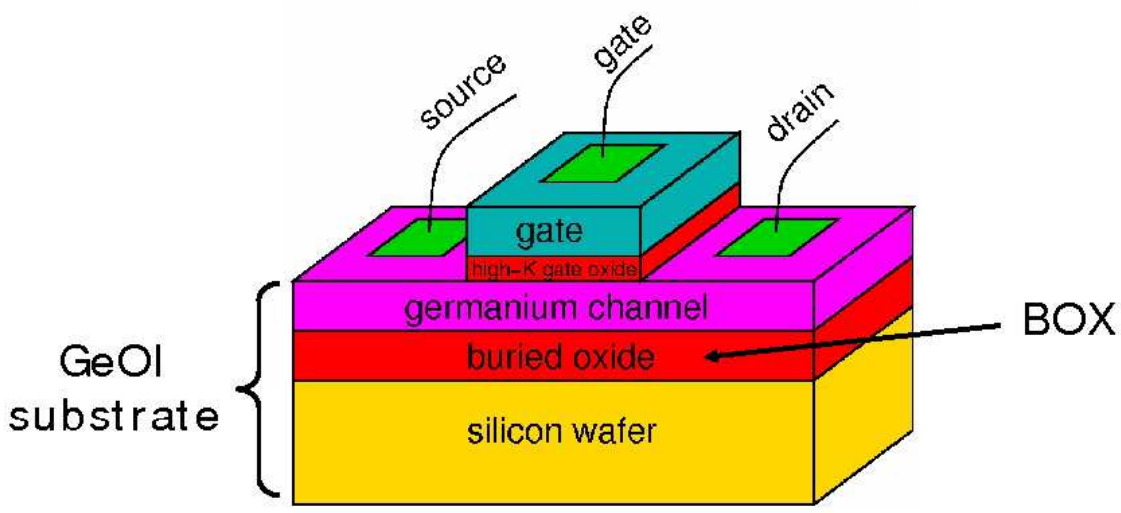


Figure 1.1: Scheme of a metal-oxide-semiconductor field effect transistor (MOSFET). The germanium on insulator (GeOI) architecture is shown, which includes a buried oxide (BOX) below the channel.

Since the reduction of the MOSFET dimensions is necessary for better performance, there is a potential problem when the thickness of the gate dielectric is too small so that electrons can tunnel through due to quantum mechanical effects. In order to avoid this without sacrificing scalability, it has been proposed the use of gate dielectrics with higher dielectric constant than $SiO_2$ (3.9), and they are the so-called high-k dielectrics. The advantage is that the thickness of the gate dielectric can be increased while the capacitance of the MOSFET is maintained. A challenge for the high-k materials is integration with Si and Ge in the MOSFET.

## 1.2 High mobility channels

In addition to high-k dielectrics, the performance of the MOSFET can in principle be improved when a material with higher mobility than Si is used in the channel. Ge seems to be better suited for transistors than Si. It has better transport properties than Si which allows for higher saturation currents, and a smaller band gap which translates to lower supply voltages and power dissipation [3]. In fact, it was used in the first transistors but it was abandoned due to difficulties in processing Ge oxide [3]. The high optical absorption coefficient of Ge makes it also suitable for photodetectors and optoelectronics [4]. Another advantage is that the lattice parameter is compatible with GaAs which opens the road to integration of both materials in a CMOSFET.

## 1.3 GeOI substrates for MOSFETs

Semiconductor-on-insulator (SeOI) substrates place an insulating oxide material between the channel and the substrate, the so-called buried-oxide (BOX). The BOX insulates the channel from the substrate and the transistor from adjacent transistors. SeOI substrates offer better electrostatic control for MOSFETs over conventional 'bulk' substrates due to less short channel effects, reduced junction capacitances and lower substrate coupling in radio frequency [3]. The SeOI architecture also offers the possibility to integrate Ge or GaAs to be used in the channel with existing low-cost and widely available Si substrates. In this way, the current Si-wafer processing lines may continue to be exploited in the production of future MOSFETs. When a material other than Si is used in the channel, such as Ge or GaAs, the BOX can be used to adjust the lattice mismatch between the Si substrate and the channel.

Ge-on-insulator (GeOI) substrates use a Ge channel on a Si substrate, and so benefit from the Ge transport properties (Section 1.2) and lattice parameter similar to GaAs. The GeOI substrate can be used as template for high-quality epitaxial growth of GaAs enabling Si/III-V monolithic integration. In these substrates a limited quantity of Ge is used providing mechanical stability over fragile and heavy Ge bulk substrates. The mechanical behaviour is close to Si wafer giving GeOI a practical advantage for processing in the current Si device lines. It has also been found that GeOI substrates have better heat dissipation by the Si substrate beneath, even with the BOX layer in-between, compared to Ge and GaAs substrates [4].

One of the main challenges in GeOI substrates for MOSFETs is to create a high-quality single-crystal layer for the channel material. A promising technique for achieving this goal is heteroepitaxial growth. A significant misfit strain exists between Si and Ge (4 %) that makes direct heteroepitaxy challenging but, on the other hand, the strain in the Ge channel is desirable because it can be used to optimize the carrier transport properties. Thus, the goal for a GeOI-based MOSFET device is to have a highly strained Ge channel with minimal density of crystal defects [5].

Successful Ge p-channel mobility enhancement has been reported much more often than significant enhancement in n-channel mobility (see Ref. [4] and references therein). This is a generally found limitation in Ge, and possible causes include: insufficient Ge surface passivation, poor dopant activation in S/D regions, impurity induced structural defects. In order to improve the n-channel mobility, strained Si or GaAs can be used instead of Ge in the same structure with a Ge p-channel, to form a dual channel heterostructure.

## 1.4 Growth Modes

There are three growth modes: Franck-van der Merwe or layer-by-layer, Volmer-Weber or 3D-island, and Stranski Krastanov. They depend on the wetting and strain conditions of the film on the substrate. If the film wets the substrate, layer-by-layer or Stranski-Kastranov growth modes are possible. The difference between the two is the strain condition on the growing layer. Under high strain (or compressive strain) a film that initially growed in a layer-by-layer mode (due to favorable wetting) can change to 3D-island growth in order to relax the strain in the film, e.g. Ge growth on Si (lattice mismatch is 4 %). If the film does not wet the substrate, it grows in 3D-islands to minimize the surface energy, e.g. Si growth on Ge.

It can be seen that Ge wets Si but Si does not wet Ge, similarly, the oxides used as gate dielectrics wet Si, on the other hand, Si grows in 3D-islands on

these oxides. This can be understood using a surface energy argument. If material $A$ is deposited on $B$, and if $\gamma_A$, $\gamma_B$, and $\gamma_{AB}$ are the surface energy of material A (interface $A$/vacuum), material B (interface $B$/vacuum), and interfacial energy between material $A$ and $B$. Then a layer-by-layer growth mode is expected when $\gamma_A + \gamma_{AB} < \gamma_B$. If this condition is satisfied, and $A$ (e.g. gate oxide) does grow layer-by-layer on $B$ (e.g. Si), then unless $\gamma_{AB}$ is a negative number, $B$ will grow in 3D-islands on $A$, since $\gamma_A < \gamma_B$.

## 1.5 GeOI fabrication techniques

Nowadays there are several fabrication techniques for GeOI substrates. The most widely used are the Ge condensation technique [6] and the Smart-Cut process. Other methods include liquid phase epitaxy [7], the bond and grinding method, the grind and etch-back method.

The Ge condensation technique consists basically of two steps: the epitaxial growth of a SiGe layer on a SOI substrate, followed by selective oxidation of Si. This Si selective oxidation is performed under dry $O_2$ and at high temperature. The result is the accumulation of Ge at the oxide interface and simultaneously, due to the high temperature used, Ge diffusion through the top Si layer of the SOI substrate and then through the remaining SiGe layer [6]. The thickness of the SiGe layer decreases during oxidation due to Si consumption. The decrease in SiGe thickness and the diffusion of Ge produce a Ge content enrichment. Enrichments up to 100 % in ultra thin SGOI layers (about 10 nm), for long-enough oxidation times, have been reported [3]. In the Ge condensation technique, initial parameters have a drastic influence on the final enrichment values and the final SGOI or GeOI thicknesses. These initial parameters are: the top Si thickness of the starting SOI wafer, the Ge content in the deposited SiGe layer and the SiGe thickness before oxidation. In addition, the final properties of the GeOI substrate are also sensitive to physical non-homogeneities induced in the prestructure fabrication, such as the uniformity of the Si and SiGe thicknesses and of the Ge content. At the current state of development, line density of dislocations ($18/\mu$ m) and low surface roughness ($\approx$ 0.4 nm Rms) characterize the Ge condensation technique [4]. The main advantage of this technique is its localized approach. It allows for Si and Ge-on-insulator co-integration, and it is adequate for very thin GeOI formation. Among the drawbacks are its high thermal budget ($> 1000\,^{\circ}$C), and plastic deformation during the oxidation process [4].

The Smart-Cut process is based on wafer bonding and uses two wafers, one is a Si wafer and the other, called donor wafer, contains the Ge layer to be transferred. The basic process flow for GeOI fabrication consists of:

oxide formation on the Si wafer, ion implantation on the (donor) wafer that contains the Ge layer, hydrophilic bonding of the two wafers, Ge film transfer by mechanical separation from the donor wafer, and finishing steps [4]. After the process is finished, the donor wafer can be reutilized to fabricate additional GeOI substrates. This is an efficient method for SOI fabrication and has been adapted for 'full sheet' (not-localized, continuous Ge film) GeOI fabrication. The quality of the donor wafer plays an important role because it contains the starting material for layer transfer. The Ge layer in the donor wafer should have minimum defectivity. The donor wafer can be a Si wafer where Ge has been grown or else a Czochralski-grown Ge bulk wafer with zero dislocations. Although the Ge bulk donor wafers offer ideal crystal quality for GeOI, the heterostructure produced after bonding has a thermal mismatch that increases with the wafer diameter. GeOI fabrication from Ge bulk donor wafers has been demonstrated for 200 mm wafers with low surface roughness (below 0.5 nm Rms) and without detection of extended defects [4]. However, future availability of 300 mm Ge bulk donor wafers, necessary for high performance MOSFET applications, is still not clear.

Liquid phase epitaxy (LPE) is yet another technique. It starts by sputter deposition of Ge on the oxide substrate followed by rapid thermal annealing (RTA) above the melting temperature of Ge. The oxide is deposited on the Si wafer but does not cover it completely and so Ge is also in contact with Si. The natural cooling down of Ge initiates the process. The LPE starts at the seed region in contact with the Si substrate and proceeds to the region on the insulator. The crystal orientation of the Ge film is then determined by the orientation of the Si substrate. Typically, the lateral extent of GeOI fabricated with this technique is limited to $20\mu m$ [4].

None of the currently used GeOI fabrication techniques is based on direct heteroepitaxial growth due to the fact that Ge grows on an insulator in a Volmer-Weber mode, that is forming 3D-islands (Section 1.4). Although after certain thickness the Ge islands do coalesce, the resulting density of defects in the film is too high for transistor applications. Nevertheless, it is still possible to attempt to obtain a metastable epitaxial structure by affecting growth kinetics through low temperature growth or high deposition rate. Moreover, it is possible, in principle, to change the growth mode to layer-by-layer through the use of a third material during heteroepitaxial growth, called surfactant. In the past, Sb and As have been used as surfactants to achieve layer-by-layer growth for the fabrication of Ge/Si heterostructures [8, 9]. The general effect of surfactants is discussed in Section 3.7. The choice of a suitable surfactant that is compatible both with Ge and the oxide substrate is investigated in this work.

# Chapter 2

# Theoretical Approach

## 2.1 Introduction

In this section I will describe the theoretical approach used in my simulations, and I begin by mentioning briefly some aspects of the theories used by the computational approach. The complete description of a many-particle interacting system (electrons and atomic nuclei) requires the quantum mechanical treatment of the electronic and nuclear parts of the system. As a consequence of the great difference between the masses of the electrons and nuclei, the Born-Oppenheimer approximation [10] (or adiabatic approximation) allows to separate the scales of time of the electronic and nuclear movements. Therefore, it is assumed that the (fast) electrons possess enough time to readjust and therefore follow the movement of the (slow) nuclei, so in each instantaneous nuclear configuration, the electrons are always in their ground state. This is equivalent to a *parametric* evolution of the ground state, which depends (parametrically) on the instantaneous nuclear configuration.

The Born-Oppenheimer approximation separates the electronic and nuclear degrees of freedom in such a way that it is possible to introduce an effective classical nuclear system. In this system, the nuclear movements can be treated classically. The forces acting on the nuclei are determined by the electrons in the ground state, and can be obtained from the Born-Oppenheimer *potential energy surface* (PES). The PES describes the total energy $E$ as function of the nuclear configuration $\{\vec{R}_I\}$. The total energy $E$ represents the potential energy of the nuclear system, and it is the sum of the electronic total energy and the nucleus-nucleus repulsion energy. The forces obtained from the PES are used to integrate the classic equations of motion for the nuclei and, in this way, generate a new nuclear configuration. The dynamic evolution of the system on the PES is called Born-Oppenheimer

dynamics. The equilibrium geometry is the global minimum (on the PES) of the total energy $E$ with respect to the nuclear configuration.

## 2.2 Density-Functional Theory

The theoretical study of the electronic structure (for a fixed nuclear configuration) requires the solution of only one Schrödinger equation for the system of interacting electrons in an "external" potential $v(\vec{r})$ originating from the nuclei. The many-electron wave function of the ground state (solution corresponding to the lowest eigenvalue of this Schrödinger equation), allows for the determination of all the electronic properties of the ground state [11]. For the description of the ground state, a theory exists that uses the electronic density $\rho(\vec{r})$ as basic variable, instead of the many-electron wave function. This theory is the *density-functional theory* (DFT) that was introduced by Hohenberg and Kohn [12] in 1964. DFT greatly simplifies calculations of the electronic structure and significantly reduces the computational cost, especially for systems with large number of particles.

The first Hohenberg and Kohn theorem [12] (according to the order given by Parr and Yang [11]) enunciates that the external potential is determined, up to a trivial additive constant, by the electronic density of the ground state. Since $\rho(\vec{r})$ also determines the number of electrons, then, it determines the Hamiltonian of the system. Consequently, $\rho(\vec{r})$ determines the many-electron wave function of the ground state and all of the electronic properties of the system, in particular, the total energy. In this way, the (electronic) total energy is a functional of the density and it is constituted by a term of kinetic energy, a term of electron-electron repulsion (potential) energy and a term of electron-nucleus attraction (potential) energy. Among them, the kinetic energy and the electron-electron repulsion are defined independently of the external potential and, therefore, together form a *universal* functional of the density, that does not depend on the studied system.

The second theorem of Hohenberg and Kohn [12] enunciates that the minimum of the total energy (the energy of the ground state), is obtained for the density of the ground state. This is a variational principle and it allows for the calculation of the density by minimizing the total energy (functional of the density), whenever the *universal* functional is known exactly. Unfortunately, the exact explicit form of this functional is not known.

The Kohn and Sham formulation of the DFT [13] (1965) translates the problem of the electronic structure of a system of interacting electrons to a system of non-interacting electrons, and both systems possess exactly the same electronic density of the ground state $\rho(\vec{r})$. This *effective* sys-

tem of $N$ non-interacting electrons moving in an *effective* external potential $v_{ef}(\vec{r})$ has a Hamiltonian that is the sum of $N$ one-electron Hamiltonians, $\hat{H}_s = \sum_{i=1}^{N}(-\frac{1}{2}\nabla_i^2 + v_{ef}(\vec{r}_i))$, where electron-electron repulsion terms do not exist [11]. The density of this system is constructed from the first $N$ eigenfunctions of the one-electron Hamiltonian $\mathcal{H}^{\mathcal{KS}}$:

$$\mathcal{H}^{\mathcal{KS}}\psi_i(\vec{r}) = \left\{ -\frac{1}{2}\nabla^2 + v_{ef}(\vec{r}) \right\}\psi_i(\vec{r}) = \varepsilon_i\psi_i(\vec{r}), \tag{2.1}$$

where the *Kohn-Sham effective potential (KS)* is defined as:

$$v_{ef}(\vec{r}) = \int d\vec{r'}\frac{\rho(\vec{r'})}{|\vec{r} - \vec{r'}|} + v_{xc}(\vec{r}) + v(\vec{r}), \tag{2.2}$$

with the *exchange-correlation potential*:

$$v_{xc}(\vec{r}) = \frac{\delta E_{xc}[\rho]}{\delta\rho(\vec{r})}, \tag{2.3}$$

and the electronic density of the ground state is determined by:

$$\rho(\vec{r}) = \sum_{i=1}^{N}|\psi_i(\vec{r})|^2, \tag{2.4}$$

with the restriction:

$$N = \int d\vec{r}\rho(\vec{r}). \tag{2.5}$$

$i$ represents any group of appropriate quantum numbers, $v(\vec{r})$ is the external potential of the original system and $E_{xc}$ is the exchange-correlation energy, both are functionals of the density. The set of equations, Eqs. (2.1), (2.2) and (2.4), should be solved self-consistently and they are known as the *Kohn-Sham equations*. The KS eigenfunctions $\{\psi_i\}$ are called KS orbitals and they are orthonormal $\langle\psi_i|\psi_j\rangle = \delta_{ij}$. In this chapter, atomic units are used (unless otherwise indicated), $e^2 = \hbar = m = 1$, where $e$ is the charge of the electron, $\hbar$ is the Planck constant and $m$ is the mass of the electron.

The (electronic) total energy KS, of the ground state, can be written as:

$$\begin{aligned} E^{KS}[\rho] = &\sum_{i=1}^{N}\int d\vec{r}\psi_i^*(\vec{r})(-\frac{1}{2}\nabla^2)\psi_i(\vec{r}) + \frac{1}{2}\int\int d\vec{r}d\vec{r'}\frac{\rho(\vec{r})\rho(\vec{r'})}{|\vec{r} - \vec{r'}|} \\ &+ E_{xc}[\rho] + \int d\vec{r}v(\vec{r})\rho(\vec{r}). \end{aligned} \tag{2.6}$$

The first term is the kinetic energy of the system of non-interacting electrons and contains most of the kinetic energy of the original system. The second term, called the Hartree energy, is the (classic) electrostatic repulsion energy of a charge distribution interacting with itself. The third term, the exchange-correlation energy, contains the corrections for the first two terms of Eq. (2.6) with respect to kinetic and electron-electron repulsion energies of the original system. The last term is the electron-nucleus attraction energy, considering that the external potential $v(\vec{r})$ is fixed (fixed nuclear configuration). $E^{KS}$ is also known as the KS (total energy) functional.

The minimization of the $E^{KS}$ energy, Eq. (2.6), with respect to the density and with fixed $N$, Eq. (2.5), or with respect to the KS orbitals subject to the orthonormality restriction, generates the Kohn-Sham equations [11].

The Kohn-Sham equations are exact and produce the exact density. The exact $v_{ef}(\vec{r})$ potential can be considered as the fictitious and unique potential that when acting on the system of non-interacting electrons produces the same density $\rho(\vec{r})$ of the system of interacting electrons in the external potential $v(\vec{r})$ [14]. In practice, the Kohn-Sham equations of the non-interacting system are much easier to solve than the Schrödinger equation of the original system, especially when the number of electrons is large. Nevertheless, the $E_{xc}[\rho(\vec{r})]$ functional is not exactly known and has to be approximated. Commonly used approximations for $E_{xc}[\rho(\vec{r})]$ are the *local-density approximation* [13] (LDA) that uses information about $\rho$ in each point of the space and the *generalized gradient approximation* (GGA) that uses information about $\rho$ and the gradient $|\nabla\rho|$.

In a rigorous treatment of the electronic and nuclear variables, consistent with the Born-Oppenheimer approximation, the temporal evolution of the electronic variables, $\psi_i(\vec{r};t)$, would be determined by the solution of: $\mathcal{H}^{\mathcal{KS}}(t)\psi_i^{KS}(\vec{r};t) = \varepsilon_i(t)\psi_i^{KS}(\vec{r};t)$, where the temporal dependence of $\mathcal{H}^{\mathcal{KS}}$ originates from the slow nuclear evolution, which in turn is determined by the Newton's equations: $M_I\ddot{\vec{R}}_I = \vec{F}_I = -\frac{\partial U^{KS}}{\partial \vec{R}_I}$. $U^{KS}$ is the minimum of the total energy $E[\rho] = E^{KS}[\rho] + E_{n-n}$, equal the KS electronic total energy, Eq. (2.6), plus the nucleus-nucleus repulsion energy[1].

[1]The nucleus-nucleus repulsion energy can be added to $E^{KS}$ after the selfconsistent calculation of the Kohn-Sham equations or else it can be included in the definition of $\mathcal{H}^{\mathcal{KS}}$; the total energy $E$ will be the same [11].

# 2.3 Car and Parrinello *Ab Initio* Molecular Dynamics

## 2.3.1 Introduction

The *ab initio* molecular dynamics simulates the Born-Oppenheimer dynamics calculating *ab initio* the electronic structure of the ground state for each nuclear configuration (at each time step). However, the selfconsistent solution to the electronic structure problem for each time step has a high computacional cost. An alternative approach to perform *ab initio* molecular dynamics simulations was presented by Car and Parrinello [15] (AIMD). The AIMD approach uses the DFT [12], in the Kohn-Sham formulation [13], to describe the instantaneous electronic structure. And the Newton equations of motion to approximate by a *classic dynamic* evolution the *parametric* evolution of the electronic $\{\psi_i\}$ and nuclear $\{\vec{R}_I\}$ variables. It is important to note that the KS orbitals $\psi_i(\vec{r};t)$, and not the electrons, are considered as classic variables.

From the computacional point of view, this approach provides a very efficient algorithm because, in the evolution of the electronic variables, it is not necessary to minimize $E$ (i.e. selfconsistent calculation of the electronic structure) for each subsequent nuclear configuration. The dynamic evolution of the nuclear system generated by the AIMD approximates well an evolution with conserved energy (of the classic system), and the forces that act on the nuclei are indistinguishable from those obtained from the PES, whenever an adiabatic decoupling exists between the electronic and nuclear variables [16] (Section 2.3.3). On the other hand, the equilibrium geometry can be obtained using the technique of simulated annealing (Section 2.3.4).

## 2.3.2 Fictitious Lagrangean and Equations of Motion

In the AIMD approach, the classic dynamic evolution of the electronic and nuclear variables is described by the Lagrangean[2]:

$$\begin{aligned}\mathcal{L}_{\mathcal{CP}} = \frac{1}{2}\sum_I M_I \dot{\vec{R}}_I^2 + \sum_i m_\psi f_i \langle\dot{\psi}_i|\dot{\psi}_i\rangle - E[\{\vec{R}_I\},\{\psi_i\}] \\ + \sum_{i,j}\Big(\langle\psi_i|\psi_j\rangle - \delta_{ij}\Big)\Lambda_{ji}. \qquad (2.7)\end{aligned}$$

[2]The extension of the Kohn-Sham formulation to variable occupation numbers $\{f_i\}$ (introduced by Janak [17]) has been used; these occupation numbers have the Fermi-Dirac distribution.

The first term is the kinetic energy of the nuclei, with masses $M_I$ and velocities $\dot{\vec{R}}_I$. The second term is the *fictitious* (classic) kinetic energy of the electronic wave functions (taking into account the double occupation of the $\psi_i$). This quantity is called fictitious because it is not related to the physical quantum kinetic energy. $m_\psi$ is a (fictitious) mass parameter, $f_i$ is the occupation number of the $\psi_i$, and $\dot{\psi}_i$ is the time derivative of the wave function. The third term is the total energy $E = E^{KS} + E_{n-n}$, which is a functional of $\{\psi_i\}$ and $\{\vec{R}_I\}$, and represents the potential energy for this classic system. The last term is an orthonormality constraint for the wave functions, implemented using the technique of Lagrange multipliers $\Lambda_{ji}$[3].

The Lagrangean $\mathcal{L}_{\mathcal{CP}}$ is also known as the fictitious Lagrangean due to the inclusion of the fictitious dynamics of the $\{\psi_i\}$ in the Born-Oppenheimer Lagrangean [18]: $\mathcal{L}_{\mathcal{BO}} = \frac{1}{2}\sum_I M_I \dot{\vec{R}}_I^2 - E[\{\vec{R}_I\}, \rho]$.

The equations of motion resulting from $\mathcal{L}_{\mathcal{CP}}$ are:

$$M_I \ddot{\vec{R}}_I = -\frac{\partial E[\{\vec{R}_I\}, \{\psi_i\}]}{\partial \vec{R}_I} = -\nabla_I E[\{\vec{R}_I\}, \{\psi_i\}] = \vec{F}_I, \tag{2.8}$$

$$m_\psi |\ddot{\psi}_i\rangle = \frac{1}{f_i}\left[ -\frac{\delta E[\{\vec{R}_I\}, \{\psi_i\}]}{\delta \langle\psi_i|} + \sum_j |\psi_j\rangle \Lambda_{ji} \right] = -\mathcal{H}^{\mathcal{KS}} |\psi_i\rangle + \frac{1}{f_i}\sum_j |\psi_j\rangle \Lambda_{ji}. \tag{2.9}$$

These coupled equations describe the *simultaneous* evolution of the nuclear, $\{\vec{R}_I\}$, and electronic, $\{\psi_i\}$, variables. At each time step, the $\{\vec{R}_I\}$ evolve due to forces $\vec{F}_I$ obtained from the instantaneous electronic structure and, simultaneously, the $\{\psi_i\}$ evolve adapting to the instantaneous nuclear configuration. Thus, the total energy $E$ is not explicitly minimized through selfconsistency cycles at each time step.

In a molecular dynamics simulation, the total energy of the (classic) system should remain constant. From the definition of $\mathcal{L}_{\mathcal{CP}}$, Eq. (2.7), it is possible to identify a constant of motion of the system ($\{\vec{R}_I\}$ and $\{\psi_i\}$), which is the total energy:

$$\begin{aligned} E_{cons} &= \frac{1}{2}\sum_I M_I \dot{\vec{R}}_I^2 + \sum_i f_i \langle\dot{\psi}_i| m_\psi |\dot{\psi}_i\rangle + E[\{\vec{R}_I\}, \{\psi_i\}] \\ &= T_n + T_\psi + E = E_{fis} + T_\psi. \end{aligned} \tag{2.10}$$

[3]This constraint does not perform work on the system and does not originate dissipation [16].

$T_n$ is the physical kinetic energy of the nuclei, $T_\psi$ is the fictitious temperature of the wave functions, and $E_{fis}$ is the physical energy of the nuclear and electronic system (note that it corresponds to the total energy of the system described by $\mathcal{L}_{\mathcal{BO}}$). The conservation of $E_{cons}$ does not have a direct physical interpretation.

Whenever $T_\psi \ll E_{fis}$, then $E_{fis}$ will be almost constant. And so it is possible to approximate a microcanonical molecular dynamics ($E_{fis} = const$) that will simulate the nuclear trajectories if the forces $\vec{F}_I$, Eq. (2.8), are very close to the (exact) forces obtained from the PES.

In the following, I will describe briefly the way the forces on the nuclei $\vec{F}_I$, Eq. (2.8), are calculated when a basis of plane waves is used. If the Hellmann-Feynman theorem [19] is used: $\nabla_I E[\{\vec{R}_I\}, \{\psi_i\}] = \nabla_I \langle \Psi | \mathcal{H} | \Psi \rangle = \langle \Psi | \nabla_I \mathcal{H} | \Psi \rangle$, where $\mathcal{H}$ is the Hamiltonian of the electronic system (it can also be $\mathcal{H}^{\mathcal{KS}}$) and $\Psi$ is an eigenfunction of $\mathcal{H}$ (that determines the exact density $\rho$). In an *ab initio* calculation, corrections should be added to the Hellmann-Feynman force. One correction is due to the use of a (finite) incomplete basis and the other, due to the non-selfconsistency of $\rho$ [20]. The first correction, also known as Pulay force, disappears when the calculated eigenfunction is exact or when the basis that expands the eigenfunctions does not depend on the nuclear coordinates $\{\vec{R}_I\}$, for instance, a basis of plane waves. The second correction does not need to be evaluated when the electronic and nuclear degrees of freedom evolve simultaneously [20], as it is the case in AIMD. Therefore, the forces $\vec{F}_I$ can be calculated using the Hellmann-Feynman theorem, when the AIMD and a basis of plane waves are used.

### 2.3.3 Molecular Dynamics and Adiabatic Decoupling

A AIMD simulation is performed by numerically integrating Eqs. (2.8) and (2.9), starting from an initial nuclear configuration $\vec{R}_I(t = 0)$ with the electronic system the closest possible to the ground state $\psi_i(\vec{r}; t = 0)$, and appropriate initial conditions for the velocities $\dot{\vec{R}}_I(0)$ and $\dot{\psi}_i(\vec{r}; 0)$. In order to simulate the physical dynamics of the nuclei at a fixed temperature, the electronic wave functions have to remain very close to the PES (of the ground state) at all times. Thus, in a AIMD simulation, the system ($\{\vec{R}_I\}$ and $\{\psi_i\}$) should remain in a state with two independent temperatures: the temperature of the eletronic variables (fictitious, associated with $T_\psi$), that should be very low to approximate the ground state, and the (physical) temperature of the nuclei [15]. Thus the nuclear and electronic variables should remain

adiabatically decoupled during the simulation.

In systems with large energy gap, a AIMD simulation (with appropriate choice of the time step) determines an energy $E_{cons}$ that is well conserved and an energy $E_{fis}$ that oscillates with a very small amplitude around the mean value (which remains constant within the precision of the integration algorithm). Thus, on average, the dynamics of the nuclei maintains $E_{fis}$ constant. This oscillation originates from $T_\psi$ (which represents the "agitation" of $\{\psi_i\}$), and can be divided into two components, one of low frequency that corresponds to the synchronization with the vibration frequency of the nuclei, and another of high frequency (superimposed) originating from the intrinsic dynamics of the $\{\psi_i\}$ [16]. The high frequency oscillations correspond to the oscillations of the electronic degrees of freedom (the coefficients of the expansion of $\{\psi_i\}$ in a basis) around the instantaneous ground state, which represents the energy minimum for the sub-system of the $\{\psi_i\}$. These oscillations are originated by the change in position of the ground state (in the PES) as a result of the evolution of the $\{\vec{R}_I\}$. The high frequency oscillations allow the $\{\psi_i\}$ to follow the slow evolution of the nuclear variables, remaining on average very close to the ground state, and also allow the irreversible energy transfer among $\{\psi_i\}$ and $\{\vec{R}_I\}$ to be slow. Since also the forces $\vec{F}_I$ depend continually on $\{\psi_i\}$, Eq. (2.8), they also show oscillations of low and high frequency around the correct value from the PES, with the deviations being very small and oscillatory. In metals, the transfer of energy is very difficult to control because there is no energy gap. In this cases, a method that controls the temperatures of $\{\psi_i\}$ and $\{\vec{R}_I\}$ can be used, for instance, the thermostats method of Blöchl and Parrinello [21].

In order to produce physical results through AIMD simulations over long periods of time, the irreversible energy transfer should be slow. This energy transfer thermically balances the $\{\psi_i\}$ and $\{\vec{R}_I\}$, in other words, it heats up $\{\psi_i\}$ (detachment from the PES) and it cools $\{\vec{R}_I\}$ (departure from the physical temperature of the simulation).

### 2.3.4 Equilibrium Geometry: Simulated Annealing

For the calculation of the equilibrium geometry (the nuclear configuration whose energy in the PES is a global minimum), AIMD uses the technique of simulated annealing [15]. In this technique, the minimum of the total energy $E[\{\vec{R}_I\},\{\psi_i\}]$ is obtained by quenching the $\{\psi_i\}$ ($T_\psi$) and $\{\vec{R}_I\}$ ($T_n$) to temperatures close to zero.

To remove kinetic energy from the system (to reduce the temperature), classic constants of friction are coupled to the equations of motion:

$$M_I\ddot{\vec{R}}_I = -\frac{\partial E[\{\vec{R}_I\},\{\psi_i\}]}{\partial \vec{R}_I} - \alpha_R M_I \dot{\vec{R}}_I, \tag{2.11}$$

$$m_\psi|\ddot{\psi}_i\rangle = -\mathcal{H}^{\mathcal{KS}}|\psi_i\rangle + \frac{1}{f_i}\sum_j |\psi_j\rangle\Lambda_{ji} - \alpha_\psi m_\psi|\dot{\psi}_i\rangle, \tag{2.12}$$

where $M_I\alpha_R$ and $m_\psi\alpha_\psi$ are the constants of friction for the $\{\vec{R}_I\}$ and $\{\psi_i\}$, respectively. By varying $\alpha_R$ and $\alpha_\psi$ it is possible to control the quenching of the system.

Note that when the system has been totally quenched, $\ddot{\psi}_i = 0$. Consequently, Eq. (2.9) is identical to the Kohn-Sham equations by a unitary transformation[4] (the resulting equation represents the minimization of $E[\rho]$ with respect to the KS orbitals under the orthonormality constraint), and the eigenvalues of the $\Lambda_{ji}$ matrix coincide with the KS eigenvalues [15]. It is essential to first bring the electrons to the ground state before releasing the atoms.

## 2.4 The PAW Method

### 2.4.1 Introduction

The Projector-Augmented Wave (PAW) method developed by Blöchl [22] is an *ab initio all-electron* method, within the formalism of the DFT [12], and the Kohn-Sham formulation [13]. An *all-electron* (AE) approach treats explicitly *all* the electrons (core and valence) of the system and gives access to the *complete* wave function (in the whole space), called AE wave function. This is essential for the calculation of properties that depend on the electronic density in the area close to the nucleus, such as hyperfine parameters; see

[4]The KS orbitals are obtained applying an appropriate unitary transformation to the calculated $\{\psi_i\}$ [18]

Petrilli *et al.* [23] for an application of the PAW method to the calculation of electric field gradients in the nucleus.

The AE wave function is the KS orbital, $|\psi_i\rangle$, and has a characteristic form in different areas of the space. Close to the nucleus, it oscillates very fast due to the strong attractive potential of the nucleus and it has a nodal structure. Far away from the nucleus, in the interstitial area (also called the bonding region), it is smooth. Therefore, it is convenient to expand $|\psi_i\rangle$ in an appropriate basis in each area of the space.

In PAW, the AE wave function is expanded in different bases inside and outside the *augmentation* region, $\Omega_I$, centered in the atom[5]: outside $\Omega_I$, in plane waves and, inside of $\Omega_I$, in fixed partial waves that are imported from atomic (isolated atom) calculations. To achieve this, the PAW method builds the AE wave functions $|\psi_i\rangle$ from *pseudo* wave functions $|\tilde{\psi}_i\rangle$, which extend over the whole space and are smooth. Since they are smooth, they can be calculated using a basis of plane waves, and subsequently *transformed* into $|\psi_i\rangle$. The PAW method can be implemented in the Car and Parrinello *ab initio* molecular dynamics, taking advantage of the use of a basis of plane waves.

In this section, I will describe the important aspects of the method, all the details can be found in the original work of Blöchl (whose nomenclature is used here) [22].

### 2.4.2 Construction of the Wave Functions

The essence of the PAW method lies in the three-component construction of the AE wave functions, $|\psi_i\rangle$, using the *pseudo* wave functions $|\tilde{\psi}_i\rangle$:

$$|\psi_i\rangle = |\tilde{\psi}_i\rangle + \sum_k |\phi_k\rangle\langle\tilde{p}_k|\tilde{\psi}_i\rangle - \sum_k |\tilde{\phi}_k\rangle\langle\tilde{p}_k|\tilde{\psi}_i\rangle. \tag{2.13}$$

The first term, $|\tilde{\psi}_i\rangle$, is the *pseudo* wave function. $|\tilde{\psi}_i\rangle$ is smooth and extends over the whole space, so it can be represented as an expansion in plane waves. The second term represents the expansion of $|\psi_i\rangle$ in AE partial waves, $|\phi_k\rangle$, with coefficients $\langle\tilde{p}_k|\tilde{\psi}_i\rangle$. The $|\phi_k\rangle$ are the solutions of the Schrödinger equation for the isolated atom (Section 2.4.5). The third term represents the expansion of $|\tilde{\psi}_i\rangle$ in *pseudo* partial waves, $|\tilde{\phi}_k\rangle$, also with coefficients $\langle\tilde{p}_k|\tilde{\psi}_i\rangle$. The $|\tilde{\phi}_k\rangle$ are built using an approach analogous to the pseudopotential approach in the isolated atom (Section 2.4.5), and they are identical to the $|\phi_k\rangle$ outside the *augmentation* region $\Omega_I$. The $\langle\tilde{p}_k|$ are the *projector* functions (or

[5]The *augmentation* region corresponds to the atomic or *muffin-tin* sphere of the linear methods [24] and to the core area of the pseudopotential methods [25].

simply *projectors*) that determine the coefficients of the expansions in partial waves; this coefficients are the same for both expansions (Section 2.4.4). The $|\phi_k\rangle$, $|\tilde{\phi}_k\rangle$ and $|\tilde{p}_k\rangle$ are fixed functions, and they are not affected by the selfconsistent process during the calculation of $|\tilde{\psi}_i\rangle$.

The index of the sum $k$ refers to the atomic sites $I$, to the angular momentum quantum numbers per site $l$ and $m$, and to the number of partial waves per angular momentum per site $n$, that is, $k \equiv I, l, m, n$. Eq. (2.13) is valid only for valence electrons, the core electrons are treated in a similar way (see next Section below).

It is interesting to analyze the contribution of each term in Eq. (2.13) to the AE wave functions $|\psi_i\rangle$:

1. The first term $|\tilde{\psi}_i\rangle$, the *pseudo* wave function, is identical to the AE wave function outside $\Omega_I$, and a smooth continuation inside[6].

2. The second term is the expansion of $|\psi_i\rangle$ in AE partial waves $|\phi_k\rangle$ (centered at the site $I$). For an incomplete (but converged) basis set, this term should provide a good description of $|\psi_i\rangle$ only inside $\Omega_I$ and a poor description outside.

3. The third term is the expansion of $|\tilde{\psi}_i\rangle$ in *pseudo* partial waves $|\tilde{\phi}_k\rangle$ (centered at the site $I$). Similar to the second term, when using an incomplete (but converged) basis set, it should describe well the $|\tilde{\psi}_i\rangle$ only inside $\Omega_I$ and poorly outside.

4. Outside $\Omega_I$, the second and third terms cancel because the $|\phi_k\rangle$ are identical to the $|\tilde{\phi}_k\rangle$ by construction and the coefficients of the expansions in partial waves are the same.

$$\sum_k |\tilde{\phi}_k\rangle\langle\tilde{p}_k|\tilde{\psi}_i\rangle = \sum_k |\phi_k\rangle\langle\tilde{p}_k|\tilde{\psi}_i\rangle \qquad \text{outside } \Omega_I \tag{2.14}$$

5. Inside $\Omega_I$, the first and the third terms cancel formally when a complete basis is used. In practice, this does not happen because it depends on the quality of the expansion of $|\tilde{\psi}_i\rangle$ in $|\tilde{\phi}_k\rangle$. However, the difference is usually very small [26].

$$\sum_k |\tilde{\phi}_k\rangle\langle\tilde{p}_k|\tilde{\psi}_i\rangle = |\tilde{\psi}_i\rangle \qquad \text{inside } \Omega_I. \tag{2.15}$$

[6] $|\tilde{\psi}_i\rangle$ can be identified with the envelope function of the linear methods [24] or with the pseudo wave function of the pseudopotential methods [25].

6. In this way, the third term will provide the necessary *correction* to the first two terms, eliminating the smooth part of $|\tilde{\psi}_i\rangle$ inside $\Omega_I$ (first term), and the poor description of $|\psi_i\rangle$ in $|\phi_k\rangle$ outside $\Omega_I$ (second term).

7. Thus, there will be a cancellation of terms inside and outside $\Omega_I$ that will allow $|\psi_i\rangle$ to be described in AE partial waves $|\phi_k\rangle$ inside $\Omega_I$ and in plane waves outside $\Omega_I$:

$$|\psi_i\rangle = |\tilde{\psi}_i\rangle \qquad \text{outside } \Omega_I \tag{2.16}$$

and

$$|\psi_i\rangle = \sum_k |\phi_k\rangle\langle\tilde{p}_k|\tilde{\psi}_i\rangle \qquad \text{inside } \Omega_I. \tag{2.17}$$

8. Finally, note that if a *complete* basis of partial waves, and a *complete* basis of plane waves are used to calculate and transform $|\tilde{\psi}_i\rangle$, then the first and the third term in Eq. (2.13) are the same and they are cancelled.

In practice, only the (valence) $|\tilde{\psi}_i\rangle$, smooth functions in the whole space (or, equivalently, within the unit cell) are calculated selfconsistently using a finite basis of plane waves[7].

$$\langle r|\tilde{\psi}_i\rangle = \tilde{\psi}_i(\vec{r}) = \sum_{\vec{G}} \tilde{\psi}_i(\vec{G}) e^{i(\vec{k}+\vec{G})\cdot\vec{r}}. \tag{2.18}$$

For crystalline systems, the index $i \equiv \vec{k}n$, where $n$ is the band index and $\vec{k}$ is the Bloch wave vector that belongs to the first Brillouin zone. Thus, the selfconsistent solution of the KS equations determines the $\tilde{\psi}_i(\vec{G})$, which are the coefficients of the expansion in plane waves.

Subsequently the $|\tilde{\psi}_i\rangle$ are *transformed* into $|\psi_i\rangle$ through the transformation operator $\mathcal{T}$, defined in Eq. (2.13):

$$|\psi_i\rangle = \mathcal{T}|\tilde{\psi}_i\rangle = \left[1 + \sum_k |\phi_k\rangle\langle\tilde{p}_k| - \sum_k |\tilde{\phi}_k\rangle\langle\tilde{p}_k|\right]|\tilde{\psi}_i\rangle. \tag{2.19}$$

[7]The plane waves are included up to a *cut-off* energy that corresponds to the maximum kinetic energy of a plane wave, $E_{pw}^{cut} = \frac{1}{2}G_{max}^2$, where $G$ is the module of the wave vector of the plane wave. In crystalline systems, $E_{pw}^{cut} = \frac{1}{2}|\vec{k}+\vec{G}|_{max}^2$, where $\vec{k}$ is the Bloch wave vector and belongs to the first Brillouin zone. Thus, the size of the plane wave basis is controlled by the only parameter $E_{pw}^{cut}$.

$|\phi_k\rangle$, $|\tilde{\phi}_k\rangle$ and $\langle\tilde{p}_k|$ are calculated only once and remain fixed during the calculation. They also define the transformation $\mathcal{T}$. On the other hand, the coefficients $c_k = \langle\tilde{p}_k|\tilde{\psi}_i\rangle$ in Eq. (2.13) change during the calculation due to the selfconsistency process of the $|\tilde{\psi}_i\rangle$.

A complete (infinite) basis of partial waves is impossible to use. The number $n$ of valence AE partial waves $|\phi_k\rangle$, *pseudo* partial waves $|\tilde{\phi}_k\rangle$ and *projectors* $|\tilde{p}_k\rangle$ per angular momentum $(l, m)$ per site $I$ ($k \equiv I, l, m, n$) is chosen so as to describe satisfactorily the scattering properties of the valence band region for the isolated atom. This number is controlled in the same way for all-three functions, due to the one-one relationship among them (Section 2.4.5).

Usually, a good convergence is obtained using a cut-off energy for the plane waves of 30 Ry, and two partial waves per angular momentum $(l, m)$ and site $I$. Nevertheless, these values depend strongly on the materials system and on the studied properties.

### 2.4.3 The Core Electrons

The core electrons belong to the innermost regions of the atom and they are much less disturbed by the external environment than the valence electrons. For this reason, the core electrons will be treated within the "frozen core" approximation. In this approximation, the density of the core electrons is maintained constant with respect to the corresponding isolated atom.

In the PAW method the core states are imported from the isolated atom. The AE core wave functions $|\psi_i^c\rangle$ can be expressed in a similar way to the valence wave functions, that is, divided in three contributions:

$$|\psi_i^c\rangle = |\tilde{\psi}_i^c\rangle + |\phi_i^c\rangle - |\tilde{\phi}_i^c\rangle, \qquad i = 1, \ldots, N_c, \tag{2.20}$$

where $N_c$ is the number of core states. $|\tilde{\psi}_i^c\rangle$ is the core *pseudo* wave function, that is identical to $|\psi_i^c\rangle$ outside $\Omega_I$ and smooth inside. In general, the *augmentation* region is defined so that $|\psi_i^c\rangle$ are contained inside $\Omega_I$, however, a small part can be, eventually, outside $\Omega_I$. $|\phi_i^c\rangle$ is a (unique) AE core partial wave, that is identical to $|\psi_i^c\rangle$ and it is expressed as a radial function times spherical harmonics. $|\tilde{\phi}_i^c\rangle$ is a (unique) core *pseudo* partial wave, that is identical to $|\tilde{\psi}_i^c\rangle$ and it is also expressed as a radial function times spherical harmonics. Note that, unlike the valence states, it is not necessary to define *projectors* for the core states because the coefficients of the partial waves are always equal to the unit.

### 2.4.4 Transformation Operator

In this section I will describe the way the transformation operator $\mathcal{T}$, Eq. (2.19), is constructed and some important consequences for the implementation of the method coming from this construction. In the following, it will be necessary to consider complete bases of partial waves and plane waves.

Consider the Hilbert space of all the AE valence wave functions of the system, $|\psi_i\rangle$ (orthogonal to the core wave functions), and the *pseudo* Hilbert space of all the corresponding *pseudo* wave functions, $|\tilde{\psi}_i\rangle$. The transformation operator $\mathcal{T}$ allows to relate the elements of those two Hilbert spaces. For the isolated atom, the AE valence wave functions are the AE partial waves, $|\phi_k\rangle$, and the corresponding *pseudo* wave functions are the *pseudo* partial waves, $|\tilde{\phi}_k\rangle$. In the following, all of the quantities related with the *pseudo* representation of the wave functions will be indicated by a tilde.

If $\mathcal{T}$ should modify $|\tilde{\psi}_i\rangle$ only inside $\Omega_I$ (in each site $I$ of the system), so that the resultant $|\psi_i\rangle$ has the correct nodal structure, then $\mathcal{T}$ can be expressed as the identity operator plus a sum of localized operators $\mathcal{S}_I$; the $\mathcal{S}_I$ operators are only defined inside $\Omega_I$ for each site $I$ and in an independent way:

$$\mathcal{T} = 1 + \sum_I \mathcal{S}_I. \tag{2.21}$$

Note that, in general, the $\mathcal{S}_I$ are different for each site $I$. Consider now the action of $\mathcal{T}$ on the solutions $|\phi_k\rangle$ for the isolated atom. In the isolated atom, $\mathcal{T}$ will only have a unique local contribution $\mathcal{S}_I$ due to the only atom of the system $I$, then:

$$|\phi_k\rangle = \mathcal{T}|\tilde{\phi}_k\rangle = (1 + \mathcal{S}_I)|\tilde{\phi}_k\rangle, \tag{2.22}$$

where $k \equiv I, l, m, n$ and $I$ is fixed. Eq. (2.22) defines the *transformation* of (all) the elements of the *pseudo* Hilbert space into the elements of the Hilbert space (not only the isolated atom). Thus, from this equation it is possible to define $\mathcal{S}_I$ for the site $I$:

$$\mathcal{S}_I|\tilde{\phi}_k\rangle = |\phi_k\rangle - |\tilde{\phi}_k\rangle \qquad \text{inside } \Omega_I. \tag{2.23}$$

Since $\mathcal{S}_I$ is defined only inside $\Omega_I$ then $|\phi_k\rangle$ and $|\tilde{\phi}_k\rangle$ can also be defined only inside $\Omega_I$.

Consider now a more general system, with arbitrary number of atoms. Inside each $\Omega_I$ of the system, Eq. (2.22) is valid. If $|\tilde{\psi}_i\rangle$ is expanded in a complete basis of $|\tilde{\phi}_k\rangle$ inside each $\Omega_I$ (with fixed $I$):

$$|\tilde{\psi}_i\rangle = \sum_{(I),l,m,n} |\tilde{\phi}_k\rangle c_k \qquad \text{inside } \Omega_I, \tag{2.24}$$

then operating on $|\tilde{\phi}_k\rangle$, using Eq. (2.22):

$$|\psi_i\rangle = (1+\mathcal{S}_I)|\tilde{\psi}_i\rangle = \sum_{(I),l,m,n} (1+\mathcal{S}_I)|\tilde{\phi}_k\rangle c_k = \sum_{(I),l,m,n} |\phi_k\rangle c_k \quad \text{inside } \Omega_I, \tag{2.25}$$

and Eq. (2.23):

$$\mathcal{S}_I|\tilde{\psi}_i\rangle = \sum_{(I),l,m,n} \mathcal{S}_I|\tilde{\phi}_k\rangle c_k = \sum_{(I),l,m,n} \Big(|\phi_k\rangle - |\tilde{\phi}_k\rangle\Big) c_k \qquad \text{inside } \Omega_I. \tag{2.26}$$

and the scalar coefficients $c_k$ are the *same* because they are not transformed. The description of $|\psi_i\rangle$ is exact because a complete basis of $|\tilde{\phi}_k\rangle$ (inside $\Omega_I$ and for any fixed $I$) was used to describe $|\tilde{\psi}_i\rangle$. It is simple to generalize Eqs. (2.24) and (2.25) to *all* the sites $I$ of the system because, in principle, each site is independent. In this way, it is possible to obtain or *recover* the correct nodal structure of $|\psi_i\rangle$ on each site $I$ (inside $\Omega_I$) starting from the calculation of $|\tilde{\psi}_i\rangle$ which is a smooth function[8].

The form of the scalar coefficients $c_k$ need to be defined. $\mathcal{T}$ should be a *linear transformation*, therefore, the coefficients $c_k$ should be linear functionals of $|\tilde{\psi}_i\rangle$. The simplest choice for the linear functional is the scalar product of $|\tilde{\psi}_i\rangle$ with some fixed function [22]:

$$c_k = \langle \tilde{p}_k|\tilde{\psi}_i\rangle. \tag{2.27}$$

The fixed functions $\langle \tilde{p}_k|$ are called *projectors* and for each $|\tilde{\phi}_k\rangle$ there is a corresponding *projector* $|\tilde{p}_k\rangle$ (Section 2.4.5). Consequently, the $\langle \tilde{p}_k|$ are also defined only inside $\Omega_I$ and are fixed. From Eqs. (2.24) and (2.27) the following condition is obtained for the *projectors*:

$$\sum_{(I),l,m,n} |\tilde{\phi}_k\rangle\langle \tilde{p}_k| = 1 \qquad \text{inside } \Omega_I, \tag{2.28}$$

where a complete basis of $|\tilde{\phi}_k\rangle$ has been considered. From this equation, it is possible to obtain the **orthonormality relationships**:

[8]Since the *transformation* $|\psi_i\rangle = \mathcal{T}|\tilde{\psi}_i\rangle$ is also used for the partial waves $|\phi_k\rangle = \mathcal{T}|\tilde{\phi}_k\rangle$, Eq. (2.22). Then, inside $\Omega_I$, the quality of the description of $|\tilde{\psi}_i\rangle$ by $|\tilde{\phi}_k\rangle$ will be the same as $|\psi_i\rangle$ by $|\phi_k\rangle$.

$$\langle \tilde{p}_i | \tilde{\phi}_j \rangle = \delta_{ij}. \tag{2.29}$$

Note that the $\langle \tilde{p}_k|$ (and $|\tilde{\phi}_k\rangle$) not need to be orthogonal among themselves.

Finally, $\mathcal{T}$ will be obtained starting from the isolated atom. Consider the action of $\mathcal{S}_I$ on $|\tilde{\psi}_i\rangle$ on a single atomic site (fixed $I$), and through Eqs. (2.26) and (2.27):

$$\mathcal{S}_I|\tilde{\psi}_i\rangle = \sum_{(I),l,m,n} \mathcal{S}_I|\tilde{\phi}_k\rangle\langle\tilde{p}_k|\tilde{\psi}_i\rangle = \sum_{(I),l,m,n} \Big(|\phi_k\rangle - |\tilde{\phi}_k\rangle\Big)\langle\tilde{p}_k|\tilde{\psi}_i\rangle \qquad \text{inside } \Omega_I. \tag{2.30}$$

Since $\mathcal{T}$ is an operator defined in the whole space (in all sites $I$ of the system), then $I$ is no longer fixed. Therefore, the action of $\mathcal{T}$ on $|\tilde{\psi}_i\rangle$, according to Eqs. (2.21) and (2.30), results in:

$$\mathcal{T}|\tilde{\psi}_i\rangle = \Big[1 + \sum_I \mathcal{S}_I\Big]|\tilde{\psi}_i\rangle = \Big[1 + \sum_k \Big(|\phi_k\rangle - |\tilde{\phi}_k\rangle\Big)\langle\tilde{p}_k|\Big]|\tilde{\psi}_i\rangle \tag{2.31}$$

with $k \equiv I, l, m, n$. And this result is identical to Eq. (2.19).

### 2.4.5 Partial Waves and *Projectors*

In this section I will briefly describe the way the AE valence partial waves $|\phi_k\rangle$, the *pseudo* partial waves $|\tilde{\phi}_k\rangle$ and the *projectors* $|\tilde{p}_k\rangle$ are obtained, subject to the **orthonormality relationship**, Eq. (2.29). To obtain $|\phi_k\rangle$, $|\tilde{\phi}_k\rangle$ and $|\tilde{p}_k\rangle$ the PAW method is not used, but note again that, according to Eq. (2.22), the particular construction of the $|\tilde{\phi}_k\rangle$ determines the PAW *transformation* $\mathcal{T}$ between the elements of the *pseudo* Hilbert space and the Hilbert space.

#### AE Partial Waves

The AE valence partial waves $|\phi_k\rangle$ are expressed as a radial function $|\chi_k\rangle$ times spherical harmonics $Y_{l,m}(\hat{r})$:

$$\langle r|\phi_k\rangle = \phi_k(\vec{r}) = \chi_k(r)Y_{l,m}(\hat{r}). \tag{2.32}$$

The radial functions $|\chi_k\rangle$ are solutions to the radial Schrödinger equation for the isolated atom:

$$\Big(-\frac{1}{2}\nabla_r^2 + v_I^{at}\Big)|\chi_k\rangle = \epsilon_k|\chi_k\rangle, \tag{2.33}$$

where $v_I^{at}(r)$ is the AE selfconsistent atomic potential[9].

To determine the (finite) basis of $|\phi_k\rangle$ a group is sought that describes satisfactorily the scattering properties of the valence band region for the isolated atom. In order to describe states that are much higher in energy than the valence band region, the number of AE partial waves can be increased to obtain the desired precision.

### *Pseudo* Partial Waves

The *pseudo* partial waves $|\tilde{\phi}_k\rangle$ are smooth functions (in the whole space), constructed independently for the corresponding AE partial waves $|\phi_k\rangle$ (solutions for the isolated atom). The pseudopotential approach is normally used to construct the $|\tilde{\phi}_k\rangle$[10]. Note, however, that this construction is not unique and other methods can be used.

In a similar way to the construction of the AE partial waves, the $|\tilde{\phi}_k\rangle$ are expressed as a radial function $|\tilde{\chi}_k\rangle$ times spherical harmonics $Y_{l,m}(\hat{r})$:

$$\langle r|\tilde{\phi}_k\rangle = \tilde{\phi}_k(\vec{r}) = \tilde{\chi}_k(r)Y_{l,m}(\hat{r}), \tag{2.34}$$

where the radial functions $|\tilde{\chi}_k\rangle$ are solutions to the modified and non-relativistic radial Schrödinger equation for the isolated atom:

$$\Big(-\frac{1}{2}\nabla_r^2 + \tilde{w}_k\Big)|\tilde{\chi}_k\rangle = \epsilon_k|\tilde{\chi}_k\rangle. \tag{2.35}$$

$\tilde{w}_k(r)$ is the smooth atomic pseudopotential, identical to the AE atomic potential $v_I^{at}(r)$ outside $\Omega_I$, and $\epsilon_k$ is the energy of the corresponding AE partial wave $|\phi_k\rangle$.

### *Projectors*

The *projectors* $|\tilde{p}_k\rangle$ are built from the *pseudo* partial waves $|\tilde{\phi}_k\rangle$ and subsequently they are subject to the **orthonormality relationship**, Eq. (2.29). $|\tilde{p}_k\rangle$ are also expressed as a radial function $|\tilde{q}_k\rangle$ times spherical harmonics $Y_{l,m}(\hat{r})$:

$$\langle r|\tilde{p}_k\rangle = \tilde{p}_k(\vec{r}) = \tilde{q}_k(r)Y_{l,m}(\hat{r}), \tag{2.36}$$

and the $|\tilde{q}_k\rangle$ are obtained directly from $|\tilde{\chi}_k\rangle$, according to:

[9] In the CP-PAW implementation used in the present work, $v_I^{at}(r)$ incorporates scalar-relativistic effects according to the version of Koelling and Harmon [27].

[10] In the CP-PAW implementation used in this work, $|\tilde{\phi}_k\rangle$ are built using the norm-conserving pseudopotential approach [25].

$$|\tilde{q}_k\rangle = \Big( -\frac{1}{2}\nabla^2 + \tilde{v}_k^{at} - \epsilon_k \Big)|\tilde{\chi}_k\rangle, \tag{2.37}$$

where $\tilde{v}_k^{at}(r)$ is a smooth atomic pseudopotential related to $\tilde{w}_k(r)$ (Ref. [22]) and $|\tilde{\chi}_k\rangle$ is the radial part of the *pseudo* partial wave with energy $\epsilon_k$, Eq. (2.35).

The **orthonormality relationship**, Eq. (2.29), is then imposed, where $|\phi_k\rangle$, $|\tilde{\phi}_k\rangle$ and $|\tilde{p}_k\rangle$ are modified in a recursive process of the Gram-Schmidt type (for details see Ref. [22]).

For the calculation of the coefficients of the expansions in partial waves, $\langle\tilde{p}_k|\tilde{\psi}_i\rangle$, of Eq. (2.13), the $|\tilde{p}_k\rangle$ are expanded in the same basis of plane waves used to expand $|\tilde{\psi}_i\rangle$.

### 2.4.6 Expectation Values, Total Energy

Analogously to the $|\psi_i\rangle$, Eq. (2.13), the operators and the expectation values can be divided into three contributions. A brief description of the way the expectation values are obtained, and explicit expressions for the calculation of the density and the total energy will be given. The complete formalism can be found in Ref. [22].

#### Expectation Values

The expectation values can be obtained using either the AE wave functions $|\psi_i\rangle$ or the *pseudo* wave functions $|\tilde{\psi}_i\rangle$, related by $|\psi_i\rangle = \mathcal{T}|\tilde{\psi}_i\rangle$, according to:

$$\langle\mathcal{A}\rangle = \sum_i f_i \langle\psi_i|\mathcal{A}|\psi_i\rangle + \sum_{i=1}^{N_c}\langle\psi_i^c|\mathcal{A}|\psi_i^c\rangle \tag{2.38}$$

$$\langle\mathcal{A}\rangle = \sum_i f_i \langle\tilde{\psi}_i|\mathcal{T}^\dagger\mathcal{A}\mathcal{T}|\tilde{\psi}_i\rangle + \sum_{i=1}^{N_c}\langle\psi_i^c|\mathcal{A}|\psi_i^c\rangle. \tag{2.39}$$

Here $f_i$ are the occupation numbers of the valence states, $N_c$ is the number of core states, $|\psi_i^c\rangle$ are the core states defined according to Eq. (2.20). The first sum is over the valence states and the second, the core states.

The *pseudo* operator $\tilde{\mathcal{A}} = \mathcal{T}^\dagger\mathcal{A}\mathcal{T}$ can be divided into three contributions (similar to $|\psi_i\rangle$), using Eq. (2.13) or (2.19):

$$\begin{aligned}\tilde{\mathcal{A}} &= \mathcal{T}^\dagger\mathcal{A}\mathcal{T} \\ &= \Big[1 + \sum_k |\tilde{p}_k\rangle\Big(\langle\phi_k| - \langle\tilde{\phi}_k|\Big)\Big]\mathcal{A}\Big[1 + \sum_l \Big(|\phi_l\rangle - |\tilde{\phi}_l\rangle\Big)\langle\tilde{p}_l|\Big]\end{aligned}$$

$$= \mathcal{A} + \sum_{k,l} |\tilde{p}_k\rangle \Big[ \langle \phi_k | \mathcal{A} | \phi_l \rangle - \langle \tilde{\phi}_k | \mathcal{A} | \tilde{\phi}_l \rangle \Big] \langle \tilde{p}_l |$$
$$= \mathcal{A} + \mathcal{A}^1 - \tilde{\mathcal{A}}^1, \tag{2.40}$$

where the one-center terms $\mathcal{A}^1$ and $\tilde{\mathcal{A}}^1$ are defined only inside $\Omega_I$ (for each $I$). However, Eq. (2.40) is valid only for local operators, such as the real space projection operator, $|r\rangle\langle r|$, the *overlap* operator, $\tilde{\mathcal{O}}$, or the kinetic energy operator, $-\nabla^2/2$. For non-local operators, corrections have to be included (see Ref. [22]).

Therefore, substituting (2.39) in (2.40), the expression for the expectation value of an operator $\mathcal{A}$ can be written as:

$$\langle \mathcal{A} \rangle = \sum_i f_i \Big( \langle \tilde{\psi}_i | \mathcal{A} | \tilde{\psi}_i \rangle + \sum_{k,l} \langle \tilde{\psi}_i | \tilde{p}_k \rangle \Big[ \langle \phi_k | \mathcal{A} | \phi_l \rangle - \langle \tilde{\phi}_k | \mathcal{A} | \tilde{\phi}_l \rangle \Big] \langle \tilde{p}_l | \tilde{\psi}_i \rangle \Big)$$
$$+ \sum_{i=1}^{N_c} \langle \psi_i^c | \mathcal{A} | \psi_i^c \rangle. \tag{2.41}$$

### Density

The charge density (electronic density) $\rho(\vec{r})$ is the expectation value of the projection operator in real space, $|r\rangle\langle r|$:

$$\rho(\vec{r}) = \sum_i f_i |\psi_i(\vec{r})|^2 + \sum_{i=1}^{N_c} |\psi_i^c(\vec{r})|^2 = \sum_i f_i \langle \psi_i | r \rangle \langle r | \psi_i \rangle + \sum_{i=1}^{N_c} \langle \psi_i^c | r \rangle \langle r | \psi_i^c \rangle. \tag{2.42}$$

Applying Eq. (2.41):

$$\rho(\vec{r}) = \tilde{\rho}(\vec{r}) + \rho^1(\vec{r}) - \tilde{\rho}^1(\vec{r}) + \rho^c(\vec{r}) \tag{2.43}$$

$$\rho(\vec{r}) = \sum_i f_i \langle \tilde{\psi}_i | r \rangle \langle r | \tilde{\psi}_i \rangle$$
$$+ \sum_{i,k,l} f_i \langle \tilde{\psi}_i | \tilde{p}_k \rangle \langle \phi_k | r \rangle \langle r | \phi_l \rangle \langle \tilde{p}_l | \tilde{\psi}_i \rangle$$
$$- \sum_{i,k,l} f_i \langle \tilde{\psi}_i | \tilde{p}_k \rangle \langle \tilde{\phi}_k | r \rangle \langle r | \tilde{\phi}_l \rangle \langle \tilde{p}_l | \tilde{\psi}_i \rangle$$
$$+ \sum_{i=1}^{N_c} \langle \psi_i^c | r \rangle \langle r | \psi_i^c \rangle. \tag{2.44}$$

$\tilde{\rho}(\vec{r})$ is the *pseudo* density, a smooth function expanded in plane waves. $\rho^1(\vec{r})$ and $\tilde{\rho}^1(\vec{r})$ are the local density and local *pseudo* density, respectively (defined inside $\Omega_I$, for each $I$), and they depend on $|\tilde{\psi}_i\rangle$ through the coefficients $\langle\tilde{\psi}_i|\tilde{p}_k\rangle$ and $\langle\tilde{p}_l|\tilde{\psi}_i\rangle$. In order to obtain $\rho(\vec{r}) = \rho^1(\vec{r}) + \rho^c(\vec{r})$ inside $\Omega_I$, it is necessary that $\tilde{\rho}^1(\vec{r})$ cancels $\tilde{\rho}(\vec{r})$ within this region.

### Total Energy

The Kohn-Sham total energy functional $E = E^{KS} + E_{n-n}$, where $E^{KS}$ is the KS electronic total energy, Eq. (2.6), and $E_{n-n}$ is the nucleus-nucleus repulsion energy, can be re-written in a form where all the coulomb interactions (electron-electron, electron-nucleus and nucleus-nucleus) are collected in a single term:

$$\begin{aligned} E[\{\tilde{\psi}_i\},\{\vec{R}_I\}] = \sum_i f_i\langle\psi_i| - \frac{1}{2}\nabla^2|\psi_i\rangle \\ + \frac{1}{2}\int d\vec{r}\int d\vec{r'}\frac{\Big(\rho(\vec{r}) + \rho^Z(\vec{r})\Big)\Big(\rho(\vec{r'}) + \rho^Z(\vec{r'})\Big)}{|\vec{r} - \vec{r'}|} \\ + \int d\vec{r}\rho(\vec{r})\varepsilon_{xc}[\rho(\vec{r})]. \end{aligned} \tag{2.45}$$

Here the nuclear charges are expressed as $\rho^Z(\vec{r}) = -\sum_I Z_I\delta(\vec{r} - \vec{R}_I)$, where $Z_I$ is the atomic number of the atom at the $I$ site. $E$ is a functional of $\rho$, obtained from Eq. (2.44), and similar to $|\psi_i\rangle$, $E$ can also be divided into three parts:

$$E = \tilde{E} + E^1 - \tilde{E}^1, \tag{2.46}$$

where

$$\begin{aligned} \tilde{E} = \sum_i f_i\langle\tilde{\psi}_i| - \frac{1}{2}\nabla^2|\tilde{\psi}_i\rangle \\ + \frac{1}{2}\int d\vec{r}\int d\vec{r'}\frac{\Big(\tilde{\rho}(\vec{r}) + \hat{\rho}(\vec{r})\Big)\Big(\tilde{\rho}(\vec{r'}) + \hat{\rho}(\vec{r'})\Big)}{|\vec{r} - \vec{r'}|} \\ + \int d\vec{r}\tilde{\rho}(\vec{r})\bar{v}(\vec{r}) + \int d\vec{r}\tilde{\rho}(\vec{r})\varepsilon_{xc}[\tilde{\rho}(\vec{r})], \end{aligned} \tag{2.47}$$

$$E^1 = \sum_{i,k,l} f_i \langle \tilde{\psi}_i | \tilde{p}_k \rangle \langle \phi_k | - \frac{1}{2}\nabla^2 | \phi_l \rangle \langle \tilde{p}_l | \tilde{\psi}_i \rangle + \sum_{i=1}^{N_c} \langle \psi_i^c | - \frac{1}{2}\nabla^2 | \psi_i^c \rangle$$
$$+ \frac{1}{2} \int d\vec{r} \int d\vec{r'} \frac{\Big(\rho^1(\vec{r}) + \rho^Z(\vec{r})\Big)\Big(\rho^1(\vec{r'}) + \rho^Z(\vec{r'})\Big)}{|\vec{r} - \vec{r'}|}$$
$$+ \int d\vec{r} \rho^1(\vec{r}) \varepsilon_{xc}[\rho^1(\vec{r})], \tag{2.48}$$

$$\tilde{E}^1 = \sum_{i,k,l} f_i \langle \tilde{\psi}_i | \tilde{p}_k \rangle \langle \tilde{\phi}_k | - \frac{1}{2}\nabla^2 | \tilde{\phi}_l \rangle \langle \tilde{p}_l | \tilde{\psi}_i \rangle$$
$$+ \frac{1}{2} \int d\vec{r} \int d\vec{r'} \frac{\Big(\tilde{\rho}^1(\vec{r}) + \hat{\rho}(\vec{r})\Big)\Big(\tilde{\rho}^1(\vec{r'}) + \hat{\rho}(\vec{r'})\Big)}{|\vec{r} - \vec{r'}|}$$
$$+ \int d\vec{r} \tilde{\rho}^1(\vec{r}) \bar{v}(\vec{r}) + \int d\vec{r} \tilde{\rho}^1(\vec{r}) \varepsilon_{xc}[\tilde{\rho}^1(\vec{r})]. \tag{2.49}$$

$\tilde{\rho}(\vec{r})$, $\rho^1(\vec{r})$ and $\tilde{\rho}^1(\vec{r})$ have been defined previously, Eqs. (2.43) and (2.44). The charge density $\hat{\rho}(\vec{r})$ and the potential $\bar{v}(\vec{r})$ have been introduced in this equation (a detailed description of this terms can be found in Ref. [22]).

### 2.4.7 Dynamics of the Nuclei and the Wave Functions

In the original work of Blöchl [22], the PAW method was implemented in the *ab initio* molecular dynamics of Car and Parrinello [15] (Section 2.3), making it possible to to calculate equilibrium geometries and perform *ab initio* molecular dynamics simulations on the PES. In AIMD, the electronic and nuclear variables evolve *classically* and *simultaneously* through forces obtained at each time step from the instantaneous electronic structure.

The electronic variables in the PAW method are the valence *pseudo* wave functions $\{\tilde{\psi}_i\}$, expanded in a basis of plane waves, Eq. (2.18), where the only electronic degrees of freedom are the coefficients of the expansion in plane waves $\tilde{\psi}_i(\vec{G})$. The nuclear variables are the positions of the nuclei (atoms) $\{\vec{R}_I\}$. For the calculation of the forces it is necessary to obtain expressions for the overlap and Hamiltonian operators, which will be described below (for complete details see Ref. [22]).

### Overlap Operator

The overlap operator in the AE representation is the identity operator $\hat{1}$. The *pseudo* overlap operator $\tilde{\mathcal{O}}$ can be obtained using Eq. (2.40):

$$\tilde{\mathcal{O}} = 1 + \sum_{k,l} |\tilde{p}_k\rangle \Big[ \langle \phi_k | \phi_l \rangle - \langle \tilde{\phi}_k | \tilde{\phi}_l \rangle \Big] \langle \tilde{p}_l |. \tag{2.50}$$

An important consequence is that $\tilde{\mathcal{O}}$ is no longer independent of the nuclear coordinates $\{\vec{R}_I\}$, which originates additional forces acting on the nuclei (see below).

### Hamiltonian Operator

Consistent with the use of $|\tilde{\psi}_i\rangle$ as variational parameters, the *pseudo* Hamiltonian operator $\tilde{\mathcal{H}}^{KS}$ will be used to obtain the forces acting on $|\tilde{\psi}_i\rangle$, according to the equation of motion Eq. (2.9). The expression for $\tilde{\mathcal{H}}^{KS}$ is [22]:

$$\tilde{\mathcal{H}}^{KS} = -\frac{1}{2}\nabla^2 + \tilde{v}_{ef} + \sum_{k,l} |\tilde{p}_k\rangle \Big[ \langle \phi_k | -\frac{1}{2}\nabla^2 + v^1_{ef} | \phi_l \rangle - \langle \tilde{\phi}_k | -\frac{1}{2}\nabla^2 + \tilde{v}^1_{ef} | \tilde{\phi}_l \rangle \Big] \langle \tilde{p}_l |. \tag{2.51}$$

where the AE Kohn-Sham potential $v_{ef}$ is separated into three contributions:

$$v_{ef} = \tilde{v}_{ef} + v^1_{ef} - \tilde{v}^1_{ef}. \tag{2.52}$$

### The Verlet Algorithm

The Verlet algorithm [28] is used to integrate the AIMD equations of motion for the nuclear $\{\vec{R}_I\}$, Eq. (2.8), and electronic $\{\tilde{\psi}_i\}$, Eq. (2.9) variables. The algorithm is:

$$x_i(+) = 2x_i(0) - x_i(-) + F_i(0)\frac{\Delta^2}{m_i}, \tag{2.53}$$

where $x_i(t)$ is a time-dependent coordinate (variable), $\Delta$ is the time step, $x_i(0)$ is the current position, $x_i(-)$ is the previous position and $x_i(+)$, the subsequent position in time. $F_i$ is the force acting on the coordinate $x_i$, and $m_i$ is a mass parameter. The coordinates $x_i$, obtained using the Verlet algorithm are exact up to order $(\Delta^3)$.

### Propagation of the Wave Functions

When the AIMD equations of motion for $|\tilde{\psi}_i\rangle$, Eq. (2.9), are integrated according to Eq. (2.53), using the *pseudo* operators $\tilde{\mathcal{H}}^{KS}$ and $\tilde{\mathcal{O}}$, it is obtained:

$$|\tilde{\psi}_i(+)\rangle = 2|\tilde{\psi}_i(0)\rangle - |\tilde{\psi}_i(-)\rangle - \tilde{\mathcal{H}}^{KS}|\tilde{\psi}_i(0)\rangle\frac{\Delta^2}{m_\psi} + \frac{\Delta^2}{m_\psi f_i}\sum_j \tilde{\mathcal{O}}(0)|\tilde{\psi}_j(0)\rangle\Lambda_{ji}. \tag{2.54}$$

The last term corresponds the forces originating from the orthonormality constraint for the $|\tilde{\psi}_i\rangle$. The Lagrange multipliers $\Lambda_{ji}$ are determined iteratively so that the constraints are satisfied for the subsequent time step (+) [22]:

$$\langle\tilde{\psi}_i(+)|\tilde{\mathcal{O}}(+)|\tilde{\psi}_j(+)\rangle = \delta_{ij}. \tag{2.55}$$

$\tilde{\mathcal{O}}$ depends on the position, Eq. (2.50) and, in general, $\tilde{\mathcal{O}}(+)$ differs from $\tilde{\mathcal{O}}(0)$ if the $\vec{R}_I$ are evolving. Thus, it is necessary to know the subsequent atomic configuration $\{\vec{R}_I(+)\}$.

### Propagation of the Nuclei

The AIMD equations of motion for the nuclei $\{\vec{R}_I\}$, Eq. (2.8), are also integrated using the Verlet algorithm, Eq. (2.53):

$$\vec{R}_I(+) = 2\vec{R}_I(0) - \vec{R}_I(-) + \vec{F}_I(0)\frac{\Delta^2}{M_I}. \tag{2.56}$$

Since the partial waves and *projectors* depend on the site $I$ (or the nuclear coordinates $\{\vec{R}_I\}$), according to Eq. (2.17), this dependence should result in a contribution (Pulay forces, Section 2.3.2) to the forces $\vec{F}_I$. The resulting force acting on the nuclei contains the dependence on the position of $\tilde{\mathcal{O}}$:

$$\vec{F}_I(0) = -\sum_i f_i\langle\tilde{\psi}_i|\nabla_I\tilde{\mathcal{H}}^{KS}|\tilde{\psi}_i\rangle + \sum_{i,j}\langle\tilde{\psi}_i|\nabla_I\tilde{\mathcal{O}}|\tilde{\psi}_j\rangle\Lambda_{ji}, \tag{2.57}$$

where the Lagrange multipliers $\Lambda_{ji}(0)$ are linearly extrapolated from the two previous time steps $(-)$ and $(-2)$.

## 2.5 The Supercell Approach

Historically, before its application on selfconsistent calculations of the electronic structure of surfaces, the *slabs* were used to study the vibrational properties of surfaces [29], e.g. surface vibrational modes of systems with 2D periodicity and one (semi-infinite surface) or two (thin film) surfaces. Inspired by the previous work with surface *slabs*, Cohen *et al.* [30] presented a method for the selfconsistent calculation of the atomic and electronic structure of localized configurations, such as, atoms, molecules, impurities, vacancies, unidimensional chains, two-dimensional layers, adsorbed substances, surfaces or interfaces between solids. In that work, the energy levels and the charge densities of the (isolated) $Si_2$ molecule were calculated using a periodically repeated unit cell and a basis of plane waves.

An isolated molecule is a non-periodic system, however, in this method an *artificial* or non-physical 3D periodic (crystalline) system is created composed of unit cells that contain the molecule and surrounding vacuum, large enough to isolate the molecule from the images in neighbouring cells. Consistent with the artificial 3D periodicity of the system, Cohen *et al.* [30] noted that in the calculation of the $Si_2$ molecule, the selfconsistent results depended little on the structure or symmetry of the unit cell, if the number of plane waves[11] (size of the basis) was sufficiently large. To decouple the charge density of the molecule, expanded in plane waves, from their periodic images, it is necessary to turn neglegible the interaction energy within those periodic images. This interaction can be divided into two contributions due to: The overlap of the wave functions and the electrostatic interaction. The overlap of the wave functions can be neglected if the images are separated a distance of around 7 Å [30]. Nevertheless, the separation of the images can not be used to solve the problem of the electrostatic interaction because the electrostatic potential is a long-distance interaction. To address this, a method to subtract the electrostatic interaction between the electronic densities of the periodic images of isolated molecules, expanded in plane waves, was developed by Blöchl [31].

For the calculation of surfaces, a *slab* (with two surfaces) is included within the unit cell. In the direction parallel to the surface, it has the 2D periodicity of the *real* surface and in the direction perpendicular to the surface, it has a vacuum region sufficiently large to minimize the *artificial* interaction between neighbouring *slabs*. A symmetric *slab* is one which has inversion or mirror symmetry in the direction perpendicular to the surface. This sym-

[11] A function constructed from plane waves (with wave vectors identical to the reciprocal lattice vectors) will be periodic in real space. Thus, the expansion of a function in a discreet group of plane waves generates a periodic system.

metry can be considered as a molecular point group symmetry, in the sense that it belongs to a 2D system which is not periodic in this direction. In this type of slab the innermost layers represent the bulk and they are frozen during the simulation, while all the other layers (and adsorbates) are free to relax. The unit cell, thus, should be tall, with the base defined by the 2D real lattice vectors (parallel to the surface) and enough height for the interaction between the two surfaces of the *slab*, through the *bulk* (thickness of the *slab*) and through the vacuum, to be neglegible. The thickness of a symmetrically terminated *slab* should be sufficient to conveniently simulate the bulk potential acting on the surface layers. And, depending on the studied properties, to: (i) effectively decouple the two surfaces of the *slab*, so that the degeneracy of the surface states from both surfaces can be controlled within a certain precision (the degeneracy occurs when the thickness of the *slab* is infinite); (ii) distinguish the surface states (particularly those whose wave functions decay slowly in the bulk) from the bulk states [32]. In addition, the size of the vacuum should be enough for the decay of the surface potential of the *slab* in the vacuum not to be perturbed by the neighbouring *slabs* [33]. In an unsymmetric *slab*,one of the surfaces is considered the bulk (usually called bottom layer) and it is kept frozen during the simulation, while the other layers are free to relax. In this type of *slab*, there is a long-range interaction between the two surfaces of the *slab*. To correct for this (small) spurious interaction, a method that uses a dipole layer in the vacuum was proposed by Neugebauer and Scheffler [34].

# Chapter 3

# Surfactant-mediated epitaxial growth of Ge on $SrHfO_3(001)$

## 3.1 Overview

Growth of GeOI substrates using high-k oxides such as strontium hafniate ($SrHfO_3$) are of great technological and scientific interest [35]. Direct heteroepitaxial growth of Ge on an oxide has been avoided due to the unfavorable growth mode, Volmer-Weber (3D-islands), that results in a Ge film with a large density of defects and rough morphology, unsuitable for transistor applications. In this work I will explore the possibility of using a third material, that could stabilize the epitaxial growth of Ge on the $SrHfO_3(001)$ surface and may even act as a so-called surfactant for layer-by-layer heteroepitaxial growth. The proposed material is strontium (Sr) and is in contrast with traditional surfactants used for Ge growth such as antimony (Sb) and arsenic (As).

In this chapter, I will study the Ge surface structures formed on the bare $SrHfO_3(001)$ substrate, in order to identify metastable epitaxial structures that could be stabilized by experimental conditions. The choice of a suitable surfactant that will stabilize the epitaxial Ge film will be discussed. Sr is then considered as an interesting candidate, and the formation of an ordered Sr 1ML film on the oxide surface, to be used as template for Ge layer-by-layer growth, will be studied. The changes in growth mode and growth kinetics when Ge is deposited on the Sr 1ML film, and the feasibility of forming a Ge epitaxial film will be investigated. Finally, adequate valence band offsets for transistor applications determined by the Sr interfaces will be discussed.

## 3.2 Computational details

The total energy calculations were performed with the Projector Augmented Wave (PAW) method [22] (Section 2.4) based on density-functional theory (DFT) [12] (Section 2.2). The exchange-correlation potential was treated with the generalized gradient approximation (GGA) as implemented by Perdew, Burke and Ernzerhof (PBE) [36]. The valence wave functions were expanded in plane waves outside the augmentation region and partial waves, inside. A plane wave *cut-off* of 30 Ry was used throughout to describe the plane wave part of the wave function. The following valence electrons were considered: $2s^2 2p^4$ for oxygen, $4s^2 4p^2$ for germanium (Ge), $4s^2 4p^6 5s^2$ for strontium (Sr), and $5s^2 5p^6 6s^2 5d^2$ for hafnium (Hf). And the following sets of *projector* functions per angular momentum $(s, p, d)$ were used: $(2, 2, 1)$ for oxygen, $(2, 2, 1)$ for Ge, $(3, 2, 2)$ for Sr, and $(2, 2, 2)$ for Hf. The semi-core states of Sr and Hf were treated as valence states. The frozen core approximation was used (Section 2.4.3).

A slab consisting of four layers was used to simulate the $SrHfO_3(001)$ surface (Section 2.5), and the back plane was kept frozen. The 2D-periodicity of the surface unit cell corresponds to (2x2)Ge(001). The experimental cubic lattice constant of $SrHfO_3$ was used (a=4.1131 Å, T=1403 K) [37]; the lattice mismatch with germanium is 2.8 % ($5.658/\sqrt{2} = 4.001$ Å [38]). A grid with 16 k-points per (1x1) surface unit cell, or equivalently four k-points per (2x2) surface unit cell, was used to sample the Brillouin zone. All structures were relaxed without symmetry constraints (except for time-inversion symmetry). The vacuum separating adjacent slab images in the direction perpendicular to the surface was never below 8 Å.

Convergence tests for bulk $SrHfO_3$ in the cubic structure, with a lattice constant of a=4.1131 Å (T=1403 K [37]), are presented in Figure 3.1. The converged plane wave kinetic energy *cut-off* is 40 Ry, with an accuracy of 26 meV (1.0 mH) relative to a 50 Ry *cut-off*. For this test, a total of eight k-points per cubic unit cell were used in all calculations. And for the Brillouin zone k-point sampling, the converged grid consisted of 64 k-points per cubic unit cell, with an accuracy of 0.9 meV (0.03 mH) relative to a grid corresponding to $10^3$ k-points per cubic unit cell. Therefore, a converged set for a $SrHfO_3$ slab with a (2x2) surface unit cell will consist of a 40 Ry plane wave *cut-off* and a grid with four k-points per (2x2) surface unit cell.

In this work, the description of the adsorption of Ge and Sr atoms on the $SrHfO_3(001)$ surface is the main concern. Thus, convergence tests have been performed for bulk Ge and bulk Sr, and they are presented in Figure 3.2. For bulk Ge in the *face centered cubic* (*fcc*) structure (a=5.658 Å [38]), the plane wave kinetic energy *cut-off* is converged at 25 Ry, the difference in

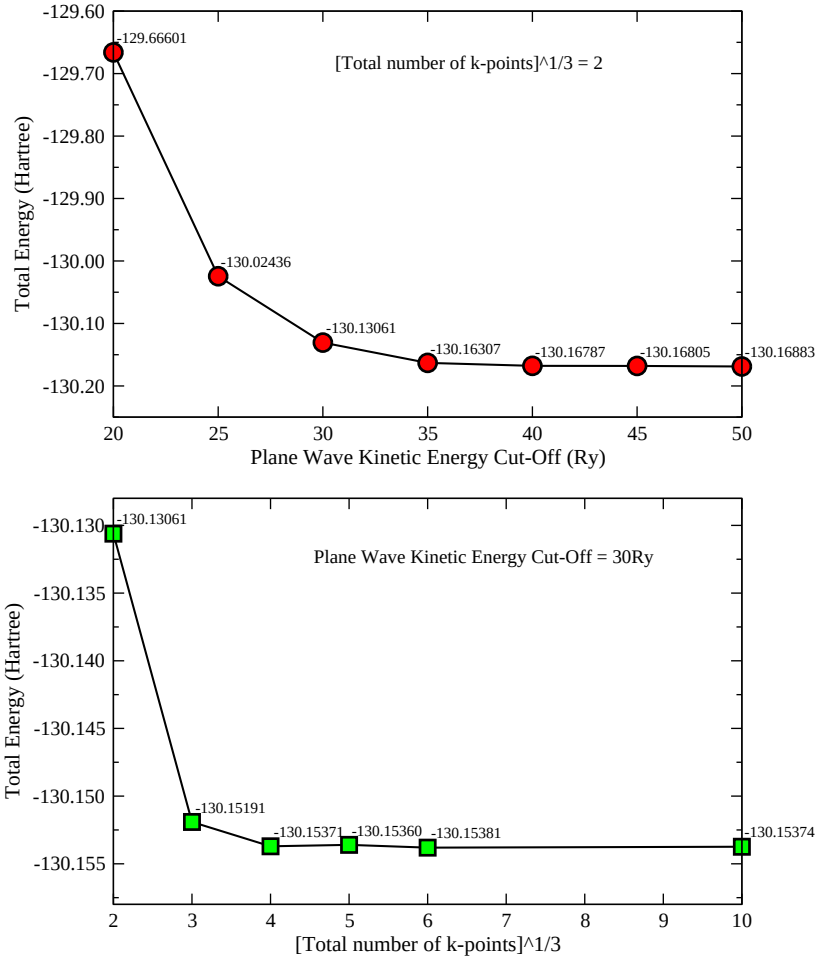


Figure 3.1: Convergence tests for bulk $SrHfO_3$ in the cubic structure (a=4.1131 Å, T=1403 K [37]). The total energy in Hartree units is plotted in the vertical axis. Top: Convergence test for the plane wave kinetic energy *cut-off*, with eight k-points per minimum cubic unit cell. Bottom: Convergence test for the Brillouin zone k-point sampling, the cubic root of the total number of k-points per cubic unit cell is plotted in the horizontal axis. A plane wave *cut-off* of 30 Ry was used for this convergence test.

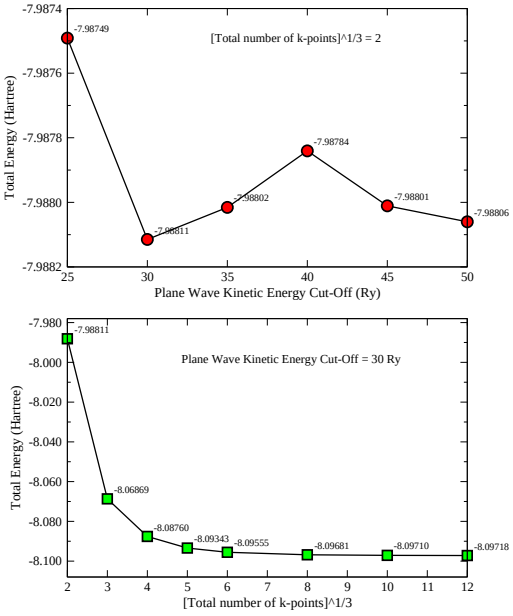


(a)

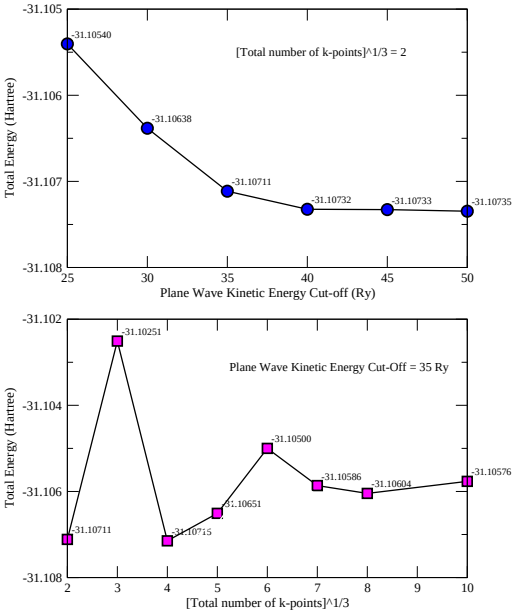


(b)

Figure 3.2: (a) Convergence tests for bulk Ge in the *fcc* structure (a=5.658 Å [38]). (b) Convergence tests for bulk Sr in the *fcc* structure (a=6.08 Å [10]). The notation is the same as in Figure 3.1.

total energy relative to a 50 Ry *cut-off* is 15 meV (0.6 mH). And a converged Brillouin zone sampling grid consists of $216 = 6^3$ k-points per *fcc* unit cell, the total energy difference relative to a grid consisting of $12^3$ k-points is 44 meV (1.6 mH). Therefore, a converged set for a (2x2)$Ge$(001) surface will consist of 25 Ry plane wave *cut-off*, and a grid with $2.7 \times 2.7$ k-points per (2x2) surface unit cell. As is common in density-functional calculations, the band gap is underestimated, and for bulk Ge no band gap is found. Convergence tests for bulk Sr, also in the *fcc* structure (6.08 Å [10]), determine that the plane wave kinetic energy *cut-off* is converged at 30 Ry, with 26 meV (1.0 mH) total energy difference relative to a 50 Ry *cut-off*. And the sampling grid is converged with $216 = 6^3$ k-points per *fcc* unit cell, the total energy difference relative to a grid with $10^3$ k-points is 21 meV (0.8 mH). Therefore, for a (2x2)$Sr$(001) surface, a converged set will consist of 30 Ry plane wave *cut-off*, and $2.7 \times 2.7$ k-points per (2x2) surface unit cell.

For all calculations presented in this chapter, a plane wave *cut-off* of 30 Ry and a grid with four k-points per (2x2) surface unit cell has been used. Thus, the plane wave *cut-off* is converged for the total energy of bulk Ge and bulk Sr, but not for bulk $SrHfO_3$. On the other hand, a grid with four k-points per (2x2) surface unit cell is converged for the total energy of bulk $SrHfO_3$, but not for bulk Ge and bulk Sr. In this work the main concern is the stability analysis (determination of total energy differences) of different Ge structures adsorbed on the surface. It is difficult to determine exactly the numerical errors in the calculations due to the use of these parameters. Nevertheless, the analysis of the calculated systems has been performed with a rather conservative criterium throughout this chapter. Whenever the difference in total energies is below 0.15 eV per atom, no conclusion regarding stability has been stated and the compared systems are regarded as almost degenerate. This criterium, however, does not affect the main conclusions of this chapter.

A convergence test for the thickness of the $SrHfO_3$(001) slab was performed considering the variation of the adsorption energy of an isolated Ge adatom. The adsorption energy was estimated according to Eq. (3.1) below. A plane wave *cut-off* of 30 Ry and a grid with four k-points per (2x2) surface unit cell was used in the test. The bottom layer is kept frozen in the bulk $SrHfO_3$ cubic structure, all other atomic coordinates are relaxed, and no symmetry constraints are applied. The results are shown in Figure 3.3. It was found that the difference in the adsorption energy of an isolated Ge adatom between a 4-layer and an 8-layer $SrHfO_3$(001) slab, with a (2x2) surface unit cell, is less than 0.10 eV.

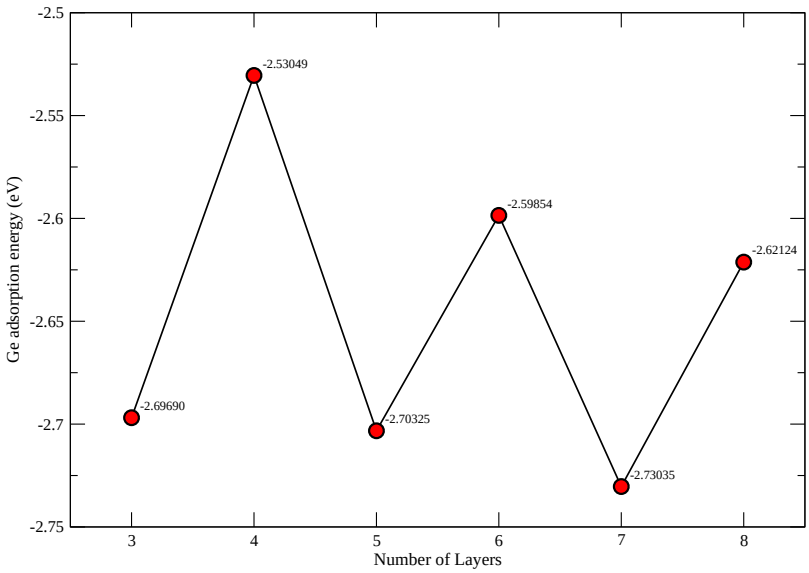


Figure 3.3: Convergence tests for the thickness of the $SrHfO_3(001)$ slab. The adsorption energy of an isolated Ge adatom on the $SrHfO_3(001)$ surface in eV is plotted against the number of layers in the slab (see text for details).

## 3.3 The perovskite crystal structure : Bulk $SrHfO_3$

The cubic perovskites have the chemical formula $ABO_3$. For II-IV perovskites (e.g. $SrHfO_3$), $A$ is a divalent cation and $B$ is a tetravalent transition metal, while for I-V perovskites (e.g. $KNbO_3$) they are mono- and pentavalent, respectively. $SrTiO_3$ is a standard model for oxides with a perovskite structure and has been widely studied. On the other hand, only a few studies exist on the properties of $SrHfO_3$ [37, 39]. Regarding the structural properties, it has been found that from 300 K to approximately 670 K the structure is orthorhombic, and at temperatures $>$ 1360 K, the structure is the ideal cubic. Moreover, measurements of the variation of the angle of rotation of the oxygen octahedron with temperature were reported [37]. It has been found theoretically that the Hf-d and oxygen-p bands hybrize and make a mostly covalent bond whereas the Sr to oxygen bond is mostly ionic [39]. Only recently, Rossel et al. [35] measured the band gap of bulk $SrHfO_3$ to be 6.5 eV and a dielectric constant $\kappa \sim 19$.

In my calculations of bulk $SrHfO_3$, using the experimental lattice constant of the cubic structure (a=4.1131 Å, T=1403 K [37]), I have found a band gap of 4.1 eV, which is typical of the known underestimation of the band gap in density-functional calculations; another theoretical study estimated a band gap of 3.67 eV [39]. In this work, this deficiency has not been corrected. When the atomic coordinates where allowed to relax (in the cubic unit cell) the oxygen octahedra tilted in opposite directions with an angle of 11 °. This is in agreement with the fact that the structure of $SrHfO_3$ at very low temperatures is orthorhombic.

## 3.4 The $SrHfO_3(001)$ surface

In principle, there are two possible terminations of the (001) surface of the $ABO_3$ perovskite: the $AO$-terminated surface and the $BO_2$-terminated surface. In II-IV perovskites, the $AO$ and $BO_2$ layers are charge neutral, so that both types of surfaces are nonpolar and expected to be stable [40]. Nevertheless, it has been argued that the $ABO_3(001)$ surfaces are to be considered as *weakly polar* surfaces due to the fact that these compounds are not fully ionic and the covalency of the $BO_6$ bonds determines a non-vanishing macroscopic dipole moment perpendicular to the surface. The electronic structure of these surfaces is not strongly modified relative to the nonpolar case [41]. On the model system $SrTiO_3(001)$ several reconstructions have been proposed, but the unreconstructed $SrO$ and $TiO_2$ terminations are the

most stable. These studies and their relation to $SrHfO_3(001)$ are discussed in more detail in Section 3.8.

In this work, the unreconstructed $SrO$ and $HfO_2$ terminations of the $SrHfO_3(001)$ surface have both been taken into account by using two differently terminated slabs. To my knowledge there are no studies on the stability of the $SrHfO_3(001)$ surface structures or reconstructions, but they are expected to be qualitatively similar to the most stable surface structures on $SrTiO_3(001)$.

It is interesting to note that cube-on-cube epitaxy of Ge (a=5.658 Å [38]) on $SrHfO_3$ (a=4.1131 Å [37]) is not possible due to the large lattice mismatch (38 %). Nevertheless, if the primitive vectors in the plane parallel to the (001) interface are rotated by 45 °, the lattice mismatch can be reduced to 2.8 %; the lattice mismatch with Si is, however, still large (6.6 %).

## 3.5 Ge clustering on $SrHfO_3(001)$

Only recently, Seo et al. [42] have reported the direct growth of Ge on $SrHfO_3(001)$, with the oxide epitaxially grown on a Si(001) substrate. RHEED and cross-sectional TEM images, show that hemispheric Ge islands are formed on the surface with no coverage between them, and they are regularly distributed on the oxide surface. This is a confirmation of the expected three-dimensional (3D) Volmer-Weber growth mode of Ge on the $SrHfO_3(001)$ oxide. Based on the observation that the crystallinity within the islands changes with temperature towards epitaxial (above 600 °C), a two temperature-step growth process was developed and shown to produce fully epitaxial Ge films. The measured epitaxial relationship between the Ge film and the $SrHfO_3(001)$ substrate is: $(001)_{Ge} \parallel (001)_{SrHfO_3}$ and $[110]_{Ge} \parallel [100]_{SrHfO_3}$. The resulting films, however, are not suitable for transistors due to their high density of defects and low Hall-mobility. Moreover, the authors noted that during Ge growth $SrHfO_3$ remained stable at high growth temperature (690 °C) [42, 43]. No intermixing or chemical reaction between Ge and $SrHfO_3$ was observed during Ge growth and, as observed by HRTEM, the $Ge/SrHfO_3(001)$ interface is atomically sharp. This is an indication that formation of Ge alloys (germanates and germanides) is not likely to occur. The fact that formation of a Ge epilayer is possible on $SrHfO_3(001)$, although with high density of defects, will be discussed in Section 3.6 using the results from this section.

The formation of Ge islands and metastable epitaxial films on the bare $SrHfO_3(001)$ surface has been investigated from a thermodynamic and kinetic point of view. In my simulations, epitaxial Ge structures have been

obtained after relaxation. They are, however, local minima (metastable) instead of global minima since the most stable surface configuration is the Ge cluster (bulk structure). It is then important to understand the mechanism of cluster formation on the oxide surface in order to attempt to hinder it and to stabilize the epitaxial configuration instead. The elucidation of the migration mechanism (kinetics) of an isolated Ge adatom on the bare surface, and the determination of the feasibility to form epitaxial Ge films on the bare $SrHfO_3(001)$ are the main objectives of this section.

### 3.5.1 Adsorption of an isolated Ge adatom

The adsorption of an isolated Ge adatom on the bare surface was simulated by the adsorption of an ordered Ge 1/4ML film. A single Ge adatom in the unit cell, with periodicity equivalent to (2x2)Ge(001) (Section 3.4), corresponds to an ordered Ge 1/4ML coverage of the $SrHfO_3(001)$ surface[1]. In order to determine the adsorption site, the diffusion path and diffusion barriers for the isolated Ge adatom on the $SrHfO_3(001)$ surface, I have calculated the potential-energy surface $E_{tot}^{PES}(\vec{R}_{\parallel})$, where the lateral position $\vec{R}_{\parallel}$ of the adatom on the surface is kept fixed while its height and the coordinates of atoms in the first three surface layers of the slab were allowed to relax. Using this approach two potential-energy surfaces for adatom adsorption and diffusion are obtained, one for the $SrO$ and other for the $HfO_2$ surface termination.

From the PES, I find that the energetically most stable adsorption site of a Ge adatom is on top of a surface oxygen atom, for both types of termination, Figure 3.4.

The adsorption energy of the Ge adatom on $SrHfO_3(001)$ is calculated as:

$$E_{ads}^{Ge/SrHfO_3} = E_{slab}^{Ge/SrHfO_3} - \left(E_{slab}^{SrHfO_3} + E_{atom}^{Ge}\right), \tag{3.1}$$

where $E_{slab}^{Ge/SrHfO_3}$ is the total energy of the slab with the adsorbed Ge, $E_{slab}^{SrHfO_3}$ is the total energy of the clean $SrHfO_3(001)$ slab, and $E_{atom}^{Ge}$ is the total energy of the isolated Ge atom[2]. The calculated adsorption energies are -2.44 eV and -2.88 eV on the $SrO$ and $HfO_2$ terminations, respectively.

[1]The repeated images of the Ge adatom on adjacent cells are separated by 8.2 Å (the lateral size of the unit cell) in the direction parallel to the surface. As pointed out by Cohen et al. [30] in a study of the isolated $Si_2$ molecule, the interaction between the charge density of the periodic images is originated by the overlap of the wave functions and their electrostatic interaction. The former can be minimized by an image separation of 7 Å, but the latter is a long-range interaction.

[2]For adsorption that does not occur at a surface substitutional site, i.e. that does not

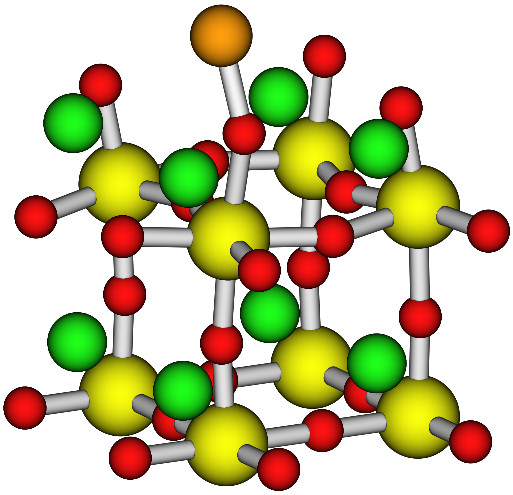

(a)

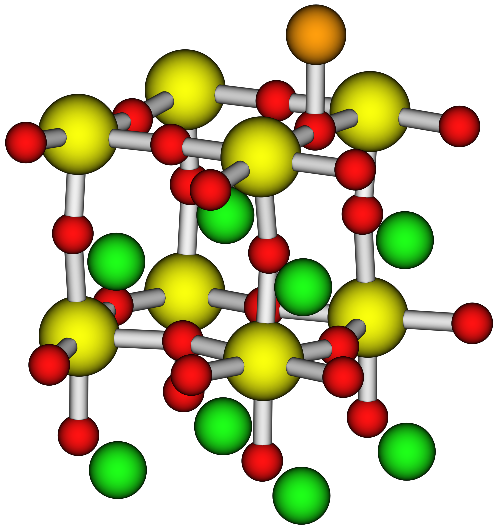

(b)

Figure 3.4: Lateral view of a Ge atom adsorbed at the oxygen site on the (a) $SrO$ surface, and (b) $HfO_2$ surface. Color scheme: Sr, Hf, oxygen and Ge atoms are green, yellow, red and orange, respectively.

The layer-projected density of states for the adsorption of a Ge atom on the $SrO$ and $HfO_2$ surface is shown in Figures 3.5 and 3.6, respectively. It can be seen that in both cases Ge makes a covalent bond with oxygen, involving the oxygen $2p$ and Ge $4s, 4p$ orbitals.

The Ge tendency to form clusters can be evaluated through the formation energy of an epitaxial film from a bulk Ge reservoir in contact with the $SrHfO_3(001)$ surface:

$$E_{clust}^{Ge/SrHfO_3} = \frac{1}{N^{Ge}}\left(E_{slab}^{Ge/SrHfO_3} - E_{slab}^{SrHfO_3}\right) - E_{bulk}^{Ge}, \tag{3.2}$$

where $N^{Ge}$ is the number of Ge atoms in the film per unit cell, $E_{slab}^{Ge/SrHfO_3}$ is the total energy of the slab with the Ge epitaxial layer, $E_{slab}^{SrHfO_3}$ is the total energy of the clean slab, and $E_{bulk}^{Ge}$ is the total energy (chemical potential) per atom in bulk Ge. The fact that Ge incorporation in $SrHfO_3$ is not observed experimentally [42], as pointed out at the beginning of this section, is reflected in Eq. (3.2) where the substrate consists entirely of $SrHfO_3$. For the isolated Ge adatom, the calculated formation energy $E_{clust}^{Ge/SrHfO_3}$, as defined in Eq. (3.2), is 1.89 eV and 1.44 eV, on the $SrO$ and $HfO_2$ terminations, respectively. The positive values mean that the energy of the isolated Ge atom adsorbed on the surface (or the energy of a Ge atom in an ordered Ge 1/4ML film formed on the surface) is higher than its energy in the bulk. This indicates that Ge will seek to form Ge-Ge bonds rather than Ge-surface oxygen bonds, and thus will form stable islands or clusters on the surface in order to minimize its energy, namely, the 3D-island (Volmer-Weber) growth mode. Since $SrHfO_3(001)$ is a chemically passivated surface, where the electrons provided by the surface metal atoms are already saturating the surface oxygen atoms, the Ge adatoms can more easily saturate its dangling bonds by making bonds among them than to make bonds to the passivated surface.

Information on the way clusters are formed on the surface can be obtained from the study of the diffusion mechanism (surface kinetics). The relevant information regarding the Ge adatom diffusion on a surface terrace is obtained from the potential-energy surface, $E_{tot}^{PES}(\vec{R}_{\parallel})$. The migration path for a Ge adatom on a terrace is determined as the path with the smallest diffusion barriers relative to the most stable adsorption site, which has previously been shown to be on top of a surface oxygen on both types of surface termination.

On the terrace with $SrO$ stoichiometry, the migration of Ge evolves across the shortest path between adjacent surface oxygen atoms, as shown in Fig-

involve the initial creation of a surface vacancy, the adsorption energy and the binding energy are equal [34].

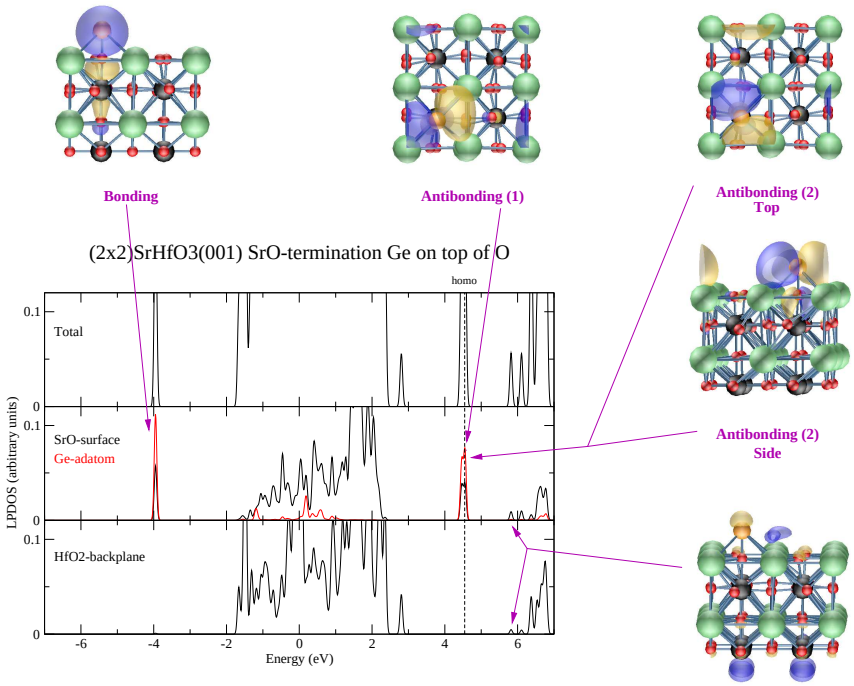


Figure 3.5: Layer-projected density of states of Ge atom adsorbed at the surface oxygen site on the $SrO$ surface. Added to the density of states are wave function plots of selected Ge-oxygen $\sigma$-bonding and $\pi$-antibonding states. The color scheme is: Sr, Hf, oxygen and Ge are green, black, red and orange, respectively.

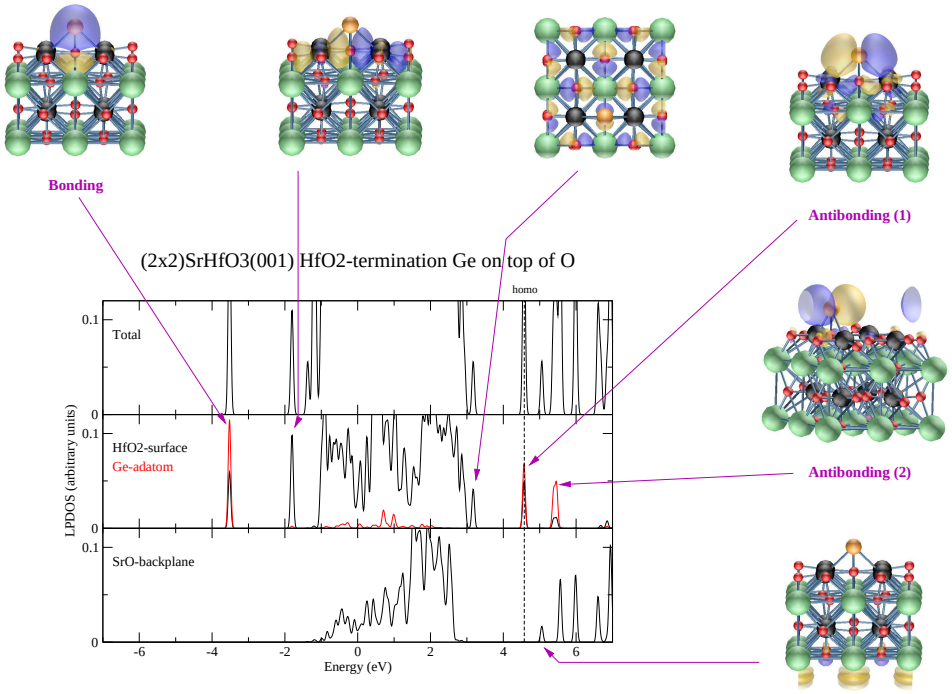


Figure 3.6: Layer-projected density of states of Ge atom adsorbed at the surface oxygen site on the $HfO_2$ surface. Added to the density of states are wave function plots of selected Ge-oxygen $\sigma$-bonding and $\pi$-antibonding states. The color scheme is the same as in Figure 3.5.

ure 3.7. At the most stable adsorption site, on top of a surface oxygen, the bond length is 1.89 Å, 3 % smaller than the sum of the covalent radii of oxygen and Ge (1.95 Å). At the middle point of this path, at the barrier configuration, the diffusion barrier is 0.53 eV. At this configuration, the Ge adatom makes bonds with two adjacent oxygen atoms with a bond length of 2.15 Å, 14 % larger than the bond length at the stable oxygen site, and 2.29 Å is the vertical distance to the surface plane (along the surface Sr atoms), 0.4 Å larger than at the oxygen site where it has the value of the bond length.

On the $HfO_2$ termination, the migration mechanism is similar to that on the $SrO$ termination, namely, along the path that connects the oxygen sites and avoids the sites on top of the surface metallic atoms. For this type of termination, I have found two paths with a small difference between their diffusion barriers, and they are shown as Path A and B in Figure 3.8. Path A has the smallest diffusion barrier and is the migration path for this surface. When the Ge adatom is at the middle point of the shortest path between two oxygen sites, at the barrier configuration along Path A, the diffusion barrier is 0.13 eV. At this barrier configuration, Ge makes bonds with two adjacent oxygen atoms with a bond length of 2.04 Å, 7 % larger than the bond length at the stable oxygen site which is 1.90 Å. The vertical separation of the Ge adatom with respect to the plane of the surface Hf atoms is smaller at the barrier configuration (1.56 Å) than at the stable oxygen site (1.90 Å).

Additionally, Path B in Figure 3.8 connects the oxygen sites but is not the shortest path (as Path A) and instead passes through the hollow sites between four oxygen atoms. At the hollow site, Ge makes bonds mainly with two of the four adjacent oxygen atoms with a bond length of 2.07 Å. The vertical separation from the surface plane is 1.71 Å, again smaller than at the stable oxygen site (1.90 Å) but 0.15 Å larger than at the barrier configuration in Path A. At the hollow site, the diffusion barrier is 0.31 eV, 0.18 eV higher than the barrier at Path A. Path B is not a second migration path but a saddle of second order. This is, however, an indication of the small corrugation of the potential-energy surface, $E_{tot}^{PES}(\vec{R}_{\|})$, on the $HfO_2$ termination.

The migration mechanism (kinetics) on a surface terrace is more efficient on the $HfO_2$ termination than on the $SrO$ termination, due to the smaller activation barriers for diffusion. Moreover, it is interesting to note that the density of Ge adsorption sites (on top of surface oxygen atoms) on a surface terrace, i.e. the number of adsorption sites per surface unit cell area, is higher on the $HfO_2$ terraces than on the $SrO$ terraces. The higher density of adsorption sites may be partly responsible for the improved Ge migration on the $HfO_2$ termination. On the other hand, the more restricted diffusion

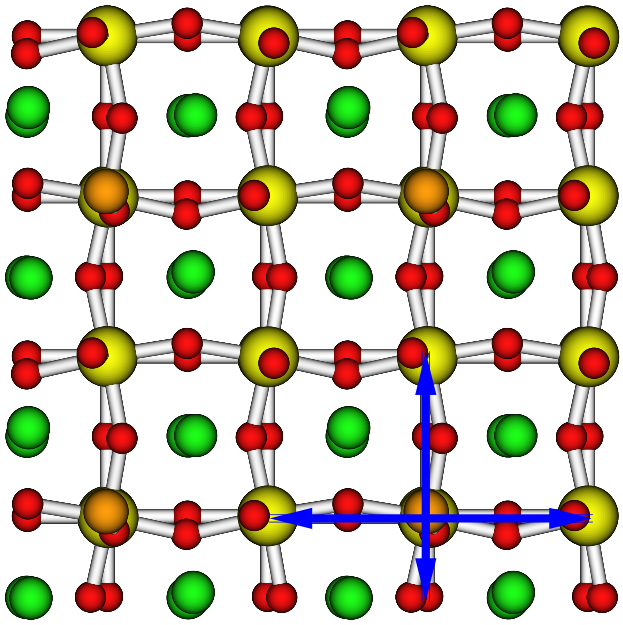

Figure 3.7: Top view of the migration path of a Ge adatom on the *SrO* surface. The color scheme is the same as in Figure 3.4.

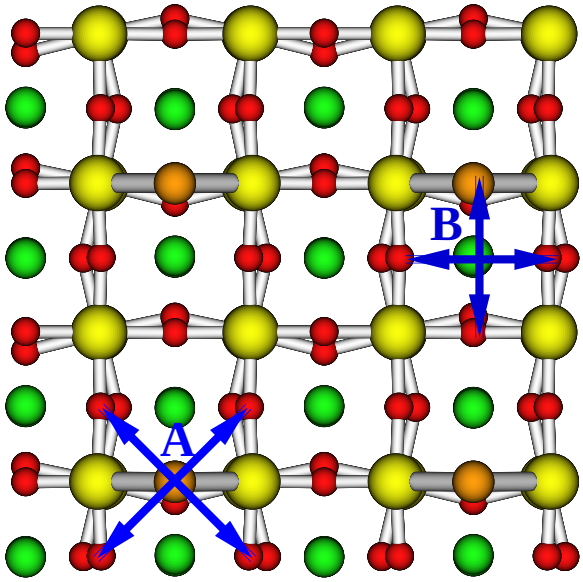


Figure 3.8: Top view of the migration path of a Ge adatom on the $HfO_2$ surface. The color scheme is the same as in Figure 3.4.

on the $SrO$ termination may affect or even hinder the formation of the stable Ge cluster structures on the surface at low temperature, as will be shown in the next section.

A passivated surface has low chemical reactivity, and on top of this inert surface the activation barrier for diffusion is expected to be low. The small diffusion barriers obtained for Ge on both surface terminations of $SrHfO_3(001)$ are in agreement with this prediction, and indicate that the Ge adatoms diffuse readily on this surface by easily breaking and forming bonds with the surface oxygen atoms. Since, as shown above, the incorporation of Ge inside the substrate is thermodynamically unfavorable and the diffusion barriers are low on the terraces, the diffusion length of the Ge adatom is expected to be large. This large diffusion length, however, should occur on an ideal non-defective surface. For instance, an oxygen vacancy on the $SrHfO_3(001)$ surface may act as a trapping site for Ge; which will be discussed in a similar context in Section 3.11.1 below.

Therefore, in order to lower its energy, an isolated Ge adatom will seek to passivate its bonds by making bonds to other Ge atoms to form clusters on the clean $SrHfO_3(001)$ surface, which confirms that the growth mode of Ge is Volmer-Weber (3D-island). The small diffusion barriers for Ge on both surface terminations favor the formation of the stable cluster structure. The Ge migration mechanism is more restricted on the $SrO$ termination. At low temperatures, the less efficient kinetics on this surface may hinder the formation of clusters.

### 3.5.2 Adsorption of Ge films

Even though Ge clusters on the clean $SrHfO_3(001)$ surface, it is interesting to study the adsorption of Ge at higher coverages. If metastable epitaxial structures (local minima) are found then they could, in principle, be stabilized by modifying the growth kinetics of Ge or modifying the surface free energy of the substrate with a suitable interface. In the calculations presented in this section, the initial Ge surface structures were epitaxial and subsequently were fully relaxed.

The Ge 1ML relaxed geometries on the $HfO_2$ termination are presented in Figures 3.9 and 3.10. It can be readily seen that the Ge adatoms do not maintain their initial epitaxial positions at 1ML and form cluster-like structures. This behavior is consistent with the efficient migration mechanism for Ge on this surface termination, and as discussed above, may be due to the non-reactive nature of the surface and the high density of Ge adsorption sites

(on top of surface oxygen atoms).

The most stable of the cluster-like Ge structures is presented in Figure 3.9. In this configuration, the average Ge bond length is 2.53 Å, 3 % larger than the bulk bond length which is 2.45 Å. The formation energy $E_{clust}^{Ge/SrHfO_3}$ for this structure, as defined in Eq. (3.2), is 0.47 eV/Ge higher than the energy for precipitation of bulk Ge on the surface, which again indicates that Ge grows as islands. Other Ge structures obtained after relaxation, which are less stable, are presented in Figure 3.10. It can be seen that the arrangement of Ge adatoms is ring-like in the first two almost degenerate-lower energy configurations (Figures 3.10(a) and 3.10(b)), while in the other two almost degenerate-higher energy configurations (Figures 3.10(c) and 3.10(d)), it is chain-like. From Figures 3.9 and 3.10, it is clear that the ring-like structures are more stable than the chain-like ones. This is consistent with the idea that a Ge adatom will seek to saturate its dangling bonds by forming bonds with other Ge adatoms rather than to the surface oxygen atoms, since in general a ring-like configuration allows for the formation of a larger number of Ge bonds than a chain-like configuration.

Performing the same procedure for Ge 1ML coverage on the $SrO$ termination, resulted in a metastable ordered structure (local minimum) made out of Ge dimers. This configuration, shown in Figure 3.11, consists of Ge dimers arranged in diagonal-rows. In turn, the epitaxial Ge(001) surface structure consists of straight-rows of dimers, and its relation to the diagonal-row configuration will be explained below.

In the diagonal-row configuration, the dimer bond length is 2.53 Å, 3 % smaller than the bond length of the surface buckled dimer in Ge(001) (2.60 Å). The diagonal-row arrangement is the result of the electrostatic repulsion among the lone-pairs in each Ge adatom. The Ge adatoms that form the dimer make bonds to the surface oxygen atoms while the dimers are oriented along the migration path on the $SrO$ surface (Figure 3.7). The formation energy $E_{clust}^{Ge/SrHfO_3}$ (Eq. (3.2)) per Ge adatom of the dimer diagonal-row configuration with respect to the bulk Ge is 0.85 eV/Ge, again the positive value indicates that the formation of a bulk Ge structure on the surface is more stable. The reduction of Ge diffusion on this surface termination compared to the $HfO_2$ termination makes the formation of a metastable dimer diagonal-row configuration possible.

An attempt to obtain a metastable epitaxial straight-row configuration, as in Ge(001), resulted in the configuration presented in Figure 3.12. This configuration is only 0.05 eV/Ge dimer less stable than the diagonal-row configuration and almost degenerate with it. Thus, it is not possible to form

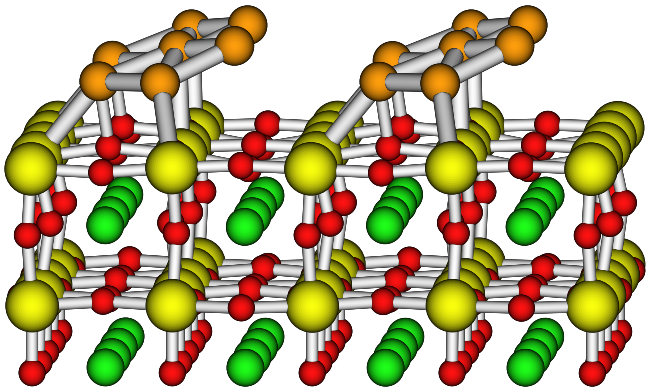

(a)

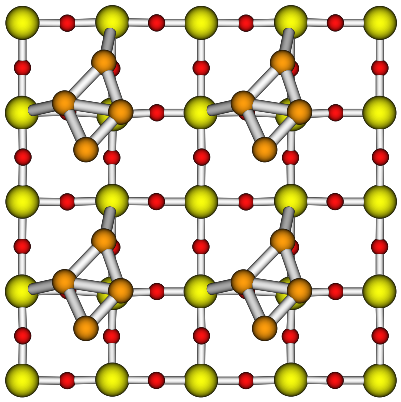

(b)

Figure 3.9: Most stable Ge 1ML structure on the $HfO_2$ surface: (a) side view, and (b) top view. The color scheme is the same as in Figure 3.4.

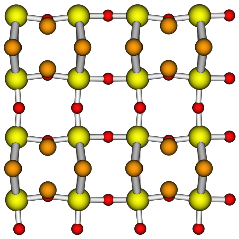

(a) $\Delta$E = 0.17 eV/Ge

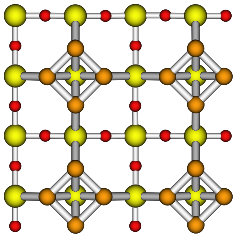

(b) $\Delta$E = 0.25 eV/Ge

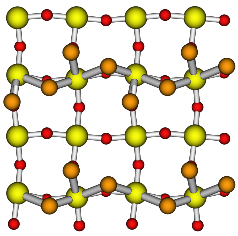

(c) $\Delta$E = 0.40 eV/Ge

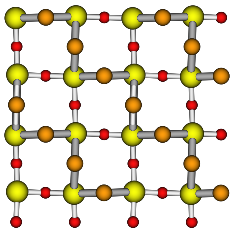

(d) $\Delta$E = 0.43 eV/Ge

Figure 3.10: Top view of relaxed Ge 1ML structures adsorbed on the $HfO_2$ surface. They are less stable than the structure in Figure 3.9, as indicated by their relative energies (per Ge atom) to this structure. The color scheme is the same as in Figure 3.4.

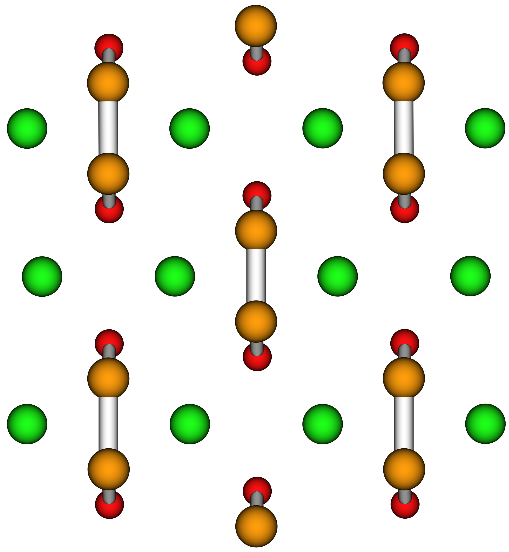

(a)

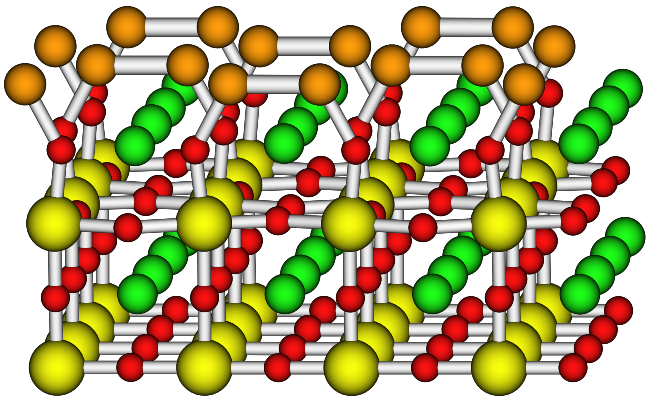

(b)

Figure 3.11: (a) Top and (b) side views of the most stable Ge 1ML structure on the *SrO* surface. The color scheme is the same as in Figure 3.4.

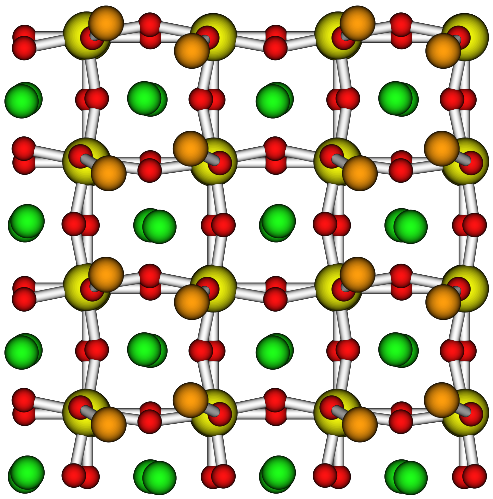

Figure 3.12: Top view of a relaxed Ge 1ML structure adsorbed obtained after initial setting of straight-rows of dimers on the $SrO$ surface.

metastable straight-rows of dimers on the $SrO$ termination.

In order to clarify the relationship between the metastable dimer diagonal-row and the epitaxial dimer straight-row configuration, the possibility of forming dimer diagonal-rows from straight-rows on the Ge(001) surface was investigated. The diagonal-row configuration is obtained by breaking every second dimer in a straight-row and bonding the Ge atoms in the neighbouring dimer rows, so that the new formed dimer lies at the valley in between straight-rows of dimers, as shown in Figure 3.13. In a (2x2) surface unit cell, the energy per dimer necessary to form diagonal-rows from straight-rows is 0.02 eV/Ge-dimer. Therefore, the dimer diagonal-row configuration is a metastable state (local minimum) of the Ge(001) surface reconstruction.

Based on the metastable Ge structure found at 1ML on the $SrO$ termination, I have investigated the possibility of forming metastable epitaxial structures at higher coverage (2ML and 3ML). These structures where obtained by initially placing each Ge atom in epitaxial sites, and then relaxing the structure. The relaxed metastable structures at Ge 2ML and 3ML coverage have dimer diagonal-rows on the surface. In the Ge 2ML metastable structure, Figure 3.14, dimer diagonal-rows are present on both layers. In contrast, the ideal epitaxial Ge 2ML configuration consists of straight-rows of dimers formed on both layers and running parallel to each other. It was not possible to obtain a 2ML metastable configuration with straight-rows of dimers on any one of the two layers.

The obtained metastable Ge 3ML configuration, Figure 3.15, consists of dimer diagonal-rows on the first monolayer and straight-rows on the surface, with the direction of the dimers perpendicular to each other, plus an unreconstructed intermediate layer. An ideal epitaxial Ge(001) 3ML film would have straight-rows of dimers on the first and third layer running perpendicular to each other while the intermediate layer is unreconstructed. As expected the formation energies $E_{clust}^{Ge/SrHfO_3}$, Eq. (3.2), of the metastable Ge 2ML and 3ML dimer diagonal-row structures are higher than the formation of clusters on the surface, by 0.34 and 0.30 eV/Ge, respectively.

In Section 3.4, it was noted that cube-on-cube epitaxy of Ge on $SrHfO_3$ is not possible but after a 45 ° rotation of the primitive vectors in the plane parallel to the (001) interface the lattice mismatch is reduced to 2.8 %. Moreover, the surface oxygen atoms on $SrHfO_3(001)$ (the Ge adsorption sites) are in registry with the Ge surface atoms on the Ge(001) film. This structural compatibility between Ge(001) and $SrHfO_3(001)$ is more easily identified on the $SrO$ termination with the appearance of metastable epitaxial structures (Figures 3.11, 3.14 and 3.15). Moreover, it is important to note that this structural compatibility also exists on the $HfO_2$ termination (discussed

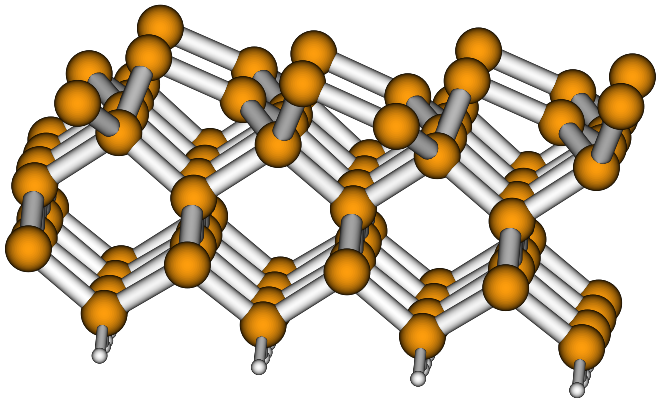

(a)

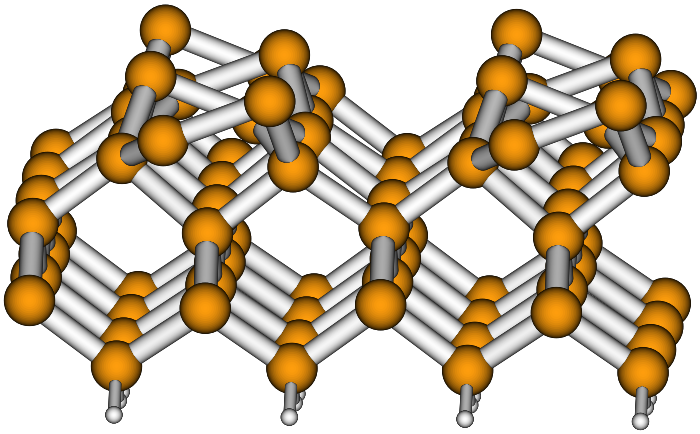

(b)

Figure 3.13: Side views of a Ge(001) surface with a (2x1) reconstruction made out of (a) diagonal-rows of dimers (metastable) and (b) straight-rows of dimers. The Ge and H atoms are orange and white, respectively.

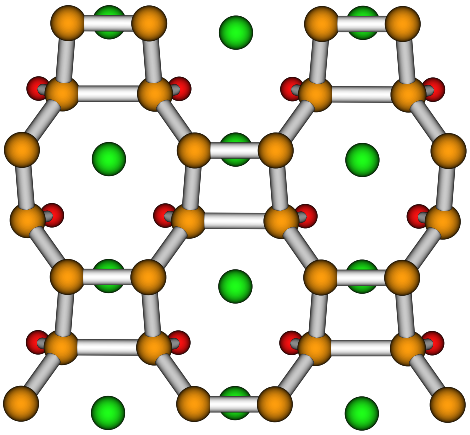

(a)

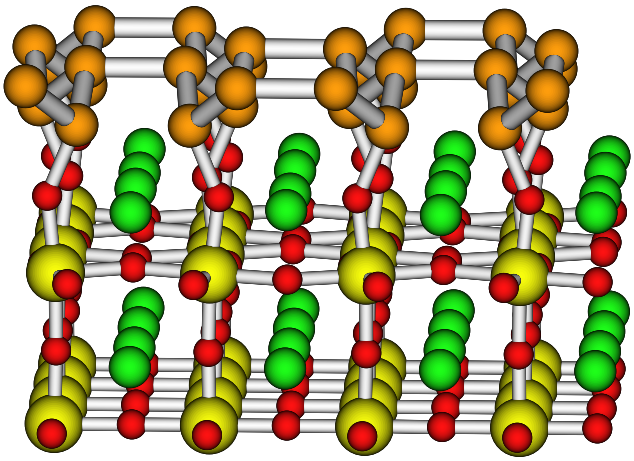

(b)

Figure 3.14: (a) Top and (b) side views of a Ge 2ML metastable relaxed structure on the *SrO* surface. Diagonal-rows of dimers are seen on the first and second monolayer. There is no dimer buckling. The color scheme is the same as in Figure 3.4.

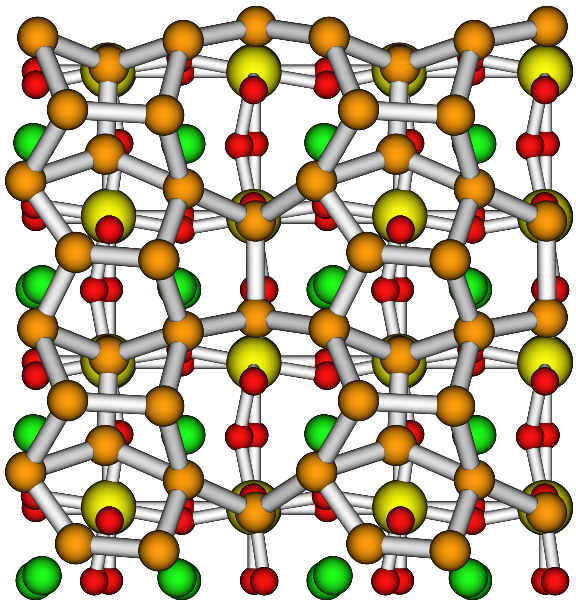

Figure 3.15: Top view of a Ge 3ML metastable relaxed structure on the *SrO* surface with diagonal-rows of dimers on the first and straight-rows of dimers on the third monolayer. There is no dimer buckling. The color scheme is the same as in Figure 3.4.

in more detail in Section 3.6.3 below). However, in my simulations at low coverages on the $HfO_2$ termination, a metastable epitaxial structure was not obtained after relaxation. This may be due to the more efficient migration mechanism on this surface and the low Ge coverage. Thus, based on the structural compatibility, similar simulations at coverages of 2ML or higher on the $HfO_2$ termination may show that the Ge epitaxial structure is metastable (local minimum). The structural compatibility is confirmed experimentally by the epitaxial relationship obtained from XRD measurements [42]: $(001)_{Ge} \parallel (001)_{SrHfO_3}$ and $[110]_{Ge} \parallel [100]_{SrHfO_3}$.

To summarize, it was confirmed that Ge does not wet the $SrHfO_3(001)$ surface, and it grows in a 3D-island (Volmer-Weber) mode. The Ge adatoms seek to minimize their energy by saturating their dangling bonds and so they prefer to make bonds to other Ge adatoms on the surface and form clusters, than to make bonds to the surface oxygen atoms. It was found that the Ge migration mechanism (kinetics) on the $HfO_2$ termination is very efficient, and at low coverages no metastable epitaxial Ge structures were obtained, only clusters. On the other hand, on the $SrO$ termination the diffusion of Ge is more restricted, and metastable epitaxial Ge(001) structures made out of diagonal-rows of dimers were obtained at several coverages. Thus, it seems that the $SrO$ surface is more suitable to attempt stabilization of the Ge epitaxial film.

## 3.6 Heteroepitaxial growth of Ge without surfactant

In this section, I will discuss the two temperature-step growth process of Seo et al. [42] for the epitaxial growth of Ge on $SrHfO_3(001)$ without surfactant. I argue that structural compatibility between the substrate and the film, and the presence of a seeding surface are key factors for the success of heteroepitaxial growth. In this context, metastable epitaxial structures become relevant.

### 3.6.1 The two temperature-step growth process without surfactant

The two temperature-step process [42] is based on the change in crystallinity within the Ge 3D-islands. These changes in crystallinity and the temperature-steps that lead to the formation of a Ge(001) epitaxial film on

$SrHfO_3$(001) are summarized below :

- Initial Ge deposition originates hemispheric 3D-islands with no coverage between them, and no reaction between Ge and $SrHfO_3$(001), at high and low growth temperatures.
- First step : Above 600 °C, the Ge islands are single-crystalline, with (001) orientation. At this high growth temperature, the islands coalesce and there is no additional nucleation [43].
- Below 500 °C, the Ge islands are polycrystalline but with the same orientation within individual islands. However, the (001) is the preferential orientation [43].
- Further Ge deposition on $SrHfO_3$(001) with already nucleated (001) oriented Ge islands (after the first step) leads to the formation of an epitaxial Ge film. Deposition temperature influences the way islands grow and coalesce, and determines the surface morphology of the film.
- Second step : At low growth temperature (350 °C), a continuous and flat Ge(001) film was obtained. Lateral growth of the islands was promoted instead of 3D-growth in order to obtain homogeneous coverage of the oxide.
- At high growth temperature, a continuous epitaxial Ge film with a rough surface morphology was obtained.

As noted by the authors, this growth process begins by seeding crystalline (001) oriented islands, at high temperature in the first step. Then the goal was to promote lateral growth of the islands to achieve homogeneous coverage of the oxide surface, at low temperature in the second step.

In this work it was also mentioned that Ge(001) and $SrHfO_3$(001) are structurally compatible in the case of an ideal 2D-surface. Although there is no cube-on-cube epitaxy, Ge(001) and $SrHfO_3$(001) become structurally compatible if one of them has an in-plane rotation of 45 °.

The observed defects in the grown Ge(001) film were mainly micro twins and stacking faults. It was noted that misfit dislocations, due to the lattice mismatch, were not observed. And that the reason for this absence may be that the epitaxial strain in the Ge film is partly relaxed by the other type of defects. It was observed that defects preferentially originated from oxide surface steps and that the defect density in the Ge film depended on the crystalline quality of the $SrHfO_3$(001) film [43]. The authors argued that the structural incompatibility between Ge(001) and $SrHfO_3$(001) at the steps

originated most of the defects on the Ge film. The starting $SrHfO_3(001)$ surface used in the experiments consisted of half and one unit cell high steps [43]. The structural compatibility between Ge(001) and $SrHfO_3(001)$ is not maintained across the steps because the diamond and perovskite structures are not compatible in the out-of-plane direction.

The measured electrical properties of the Ge film were poor. The effect of film defects on the electrical properties is still unclear. However, the importance of reducing the high density of defects in the Ge film was stressed.

Finally, the HRTEM images revealed that the $Ge/SrHfO_3(001)$ interface was atomically sharp, with no indication of an interfacial reaction.

### 3.6.2 Seeding for heteroepitaxial growth

For solid phase heteroepitaxial growth of a film on a substrate, it is necessary to have a structural template for the growing film. It might be the case that both the substrate and the film have the same crystallographic structure. For example, when Ge grows epitaxially on Si(001), from a structural point of view, the Si dangling bonds on the surface provide the tetrahedral bonding configuration necessary for growth of a (strained) Ge(001) film. In this case the Si(001) substrate is seeding the growth of the Ge(001) film. However, the growth mode of Ge on Si(001) is of the Stranski-Krastanov type, that is layer-by-layer followed by 3D-island growth. And in order to change the Ge growth mode to layer-by-layer, an additional process has to be performed. Therefore, a seeding substrate is the one that provides the necessary structural template for heteroepitaxial growth.

A seeding substrate has an arrangement of adsorption sites on its surface that is compatible with the positions of the surface atoms on the growing film. In addition, it has a chemically active surface that reacts with the adsorbed atoms to form the epitaxial film. When both the substrate and the film have the same crystallographic structure, as in the case of the Ge growth on Si(001), cube-on-cube epitaxy takes place and the structural compatibility between substrate and film is readily seen. In addition, Si(001) is a chemically active surface that reacts with Ge to form tetrahedral bonds at the interface.

In a more general case, the substrate and the growing film may have different crystallographic structures, e.g. Ge growth on a crystal oxide. In this case, even if there is structural compatibility, the bonding environment at the substrate surface may not be the most favorable for heteroepitaxial growth of the film. And additional processes may be needed to stabilize the formation of the epitaxial film.

Structural compatibility is a requirement for heteroepitaxial growth. Two structurally compatible materials may have cube-on-cube epitaxy or else an

in-plane rotation may be needed to minimize the lattice mismatch. In any case, the initial growth will result in a strained film, due to the (minimum) lattice mismatch. Ideally, a film should grow in a crystallographic direction so as to minimize its strain. At low temperatures, however, a film may grow in a metastable state with higher strain than the minimum, and a thermal process may be needed to reach the stable state with minimum strain.

The growth mode is independent of the structural compatibility between substrate and film. This means that if the film does not wet the substrate, 3D-island growth will occur even if the substrate is structurally compatible. The islands, however, can become single-crystalline and epitaxially oriented under adequate growth conditions, as in the case of the initial Ge growth on $SrHfO_3(001)$ at high temperature [42].

The structural compatibility is not affected if the interface between film and substrate is atomically sharp. But it may be affected in the case of an interfacial reaction, depending on the interfacial compound that is formed.

### 3.6.3 Stabilization of metastable Ge structures

After reviewing the main features of the two temperature-step growth process, and the main characteristics of a seeding substrate for heteroepitaxial growth, in this section I will discuss the heteroepitaxial growth of Ge on $SrHfO_3(001)$ without surfactant.

In Section 3.5 it was shown that a metastable epitaxial Ge structure exists on the $SrO$ termination of $SrHfO_3(001)$ (Figure 3.11). In order to stabilize this epitaxial structure, a common approach is to grow at low temperature. However, Seo et al. [42] showed that at low temperatures, polycrystalline Ge islands are formed, even though, (001) is the preferential orientation. It is interesting that at high temperatures, the islands coalesce (no additional nucleation), and become single-crystalline and epitaxial. In addition, it was not possible to determine from the experiments if the islands nucleate preferentially on only one type of surface termination in $SrHfO_3(001)$ [43].

I will show that the (surface of) Ge islands act as (provide) a seeding substrate for Ge. The crystalline (001) oriented islands, in turn, are possible due to the structural compatibility of Ge(001) and $SrHfO_3(001)$, and this configuration is stabilized at high temperatures. Lateral growth of the islands, at low temperature, leads to the formation of an epitaxial film. The Ge(001) film is the result of the structural compatibility and the presence of a seeding substrate.

In the following discussion, it is assumed that the $Ge/SrHfO_3(001)$ interface is atomically sharp, based on the experimental observation that no interfacial reaction occurs.

Ge(001) and $SrHfO_3$(001) are structurally compatible after an in-plane rotation of 45 ° on one of the materials. Microscopically, the Ge atoms adsorb on top of surface oxygen atoms. The arrangement of the adsorption sites on the surface is compatible with the position of the Ge atoms on the surface of an already formed (and strained) Ge(001) film. When the Ge(001) film is not formed in advance, then Ge is deposited on the oxide surface and the deposited atoms have the tendency to make bonds among them and form clusters. At low coverages, clustering is readily seen in the $HfO_2$ termination but not in the $SrO$ termination, where a metastable ordered structure (local minimum) has been identified (see Section 3.5 and Figure 3.11). There are also differences in the arrangement of the adsorption sites on the $SrO$ and the $HfO_2$ terminations of the oxide.

On the $SrO$ termination, the surface oxygen atoms are arranged in a 2D-square network with a unit cell corresponding to (1x1)$SrHfO_3$(001). And, on this termination, there is a unique possibility to accomodate the Ge atoms that are on the surface of an already formed Ge(001) film. The metastable Ge(001) 2ML (Figure 3.14) and 3ML (Figure 3.15) structures found in Section 3.5 confirm this structural compatibility. On the other hand, the arrangement of the oxygen adsorption sites on the $HfO_2$ termination is finer with a unit cell corresponding to $(\frac{\sqrt{2}}{2} \times \frac{\sqrt{2}}{2})SrHfO_3$(001). As argued in Section 3.5, the finer arrangement of the adsorption sites is responsible for the easier Ge clustering and more efficient diffusion mechanism. Nonetheless, there is structural compatibility between Ge(001) and the $HfO_2$ termination. The finer arrangement of the adsorption sites determines two inequivalent possibilities for adsorption of the Ge atoms at the surface of a Ge(001) film. At low coverages, no metastable Ge epitaxial structure was found. However, due to the structural compatibility, it is likely that such a structure is found at coverages above 2ML.

Although there is structural compatibility in the surface plane, there is no such compatibility in the out-of-plane direction, as pointed out by Seo et al. [42]. A real $SrHfO_3$(001) surface is made out of steps with different heights. The smallest surface step is half a unit cell high and corresponds to the interlayer separation, which in the bulk is 2.06 Å. On the other hand, the interlayer separation in the (001) direction in Ge bulk is 1.41 Å. Therefore, at half unit cell high steps the structural compatibility is not mantained, and the creation of defects is more likely. However, the structural compatibility in the out-of-plane direction is much more favorable across one unit cell high steps, which are also present on the $SrHfO_3$(001) surface.

The requirement for heteroepitaxial growth of Ge on $SrHfO_3$(001) in the two temperature-step process is the formation of single-crystalline (001) oriented islands. This type of island forms at any temperature but only at

high temperature all the islands are single-crystalline and (001) oriented. Then, it is this orientation of the islands on the oxide surface that seems to be the most stable.

The formed single-crystalline islands are hemispherical and there is no coverage between the islands. Inside the islands the Ge atoms have the diamond structure as in the bulk. Ideally, the atoms on the surface of an island have tetrahedrally oriented dangling bonds. The surface of the island can then be considered as a seeding surface for homoepitaxial growth of Ge. However, the two temperature-step process is far from being similar to the homoepitaxial growth on the Ge(001) surface.

Although the $SrHfO_3$(001) surface does not provide the tetrahedral bonding configuration for Ge growth, it is still structurally compatible with Ge(001) (at least in the ideal two dimensional case of a surface without steps). In agreement with this compatibility, I have found metastable Ge(001) structures on the $SrO$ termination at coverages up to 3ML (Section 3.5). Stabilization of the metastable Ge(001) film in the two temperature-step process could not be achieved by low temperature growth only (at low temperatures, polycrystalline islands are formed). But it is necessary that single-crystalline (001) oriented islands are formed first (at high temperature).

Subsequently, in the second step of the growth process, the formation of a Ge(001) flat film is achieved by lateral growth and coalescence of the islands at low temperature. In this case, low temperature growth stabilizes the metastable Ge(001) film. Thus, it appears that in the two temperature-step growth process, the stabilization of the metastable Ge(001) film could be achieved via the seeding effect of the single-crystalline (001) oriented islands. In the following sections I will discuss other processes that could be used to stabilize the Ge(001) film.

## 3.7 Surfactant for Ge heteroepitaxial growth

A method used to obtain epitaxial, flat, single-crystalline films of materials that do not grow in a layer-by-layer mode is surfactant-mediated growth. The main requirement for a surfactant is that it will segregate on top of the growing material during the deposition process. Although the mechanism for surfactant-mediated growth is still not completely understood, this method has proved successful for growth of semiconductor epitaxial films on a variety of substrates. In this section, I will discuss the feasibility of using a surfactant to stabilize the epitaxial growth of Ge on $SrHfO_3$(001).

### 3.7.1 Surfactant-mediated growth

As pointed out by Eaglesham et al. [44], a *surfactant* is "a substance that lowers surface tension, thereby increasing spreading and wetting properties" (*Encyclopaedia Brittanica*), even though it is sometimes taken to mean (in heteroepitaxial growth) a kinetic inhibitor of island formation. In heteroepitaxial growth, change of the growth mode to layer-by-layer is the best known and most studied surfactant effect. In addition, other improvements on the growth characteristics in homoepitaxial and heteroepitaxial growth, due to an added surface layer, have also been considered as the surfactant effect [44, 45]. Reduction of the surface free energy and modification of the growth kinetics by an added surface layer has long been regarded as the main energetic and kinetic factors that combine to produce the surfactant effect [8]. However, depending on the materials system and the growth conditions, reduction of the surface free energy may even produce the opposite effect [46].

In the original work of Copel et al. [8], Ge/Si heterostructures were grown in a layer-by-layer mode by means of the deposition of a monolayer of As. The growth mode of Ge on Si is the Stranski-Krastanov, which consists of the formation of a Ge wetting layer followed by random island growth; Ge wets Si but forms islands to relax the strain due to the lattice mismatch (4.0 %). On the other hand, Si growth on Ge occurs via the Volmer-Weber (3D-island) mode; Si, consequently, does not wet Ge, due to the fact that the Si surface free energy is greater than that of Ge. The observed effect of As was to change the growth mode from Stranski-Krastanov (due to strain considerations) and Volmer-Weber (surface energy considerations) to layer-by-layer. In addition, the As monolayer was seen to segregate to the surface during growth. Due to these characteristics, As was considered to act as a surfactant. Growth of high-quality, single-crystalline films of materials that would otherwise have island growth or poor epitaxy is the main application (in heteroepitaxial growth) of surface layers considered to act as surfactants. Surface layers that are used to control the characteristics of epitaxial islands [44], and to increase the efficiency of homoepitaxial growth [45] have also been regarded to act as surfactants.

Layer-by-layer surfactant-mediated growth is characterized by:

- Segregation of the surfactant to the surface of (or, equivalently, low incorporation in) the growing material. This is a requirement for a surfactant.

- Reduction of the surface free energy.

- Surface passivation of the growing material by the surfactant overlayer[3].
- The surfactant can be deposited directly on the substrate prior to the growing material, and then it has to passivate the surface of the substrate too.
- Modification of the growth kinetics to improve surface morphology.
- High sensitivity to the growth conditions and the materials system (including choice of surfactant): Diffusion on the surface can be enhanced or hindered, layer-by-layer growth may occur by step-flow or nucleation of 2D-islands, transition back to 3D-island growth mode can occur at sufficiently high temperatures.

The surfactant passivates the surface of the growing film and thus reduces the surface free energy. Chemical passivation is usually achieved by saturation of the dangling bonds on the surface. A requirement for a surfactant is the surface passivation of the growing film, independent of the way the surfactant is deposited [9]. If the surfactant is deposited prior to the growing material, then it should also passivate the surface of the substrate (as originally proposed by Copel et al. [8]). However, it has been demonstrated that the deposition of the surfactant prior to the growing material is not a requirement [9] (see below).

The driving force for segregation of the surfactant to the surface is the relative thermodynamic stability of the passivated and unpassivated surfaces. A passivated surface is expected to be more stable than an unpassivated one. Thus, a configuration where the surfactant layer is on top of the growing material should be thermodynamically more favorable than another where it is buried under the surface. An alternative way of stating this requirement is that, during growth, a surfactant must have low incorporation rate in the growing material.

It has been argued that the detailed structure of the surfactant layer adsorbed on top of the substrate influences surfactant segregation. The strength of the surfactant bond to the substrate can favor or hinder its segregation to the surface [47].

[3]In the homoepitaxial growth of GaN(0001), it has been found that deposition of one monolayer of In (or Ga) on a Ga-terminated surface, enhances surface diffusivity [45]. Configurations with at least two metal layers on top of the surface were shown to be thermodynamically stable and to improve the efficiency of GaN growth. The In (or Ga) monolayer does not passivate the Ga-terminated GaN(001) surface. The authors considered that In acted as a surfactant (and Ga as an autosurfactant) for homoepitaxial growth of GaN surfaces.

The mechanism by which the surfactant changes the growth mode into layer-by-layer is not clearly understood. The focus of attention has been on the influence of surfactants on growth kinetics. It has been observed experimentally that, depending on the materials system, layer-by-layer growth can occur by either step-flow or nucleation of 2D-islands, and depending on the growth temperature even 3D-growth can be recovered. Two opposite models for (enhanced and reduced) diffusion of arriving atoms on the surfactant-terminated surface have been considered. One is based on enhanced diffusion [46]: The surfactant chemically passivates the surface, reducing the diffusion barrier, and thus the arriving atoms diffuse more efficiently on the surfactant-passivated surface. Depending on wether the surfactant is able to passivate or not the surface steps, different growth morphologies are originated. If the surface steps are not passivated by the surfactant, then arriving atoms can exchange positions with the surfactant more easily at steps than on the terraces, and step-flow growth takes place. If on the other hand, the surfactant passivates the steps, then exchange at steps and on the terraces will be comparable, and arriving atoms may still exchange on surface terraces, creating 2D-islands. In the latter case, when strain effects are taken into account, as in heteroepitaxial growth, it is found that layer-by-layer growth occurs at low temperatures and 3D-growth occurs at high temperatures. The second model is based on reduced diffusion [48]: Due to the thermodynamic stability of the passivated surface, an arriving atom will almost immediately exchange positions with a surfactant atom on a terrace, and become incorporated below the surface (where diffusion is drastically reduced) creating 2D-islands. In this way, the system can not achieve its stable 3D-island configuration.

Alternatively, surface energy anisotropy has been proposed to influence changes in the growth mode in the presence of a surfactant [44]. After growth of Ge islands on Si(001) under special conditions in order to achieve an equilibrium configuration, it has been found that, depending on the choice of surfactant, certain facets are enhanced (stabilized) with respect to nearby orientations. It was argued that the equilibrium morphology can favor the formation of a planar film during surfactant-mediated heteroepitaxial growth.

### 3.7.2 Two examples of Ge heteroepitaxial growth with Sb as surfactant

Finally, two contrasting examples will illustrate the surfactant-mediated growth of Ge. Copel et al. [8] originally demonstrated that Ge can be epitaxially grown on Si(001) using As as surfactant. Ge has a Stranski-Krastanov

growth mode on Si and for thicknesses greater than the critical thickness (approximately 3 ML [9]) it forms 3D-islands, in order to release the strain due to the mismatch of the lattice parameters (4.0 %). The surfactant, a monolayer of As, was deposited on the Si substrate prior to Ge (it passivates both Si and Ge) and segregated to the surface during growth. In this way, epitaxial Ge/Si heterostructures were grown at 500 °C in a layer-by-layer mode. Later work on this materials system by Osten et al. [9], but using Sb as surfactant, proved that the condition of surfactant deposition on the substrate prior to Ge was not necessary. In this work, different ways of depositing the surfactant were investigated: Prior to Ge, after deposition of a 2 ML Ge layer (smaller than the critical thickness) with subsequent Ge deposition or Ge coevaporation, and a growth temperature of 450 °C. The results were equivalent, and in all-three cases it was possible to grow 30 nm thick Ge films in a layer-by-layer mode, with no observed tendency towards clustering. Surfactant-mediated growth enables the fabrication of Ge layers thicker than the critical thickness on Si(001).

On the other hand, Bojarczuk et al. [49] demonstrated epitaxial growth of Ge on $(La_xY_{1-x})_2O_3(111)$ using Sb as surfactant. The composition of the oxide was adjusted to minimize the lattice mismatch with Si(111) [50], which is the supporting wafer. Ge grows in a Volmer-Weber or 3D-island mode on $(La_xY_{1-x})_2O_3(111)$, i.e. it does not wet the oxide, in contrast to the Ge growth on Si. The growth methodology is however different from the previous example. Initially, an amorphous and uniform Ge thin layer was deposited at low temperature ($\sim$ 100 °C). Subsequently, the Ge film was epitaxially crystallized at high temperature ($\sim$ 450 °C) under an Sb flux. The amorphous to crystalline transformation occurred without surface roughening, resulting in an epitaxial, flat, single-crystalline film. On the other hand, in the absence of a surfactant flux, the obtained film is crystalline but has a rough surface. After the recrystallization process, measurements indicated the accumulation of approximately a monolayer of Sb confined to the surface.

In the two examples above, epitaxial, single-crystalline Ge films were obtained using Sb as surfactant, which was deposited after formation of a thin Ge layer. Similar growth temperatures were also used, $450 - 500$ °C (the temperature for Ge growth on the oxide is the recrystallization temperature of the final step). The substrates, Si(001) and $(La_xY_{1-x})_2O_3(111)$, have almost the same lattice constant (the oxide's tuned to that of Si), and they are structurally compatible with Ge[4], despite the lattice mismatch. On the other

[4] $(La_xY_{1-x})_2O_3(111)$ and Ge(111) are structurally compatible, and have the epitaxial relationship: $(La_xY_{1-x})_2O_3(111) \parallel Si(111)$ and $(La_xY_{1-x})_2O_3[0\bar{1}1] \parallel Si[110]$ [50].

hand, their crystallographic structures are different. The Si(001) surface has dangling bonds that provide the tetrahedral bonding configuration to the deposited Ge film, whereas, $(La_xY_{1-x})_2O_3(111)$ is a polar surface that does not provide the tetrahedral bonding configuration. In addition, Ge wets Si but does not wet $(La_xY_{1-x})_2O_3$, so the growth modes are Stranski-Krastanov and 3D-island, respectively. Taking into account the characteristics of each substrate, it is interesting to note that on the $(La_xY_{1-x})_2O_3(111)$ surface, an amorphous, uniform Ge film was deposited at very low temperatures, instead of directly trying to epitaxially grow Ge, and that the surfactant was deposited on top of this uniform, amorphous Ge film, instead of directly on the oxide substrate. It is not known whether Sb can act as surfactant if deposited prior to Ge on the substrate or if it wets $(La_xY_{1-x})_2O_3(111)$. Finally, the fact that the amorphous and uniform Ge layer was obtained at low temperature, and the epitaxial, single-crystalline, flat (rough) Ge film with (without) Sb on the surface was obtained after a thermal process, suggests that the former can be regarded as a metastable configuration and the latter as an equilibrium configuration for this system.

### 3.7.3 Sb as surfactant for heteroepitaxial growth of Ge on $SrHfO_3(001)$

Previous experimental studies demonstrated that epitaxial, flat, single-crystalline Ge layers can be grown on different substrates using Sb as surfactant. Depending on the materials system, the surfactant has been deposited either before or after the Ge film with careful control of the growth conditions. In this section, I will discuss the feasibility of using Sb for layer-by-layer growth of Ge on $SrHfO_3(001)$. First, the effect of using Sb on an already formed Ge film will be discussed, taking into consideration experimental evidence. Finally, the feasibility of forming an ordered Sb film on $SrHfO_3(001)$, for surfactant-mediated layer-by-layer growth of Ge, will be investigated by first principles simulations.

The feasibility of using Sb as surfactant after deposition of the Ge film is discussed taking into consideration two representative experimental studies already reviewed in Section 3.7.2, namely, the epitaxial growth of Ge on $(La_xY_{1-x})_2O_3(111)$ and on Si(001). Important similarities between these materials systems and Ge on $SrHfO_3(001)$ are the structural compatibility between the Ge epitaxial film and the substrate (Section 3.6.3) and the passivation of the epitaxial Ge surface with Sb. The method of Bojarczuk et al. [49] starts with the deposition of a uniform and amorphous Ge layer on $(La_xY_{1-x})_2O_3(111)$ at low temperature followed by epitaxial crystallization

of Ge at high temperature under an Sb flux. On the other hand, stabilization of layer-by-layer growth of Ge with Sb as surfactant has been demonstrated on Si(001), independent of whether the surfactant is deposited prior or after formation of a thin Ge film [9]. Deposition of Ge on $SrHfO_3$(001) at low temperature leads to the formation of polycrystalline islands as observed by Seo et al. [42] instead of an amorphous film (Section 3.6.1). Moreover, Seo et al. [42] reported that a smoothening of the growth front by growing Ge beyond a critical thickness (as in the work of Guha et al. [50]) was not observed. And that a transformation to an epitaxial flat film by the recrystallization method of Bojarczuk et al. [49] using Sb as surfactant could not be obtained. The fact that an epitaxial Ge film was not obtained after growth at high temperature under (or not) an Sb flux, may be due to the early formation of Ge islands and/or the lack of a suitable interface that stabilizes the epitaxial film[5]. As reported by Eaglesham et al. [44] in the study of surfactant-mediated morphology changes in Ge islands formed on Si(001), deposition of Sb after formation of Ge islands may not change the morphology of the islands to flat layers. Therefore, layer-by-layer growth using Sb as surfactant starting from already formed Ge islands may not be possible. On the other hand, if an epitaxial Ge film can be formed, then Sb can in principle be used together with a thermal process to improve the quality of the film, e.g. surface roughness and density of defects, analogous to the study of Bojarczuk et al. [49] with and without surfactant (Section 3.7.2). Therefore, it would be interesting to study the effect of Sb and a thermal process on the growth mode and the quality of the epitaxial Ge film formed after the two temperature-step growth of Seo et al. [42], which has not yet been attempted [51].

When Sb is deposited on the $SrHfO_3$(001) substrate prior to Ge, it is not known whether Sb wets $SrHfO_3$(001) and subsequently can segregate to the surface to act as surfactant for Ge heteroepitaxial growth. It is important to determine if ordered structures (thin films, patterns) of Sb can be formed on the oxide surface. These structures could be used as templates for Ge overgrowth and could modify the energetics of and kinetics on the surface in such a way that surfactant-mediated Ge layer-by-layer growth is achieved. Below I present my results and discuss the feasibility of forming ordered thin films of Sb on the $SrHfO_3$(001) surface.

In order to determine the feasibility of using Sb as surfactant for Ge layer-

[5] A suitable $Ge/SrHfO_3$(001) interface may stabilize the epitaxial, single-crystalline Ge film configuration at high temperature. Such an interface may be determined by the atomic structure of the starting substrate (surface reconstruction or deposited ordered thin film) to be used as template for epitaxial growth.

by-layer heteroepitaxial growth, I have studied the deposition of Sb 1ML and 2ML on the $SrO$ termination of $SrHfO_3(001)$. This termination seems to be the most suitable for epitaxial growth of Ge due to the favorable arrangement of the adsorption sites on the oxide surface, as discussed in Section 3.6.3. The details of the calculations are explained in Section 3.2.

Similar to the deposition of Ge 1ML on the $SrO$ surface (Section 3.5), the possibility of forming metastable ordered Sb 1ML structures (local minima) was first investigated. If such a structure is found, growth of it at low temperature could be attempted. The starting configuration of Sb 1ML consisted of Sb atoms adsorbed on top of surface oxygen atoms, as these have been determined to be the reactive sites on the oxide surface. Relaxation of this structure resulted in immediate clustering of the Sb atoms, as shown in Figure 3.16(a). An attempt to obtain an ordered structure made out of dimers, identical to that of Figure 3.11, resulted in the formation of a chain, Figure 3.16(b). This indicates that formation of an ordered Sb structure (or stabilization of a metastable ordered structure at low temperature) on the $SrO$ surface is difficult.

From a chemical point of view, the driving force for Sb clustering on the $SrHfO_3(001)$ surface is similar to that of Ge (Section 3.5). An Sb atom has three unsaturated bonds (one less than Ge) and seeks to saturate them by making bonds with other Sb atoms rather than to the low reactive $SrHfO_3(001)$ surface. The easy formation of Sb clusters on the $SrO$ surface described above, indicates that the diffusion barriers are smaller than for Ge, which contributes kinetically to the rapid formation of Sb clusters.

To study the feasibility of formation of an ordered Sb 2ML film, it was taken into consideration that the bulk crystal structure of Sb is rhombohedral, which is quite close to a simple cubic lattice distorted along a body diagonal [10]. Thus, the starting structure for Sb 2ML was build similar to an epitaxial Ge 2ML film although without surface dimers, with the atoms on the first layer (the interface) adsorbed at oxygen sites and the atoms on the second layer (the surface) forming a covalent angle of 71.1 ° and a bond length of 3.5 Å (26 % larger than twice the covalent radius of Sb). Relaxation of this structure resulted in the formation of diagonal rows of dimers at the interface and straight rows of dimers at the surface, Figure 3.17. The bond length between atoms at the interface and surface is 2.90 Å, while the bond length of the dimers is 3.07 Å and 2.99 Å at the interface and surface, respectively. Most importantly, the Sb atoms at the interface detached from the oxygen adsorption sites which resulted in low adhesion of the film to the substrate. This can be explained by the fact that both surfaces of the Sb 2ML film are passivated and non-reactive, and are in contact with the low reactive $SrHfO_3(001)$ surface. Thus, even though an ordered Sb 2ML

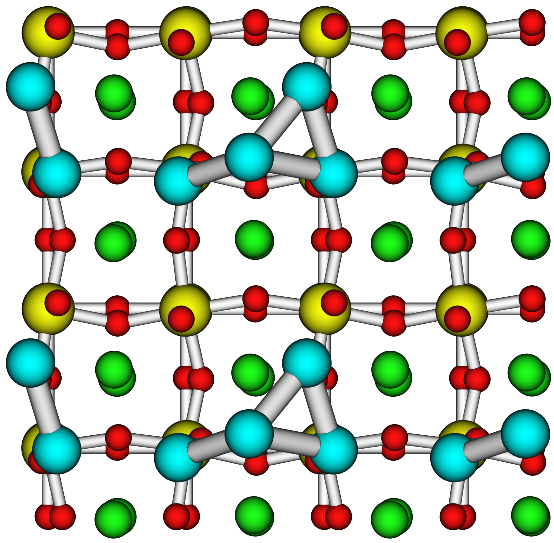

(a)

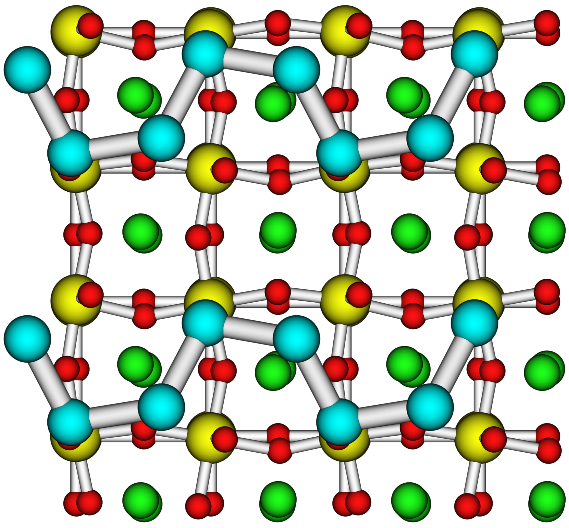

(b)

Figure 3.16: Top view of two relaxed surface structures of Sb 1ML on the $SrO$-terminated $SrHfO_3(001)$ surface. (a) Initial structure with Sb atoms adsorbed on surface oxygen sites. (b) Initial structure with Sb atoms forming dimer rows on the surface. The Sb atoms are light blue.

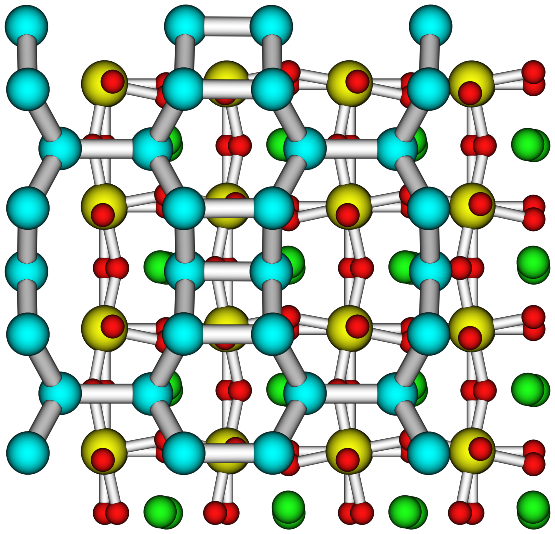

(a)

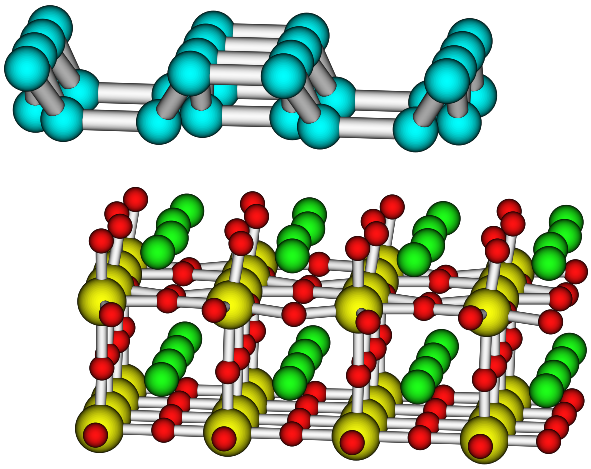

(b)

Figure 3.17: (a) Top and (b) Side views of a relaxed Sb 2ML film with the diamond structure. The Sb film seems to have detached from the $SrO$-terminated $SrHfO_3(001)$ surface. The color scheme is the same as in Figure 3.16.

configuration has been found, it may detach easily from the oxide surface.

It has been shown that Sb does not wet the $SrHfO_3(001)$ substrate, and may even have low adhesion to it. Consequently, formation of ordered Sb structures on the surface, to be used as template for Ge overgrowth, is difficult. These ordered structures could in principle modify the growth mode and growth kinetics of Ge on the surface in order to stabilize the Ge epitaxial film or to achieve epitaxial layer-by-layer growth. Therefore, deposition of Sb prior to Ge on the $SrO$-terminated $SrHfO_3(001)$ surface, does not lead to epitaxial Ge layer-by-layer growth.

### 3.7.4 Can Sr be considered as a surfactant?

In Section 3.5, it was argued that, from a chemical point of view, the formation of Ge clusters on the oxide surface is driven by the Ge preference to make bonds to another Ge adatoms rather than to the surface oxygen atoms, which are, formally, chemically passivated by the surface Sr or Hf atoms in the same oxide layer. In addition, metastable, epitaxial Ge structures were found to exist on the $SrO$ termination of the $SrHfO_3(001)$ surface. If the $SrHfO_3(001)$ surface is only $SrO$ terminated, and this surface termination is completely unoxidized, then a new $Ge/SrHfO_3(001)$ interface (Sr 1ML) will be created. Does the new interface stabilizes the formation of the Ge epitaxial film on the $SrHfO_3(001)$ surface? Would Sr act as surfactant for layer-by-layer growth of Ge? And does the $Ge/SrHfO_3(001)$ heterostructure determine good transistor properties? These are the main questions that I will address in the next sections. In this section, I will present simple arguments and examples for a similar materials system that support the idea of using Sr for layer-by-layer growth of Ge on $SrHfO_3(001)$.

Removing the oxygen atoms from the $SrO$ surface is equivalent to depositing a Sr 1ML film on the $HfO_2$ terminated surface. If the Sr 1ML film is grown on $SrHfO_3(001)$ (including both surface terminations), then a new highly reactive surface might be created. It can be expected that the Ge tendency to form clusters on this new Sr-covered surface would at least be weakened. Because Sr is very electropositive (electronegativity is 0.95 Pauling's), the Sr 1ML film will provide plenty of electrons that could passivate the Ge adatoms. Whether a stable Sr 1ML film can be formed on the $SrHfO_3(001)$ surface and it stabilizes the growth of the Ge epitaxial film remains to be proved and will be discussed in the next sections. Due to the 3D-island growth mode of Ge on the oxide, the initial stage of Ge growth is arguably the most delicate and decisive part of the entire growth process, and the determination of an adequate surface template for Ge growth is the

most important.

A very important theoretical result for this argumentation was the study of the Sr-interfaces of the $SrTiO_3/Si(001)$ heterostructure by Först et al. [52]. In this work, it was demonstrated that an Sr 1/2ML interface passivates the Si dangling bonds at the interface, thus unpinning the Fermi level. And oxidation of this Sr 1/2ML interface, produced adequate band offsets for transistor applications. Thus, control of the structure and composition of the interface can determine the transistor properties. Furthermore, these interface structures were shown to be good templates for oxide growth and chemically stable in contact with Si, moreover, they reproduced the main features of the Z-contrast images, obtained by McKee et al. [53], of the real interface. The use of Sr to produce an stable and adequate interface for transistors, has been exploited in this work. Analogous to $SrTiO_3/Si(001)$, an interface of the Sr 1/2ML type may stabilize the epitaxial $Ge/SrHfO_3(001)$ heterostructure, by minimizing the interfacial energy, and determine good transistor properties. Whether Sr 1/2ML is a good template for heteroepitaxial growth of Ge, in contrast to Sr 1ML as argued above, will be investigated in the next sections.

Studies of the growth of (wetting) single-crystalline perovskite oxides on Si and Ge substrates have established the necessity to understand and control the initial formation of the oxide/semiconductor interface, which will serve as template for the oxide overgrowth [53]. Thus, formation of ordered structures of alkaline earth metals on the clean semiconductor surface, with the additional requirement of surface passivation (necessary for transistor applications), are still the subject of experimental and theoretical studies. In the theoretical study of the Sr deposition on Si(001) by Ashman et al. [54], it was found that the (2x1) surface reconstruction at Sr 1/2ML is the only Sr-covered surface structure without states in the band gap of Si. In this reconstruction, all the dangling bonds of the Si(001) surface are passivated by Sr 1/2ML and, consequently, the formation of straight rows of unbuckled dimers is observed. A similar passivation effect is expected for the Ge(001) surface and, in principle, it could be used in the context of (at least homoepitaxial) surfactant-mediated growth of Ge using Sr 1/2ML as surfactant. But there are additional requirements for a surfactant, e.g. segregation to the surface, favorable modification of growth kinetics, that will be discussed in the next sections. It is interesting to note that Sr has a large atomic radius compared to that of Ge, so it should easily segregate to the surface during growth. On the other hand, Sr could also promote oxidation of the semiconductor surface, as argued by Franciosi et al. [55] for a more general case.

Therefore, in the context of surfactant-mediated layer-by-layer growth of

Ge on $SrHfO_3(001)$, there are indications that Sr could be used as a template for Ge overgrowth, determine an stable interface with good transistor properties, and act as surfactant for Ge epitaxial layer-by-layer growth.

## 3.8 Formation of Sr 1ML film on $SrHfO_3(001)$

As pointed out in Section 3.4, the structure of the (001) surface of $SrTiO_3$-a standard model for oxides with a perovskite structure-has been widely studied, and many reconstructions and structural transformations have been observed under various experimental conditions (of gas environment, pressure, temperature). The models proposed to understand and determine the surface structures are sometimes contradictory, moreover, many of these surface reconstructions are believed to be thermodynamically unstable (see Ref. [56] and references therein). Kubo and Nozoye [57] observed the coexistence of Sr-based clusters and ordered structures on the $TiO_2$-terminated surface at temperatures above 1000 °C, and proposed a Sr-adatom model to explain most of the observed reconstructions. This model consists of ordered Sr adatoms at the oxygen fourfold sites of a $TiO_2$-terminated layer. Liborio et al. [58] investigated, theoretically, the thermodynamic stability of many of the Sr-adatom structures. They found that the low coverage Sr-adatom structures ($\theta < 0.20$) were unstable, and the higher coverage structures were stable only when the surfaces were close to equilibrium with SrO. Thus, on the $SrTiO_3(001)$ model surface, fabrication of ordered Sr structures on the $TiO_2$ termination may be hindered by the formation of bulk $SrO$. On the other hand, to my knowledge, little is known about the formation of ordered Sr structures on the $SrO$ termination.

The crystal structure of bulk Sr is *face centered cubic* and is stable at room temperature. The lattice constant is 6.08 Å [10], so cube-on-cube epitaxy with cubic $SrHfO_3$ (4.1131 Å [37]) is not possible. However, if the primitive vectors in the plane parallel to the (001) interface are rotated by 45 °, the lattice mismatch between Sr (4.30 Å) and $SrHfO_3$ can be reduced to 4.5 %. Thus, if Sr wets $SrHfO_3(001)$, the growth mode may well be Stranski-Kastranov, that is, initial layer-by-layer growth with subsequent islanding due to the compressive stress on the Sr film. In this section I will study the feasibility of forming a Sr 1ML or Sr 1/2ML film on the $SrHfO_3(001)$ surface, to be used as template for Ge heteroepitaxial growth.

### 3.8.1 The isolated Sr adatom

Knowledge of the adsorption and diffusion mechanism of an isolated Sr adatom on the $SrHfO_3(001)$ surface enables an understanding of the initial stages of growth and the possible difficulties for the formation of the Sr film. Analogous to the adsorption of Ge (Section 3.5), the adsorption of an isolated Sr atom was simulated by the adsorption of Sr 1/4ML. This coverage corresponds to the adsorption of one Sr atom within the (2x2) surface unit cell, with a separation between Sr adatom images of 8.22 Å in the direction parallel to the surface. The Sr adatom deposition was simulated on the $SrO$ termination only, and the potential-energy surface $E_{tot}^{PES}(\vec{R}_{\parallel})$ was calculated in order to determine the adsorption site and the migration mechanism, using the procedure described in Section 3.5 for the isolated Ge adatom.

On the $SrO$ termination, the most stable Sr adsorption site is on top of a surface oxygen atom. At the oxygen site, the bond length is 2.29 Å, which is 15 % smaller than the sum of the Sr and oxygen covalent radii (2.64 Å). The Sr adatom diffuses along the shortest path that connects the oxygen adsorption sites. At the midpoint between two oxygen sites along the migration path (the bridge site), is the so-called barrier configuration, which determines the diffusion barrier. At the barrier configuration the bond length is 2.58 Å, 13 % larger than the bond length at the oxygen site, and the diffusion barrier is 0.65 eV.

Analogous to Eq. (3.1), the formation energy of the Sr surface structure on the $SrHfO_3(001)$ substrate with respect to free Sr atoms is defined as:

$$E_{atom}^{Sr/SrHfO_3} = \frac{1}{N^{Sr}}\left(E_{slab}^{Sr/SrHfO_3} - E_{slab}^{SrHfO_3}\right) - E_{atom}^{Sr}, \qquad (3.3)$$

where $N^{Sr}$ is the number of Sr atoms in the adsorbed film (not in the $SrO$ layers of the $SrHfO_3(001)$ substrate) per unit cell, $E_{slab}^{Sr/SrHfO_3}$ is the total energy of the slab with an adsorbed Sr epitaxial layer, $E_{slab}^{SrHfO_3}$ is the total energy of the slab containing the clean $SrHfO_3(001)$ substrate, and $E_{atom}^{Sr}$ is the total energy of a free Sr atom (in the gas phase). $E_{atom}^{Sr/SrHfO_3}$ can be associated with the formation of an Sr film during molecular beam epitaxy, and it takes into account the creation of both interfacial and intralayer bonds in the heterojunction [59]. In my simulations, the adsorption energy of the isolated Sr adatom is obtained from Eq. (3.3) with $N^{Sr} = 1$. The intralayer interactions within the Sr 1/4ML film are included but they are expected to be small, and so the interfacial interaction (or the interaction of the adsorbed atom with the surface) should be the main contribution to the value of $E_{atom}^{Sr/SrHfO_3}$. The calculated adsorption energy for the isolated Sr adatom is equal to -1.09 eV, on the $SrO$ termination.

The tendency to form Sr clusters instead of an epitaxial film on the surface, can be evaluated by comparing the energy of Sr adsorbed on the oxide surface to the energy in bulk Sr (when this reservoir is in contact with the surface). Thus, the formation energy of the Sr film is:

$$E_{clust}^{Sr/SrHfO_3} = \frac{1}{N^{Sr}}\left(E_{slab}^{Sr/SrHfO_3} - E_{slab}^{SrHfO_3}\right) - E_{bulk}^{Sr}, \tag{3.4}$$

where the notation is the same as in Eq. (3.3), and $E_{bulk}^{Sr}$ is the total energy per atom in bulk Sr (chemical potential). For an isolated atom ($N^{Sr} = 1$) on the $SrO$ termination, the formation energy $E_{clust}^{Sr/SrHfO_3}$ is 0.24 eV. Although this value is positive, indicating that in principle Sr has a tendency to form clusters on the surface, it is small and so the formation of an ordered Sr (1/4ML) film may still be marginally stable; in contrast, for the isolated Ge atom (Ge 1/4ML) adsorbed on the $SrO$ termination, the value of a similarly defined formation energy, Eq. (3.2), is not small and equal to 1.8 eV (Section 3.5).

In order to determine more precisely the stability of the studied surface configurations in thermodynamic equilibrium with matter reservoirs (e.g. bulk Sr, $SrO$ oxide), a more detailed analysis considering the variation of the Sr and oxygen chemical potentials within a range of allowed values may be necessary (as for example in Refs. [56] and [59]).

Note that the energy window between diffusion and adsorption/desorption is relatively small, 0.44 eV. Therefore, careful handling of the experimental conditions is likely needed to achieve the formation of the stable configuration.

### 3.8.2 The Sr 1/2ML surface configuration

Next, I study the feasibility of forming a Sr 1/2ML template for Ge overgrowth on the $SrO$ termination of $SrHfO_3(001)$. The Sr 1/2ML coverage is simulated by the adsorption of two Sr atoms in the (2x2) surface unit cell. The stable configuration is obtained by adsorbing one atom at the oxygen site and the second atom is adsorbed at any of the non-equivalent oxygen sites within the unit cell (including adsorption at the same site of the first atom). The initial position of the second atom is high above the surface (no less than 4.25 Å), and the structures were relaxed without constraints on the surface atoms (only the bottom layer was frozen in the bulk configuration).

On the $SrO$ termination, the calculated equilibrium structure at Sr 1/2ML is a chain, shown in Figure 3.18(a). In this configuration, the distance between Sr adatoms is 4.08 Å (half the surface unit cell length), and the bond length (to the surface oxygen atom) is 2.34 Å, 2 % larger than the bond length

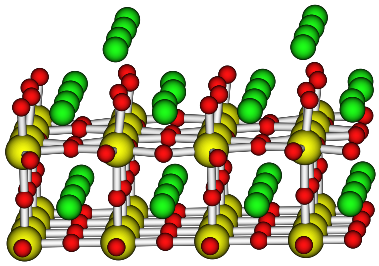

(a)

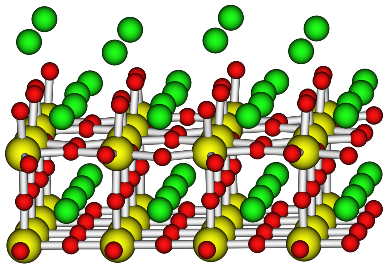

(b)

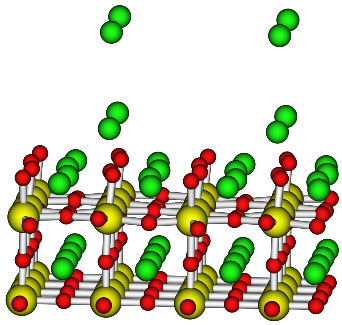

(c)

Figure 3.18: Side view of three surface structures of a Sr 1/2ML film formed on the $SrO$-terminated $SrHfO_3(001)$ surface. (a) Equilibrium structure. (b) Structure almost degenerate with (a). (c) Metastable structure. The color scheme is the same as in Figure 3.4.

of the isolated Sr adatom. The same configuration was obtained when the second atom was initially positioned above the bridge site and then relaxed. Another almost degenerate structure, 0.12 eV per *adsorbed* Sr (eV/Sr) higher in energy, was obtained. It is shown in Figure 3.18(b), and the Sr atoms are adsorbed at opposite oxygen sites within the unit cell. The distance between adatoms is 5.82 Å and the bond length is 2.35 Å. This configuration was again obtained after relaxing a structure with the second adatom initially positioned on top of a surface Sr atom. A third structure, 0.61 eV/Sr higher in energy, consists of two Sr atoms adsorbed at the same oxygen site, one on top of the other (Figure 3.18(c)). The (vertical) distance between adatoms is 4.73 Å (24 % larger than twice the covalent radius of Sr), and the distance to the surface is 7.02 Å (the size of the vacuum is still larger than 8 Å).

The formation energy of the Sr 1/2ML film relative to free Sr atoms ($E_{atom}^{Sr/SrHfO_3}$) is obtained from Eq. (3.3) with $N^{Sr} = 2$. It is equal to $-1.13$ eV/Sr for the calculated stable configuration, Figure 3.18(a), and is only 0.04 eV lower than the adsorption energy of the isolated Sr adatom (Sr 1/4ML). This indicates that the intralayer interaction in the Sr 1/2ML film is weak or at least not significantly different from that at Sr 1/4ML coverage.

The value of $E_{clust}^{Sr/SrHfO_3}$, Eq. (3.4), for the Sr 1/2ML film is equal to 0.19 eV/Sr, and it is similar to that obtained for the isolated Sr adatom. This indicates that in thermodynamic equilibrium, bulk Sr is (slightly) more likely to form on the surface than an ordered Sr 1/2ML film. Nevertheless, as pointed out above, experimental conditions should be carefully chosen in order to achieve the equilibrium configuration. It is interesting to note that although the process of Sr adsorption on the oxide surface is favorable ($E_{atom}^{Sr/SrHfO_3} < 0$), this surface configuration at Sr 1/2ML coverage (Figure 3.18(a)) may not be thermodynamically stable ($E_{clust}^{Sr/SrHfO_3} > 0$) relative to formation of bulk Sr on the surface.

Therefore, it is not clear whether an ordered Sr 1/2ML film, to be used as template for Ge epitaxial growth on $SrHfO_3$(001), can be formed on the $SrO$ termination, due to the fact that this surface structure seems to be stable only when the substrate is in or very nearly in equilibrium with bulk Sr.

### 3.8.3 The Sr 1ML surface configuration

At Sr 1ML coverage, on the $SrO$ termination, the stable configuration consists of Sr adatoms occupying all the surface oxygen sites on the (2x2) surface unit cell. In this configuration the equilibrium bond length to a surface oxygen atom is 2.43 Å, 6 % larger than in the isolated Sr adatom (Sr

1/4ML film).

The value of $E_{atom}^{Sr/SrHfO_3}$ for the Sr 1ML film is obtained from Eq. (3.3) with $N^{Sr} = 4$, and is equal to -1.39 eV/Sr. It is 0.26 eV/Sr lower than that of the Sr 1/2ML film, and indicates further stabilization due to the agglomeration of Sr atoms. In contrast, when the coverage was increased from 1/4ML (model for isolated adatom) to 1/2ML, the decrease in energy per adsorbed Sr was very small. $E_{atom}^{Sr/SrHfO_3}$ can also be associated with the energy per Sr adatom necessary to atomize an Sr 1ML film or a cluster of 1ML thickness (two dimensional-island) into free Sr atoms (1.39 eV/Sr).

For the Sr 1ML film, $E_{clust}^{Sr/SrHfO_3}$, Eq. (3.4), is equal to -0.06 eV/Sr. It is negative, indicating in principle wetting, but still too small to be conclusive. Thus, the possibility that Sr grows in clusters instead of layer-by-layer on the oxide surface can not be discarded.

Therefore, in order to determine the feasibility of forming an ordered Sr 1ML film on the $SrO$ termination, a more detailed study of the thermodynamic stability of this and other relevant surface structures as function of the Sr and oxygen chemical potentials may be necessary. Nevertheless, as pointed out by Bottin and Finocchi [59], a surface structure that is not stable, whatever the external chemical environment, can be, in principle, stabilized by growth of an overlayer.

### 3.8.4 Process of formation of Sr 1ML

Although the formation of ordered Sr structures on the $SrO$ termination may not be thermodynamically favored relative to bulk Sr at the initial stages of growth, other growth processes can aid in determining or even stabilizing such an ordered structure. For instance, I have studied the growth of the second Sr monolayer. This process can be considered to occur on top of an already formed Sr two dimensional-island of 1ML thickness. Durig molecular beam epitaxy, Sr atoms can be adsorbed on top of forming two dimensional-islands and may form the second monolayer.

An isolated Sr adatom in the second monolayer (Sr 5/4ML), on the $SrO$ termination, adsorbs at the hollow site in between four Sr atoms of the first monolayer. The distance to the oxide surface is 5.75 Å. The average bond length between the adatom and the Sr atoms on the first monolayer is 4.24 Å, 11 % larger than twice the covalent radius of Sr. Analogous to the adatom diffusion on the bare $SrO$ surface, the adatom on the second monolayer diffuses along the shortest path that connects the hollow adsorption sites (instead of the surface oxygen sites). At the midpoint between two hollow sites (bridge site) is the barrier configuration that defines the diffusion barrier.

At this configuration, the bond length to the nearest Sr atoms is 4.08 Å, and the distance to the oxide surface is 6.16 Å. The diffusion barrier is 0.20 eV. This small diffusion barrier indicates that the Sr adatoms on the second monolayer are highly mobile, and that the bond between the adatoms and the Sr atoms in the first monolayer is weak.

The value of $E_{clust}^{Sr/SrHfO_3}$, Eq. (3.4) with $N^{Sr} = 5$, for this surface configuration is equal to 0.08 eV/Sr, and it is too small to be conclusive regarding Sr wetting of the substrate.

For this surface configuration, $E_{atom}^{Sr/SrHfO_3}$, Eq. (3.3) with $N^{Sr} = 5$, is equal to -1.24 eV/Sr, and represents the energy per Sr gained when free Sr atoms (in the gas phase) adsorb on the surface and form this configuration. If this chemical reaction can be reversed, then the energy necessary to atomize the formed Sr 5/4ML film is 1.24 eV/Sr.

On the other hand, an estimate of the adsorption energy of the isolated Sr adatom in the second monolayer can be obtained by modifying Eq. (3.3) in order to consider the first Sr monolayer as part of the substrate. In this way, $E_{slab}^{SrHfO_3}$ will be replaced by the total energy of the slab with an adsorbed (and ordered) Sr 1ML film, and $N^{Sr} = 1$. The calculated value is then equal to -0.66 eV. The adsorption energy of the isolated Sr adatom on the bare oxide surface is 0.43 eV lower. Thus, if the surface is not completely covered and Sr clusters of 1ML thickness exist, a free Sr atom will preferentially adsorb on the bare surface than on top of a Sr cluster in order to minimize its energy. In addition, the value of $E_{atom}^{Sr/SrHfO_3}$ for the Sr 1ML film is 0.73 eV/Sr lower than the adsorption energy of an isolated adatom in the second monolayer. This means that a free Sr atom will lower its energy even more, by 0.30 eV/Sr, when incorporating in a Sr 1ML film instead of on the bare oxide surface. Such a process is possible if there are free sites within the Sr film (Sr coverage is almost one monolayer) and a free Sr atom adsorbs on one of them and/or there are Sr clusters of one monolayer thickness (or two dimensional islands) on the surface and a free Sr atom adsorbs at the edge of a cluster (step).

The preferential adsorption on the first monolayer rather than on the second, may promote the formation of an ordered Sr 1ML film on the $SrO$ termination. And the low diffusion barrier on the second monolayer may contribute to this process, so that even if a free Sr atom is adsorbed on the second monolayer, it can readily diffuse until reaching a descending step. It is expected that a barrier exists at the descending step, the Ehrlich-Schwoebel barrier, so that diffusing adatoms have a temperature-dependent probability to be reflected there (and consequently clusters may be formed on the second monolayer), nevertheless, the barrier has been observed to be effective at low temperatures [60]; and so it is expected to be small. The Ehrlich-Schwoebel barrier has not been calculated in this work. A sufficiently high growth tem-

perature will thus be necessary so that a diffusing adatom can surmount a descending step to be incorporated in the first monolayer.

It is interesting to note that the calculated adsorption energy, $E_{atom}^{Sr/SrHfO_3}$, also represents the interaction of the adsorbed Sr atom with the substrate surface, and thus can be identified with the binding or desorption energy (with opposite sign). The binding energy of the isolated Sr adatom in the second monolayer to the substrate (a terrace of one monolayer thickness) is then equal to 0.66 eV. When compared to the isolated Sr adatom on the bare surface, this low value not only means a weaker binding to the substrate for the atoms in the second monolayer, moreover, it is equal to the diffusion barrier on the bare surface (Section 3.8.1). Therefore, at sufficiently high temperature to activate diffusion of isolated adatoms on the bare surface, a simultaneous desorption of the isolated adatoms in the second monolayer (formed on top of Sr clusters of one monolayer thickness) will be promoted. Moreover, adatoms in the second monolayer that were not desorbed may still have enough energy to surmount the Ehrlich-Schwoebel barrier at a descending step and become incorporated in the first monolayer. Nevertheless, Sr clusters may still form in the second monolayer, with a higher binding energy than the isolated adatoms, and should be evaporated if they persist on the second monolayer after formation of the first monolayer. In this case, an upper limit for the desorption energy is the atomization energy of the Sr 1ML film, 1.39 eV/Sr.

Therefore, on the $SrO$ termination, in a small energy window between the activation energy for diffusion (0.65 eV) and the binding energy (1.09 eV) of the isolated adatom on the bare surface, formation of the second monolayer may be hindered in favor of formation of the first monolayer. Due to the small energy window, careful handling of the experimental conditions will be necessary. In Figure 3.19, I present a summary of the formation energies $E_{atom}^{Sr/SrHfO_3}$, Eq. (3.3), for the formation process of a Sr 1ML film. Moreover, it is unlikely that an ordered Sr 1/2ML film can be formed in this way on the $SrO$ termination.

## 3.9 Oxidation of the Sr 1ML film

As discussed in the previous sections, the formation of a Sr 1ML film on the $SrO$ termination might be possible under adequate experimental parameters: Sr partial pressure and temperature. The formation of a Sr 1ML film on the $SrHfO_3(001)$ substrate increases the reactivity of the surface, and its

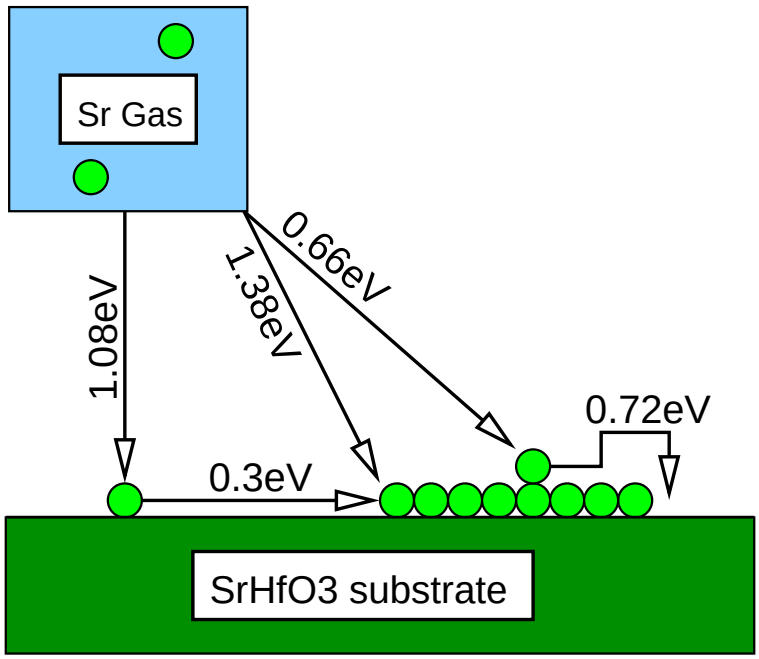


Figure 3.19: Formation energies $E_{atom}^{Sr/SrHfO_3}$, Eq. (3.3), for the formation process of a Sr 1ML film on the $SrO$-terminated $SrHfO_3(001)$ surface. The Sr atoms are green.

impact on the growth mode and growth kinetics of Ge will be discussed in the next sections. This chemically reactive Sr surface can be, in principle, easily oxidized. If oxidation takes place, the resulting surface will be equivalent to the $SrO$ termination of the oxide substrate, where Ge is expected to cluster as discussed in Section 3.5. In this section, I will investigate the feasibility of avoiding oxidation of the Sr 1ML film.

Starting from the assumption that an ordered Sr 1ML film has been formed on the $SrO$ termination, it is important to identify first the possible sources of oxygen during molecular beam epitaxy. They are the atmosphere in the chamber and the oxygen atoms in the $SrHfO_3(001)$ substrate. The former can not be completely suppressed, even in a growth chamber where the only sources are Sr and Ge, residual oxygen remains in small quantity, considered as contamination [61]. On the other hand, oxygen is one of the constituents of the oxide substrate. If the oxygen contamination is not significant, the substrate becomes the only relevant source of oxygen.

In order to determine the feasibility of oxidation of the Sr 1ML film with oxygen from the substrate, I have calculated the thermodynamic stability of a surface configuration where an oxygen atom from the $SrO$ termination has been incorporated in the Sr 1ML film relative to a configuration that

consists of a fully oxidized $SrO$ termination and an unoxidized Sr 1ML film. This process corresponds to the incorporation of an oxygen atom (oxygen 1/4ML) in the Sr 1ML film and the creation of an oxygen vacancy in the $SrO$ termination. The calculated difference in energy is 0.65 eV per oxygen atom. Therefore, oxidation of a fully formed Sr 1ML film by oxygen from the subsurface $SrO$ layer is thermodynamically unfavorable. The relaxed surface configuration with the oxygen atom in the Sr 1ML film is shown in Figure 3.20. The mean distance between the oxygen atom and the nearest Sr atoms in the one monolayer film is 2.39 Å, which is 9 % smaller than the sum of the Sr and oxygen covalent radii (2.64 Å).

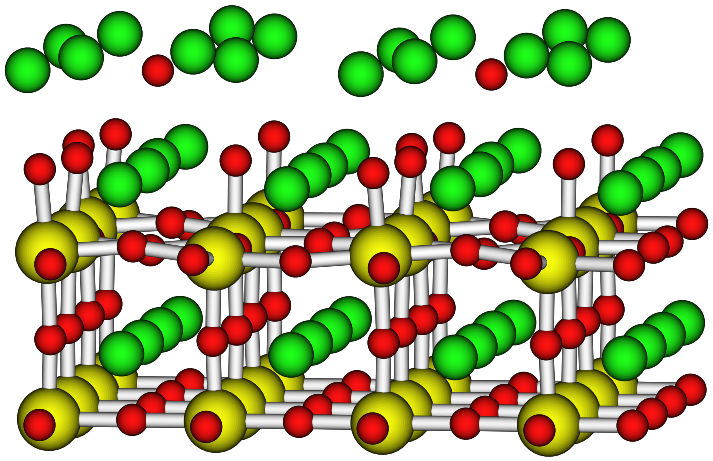

Figure 3.20: Side view of a relaxed structure with one oxygen atom (oxygen 1/4ML) from the subsurface $SrO$ layer, incorporated in the Sr 1ML film. This configuration is thermodynamically unfavorable relative to the fully oxidized $SrO$ layer and unoxidized Sr 1ML film.

Oxidation may occur more efficiently during formation of the Sr 1ML film. The effect of oxidation on the formation process of the Sr 1ML film has not been studied in this work. Nevertheless, if a partially oxidized Sr 1ML

film is formed, an adequate thermal treatment should, in principle, bring the system to its more stable configuration, which it has been shown to consist of the fully oxidized $SrO$-terminated $SrHfO_3(001)$ surface and the unoxidized Sr 1ML film. The applied temperature should then be sufficiently high so that an oxygen atom in the Sr 1ML film can surmount the activation barrier for diffusion back into the subsurface $SrO$ layer, but sufficiently low to prevent atomization of the Sr 1ML film (1.39 eV/Sr).

Therefore, there are indications that an ordered, unoxidized Sr 1ML film can be formed on a flat and perfectly stoichiometric $SrO$-terminated $SrHfO_3(001)$ surface through careful control of the experimental conditions, in a growth chamber with insignificant oxygen contamination. In a small energy window between 0.66 eV (the diffusion barrier of an isolated adatom on the bare oxide surface and also the binding energy of an isolated adatom on the Sr 1ML surface) and 1.09 eV (the binding energy of an isolated adatom on the bare oxide surface), the formation of the Sr 1ML film may be achieved while simultaneoulsy hindering the formation of the second monolayer. Once the Sr 1ML film is formed, deoxidation of the film may be achieved through a thermal treatment with a temperature below the limit of Sr 1ML atomization. The atomization energy of the Sr 1ML film is equal to 1.39 eV/Sr. This energy determines the upper limit for the diffusion and desorption processes involving the Sr 1ML film discussed below. At deposition temperatures below the limit of Sr 1ML atomization, the film can be used as template for Ge overgrowth. Whether the Sr 1ML template determines an interface that modifies the growth mode and growth kinetics of Ge to stabilize the epitaxial Ge surface configuration and/or whether Sr can act as surfactant for Ge layer-by-layer growth is discussed in the following sections. On the other hand, it is unlikely that an ordered Sr 1/2ML template can be formed on the surface for the same purposes.

## 3.10 Substrate termination and surface roughness

Up to this point it has been assumed that a single terrace exists on the $SrHfO_3(001)$ surface, and it is the $SrO$ termination of the substrate. On a real, untreated $SrHfO_3(001)$ surface, two types of surface steps exist, of half and full (cubic) unit cell heights [43]. This indicates the presence of both types of surface terminations, namely, $SrO$ and $HfO_2$, on the substrate surface, where each domain and/or its combination may affect growth

kinetics in a different way. Kawasaki et al. [62] have developed a method for preparation of sufficiently smooth surfaces, terminated by a single atomic layer, and demonstrated it for the model system $SrTiO_3$(001): Since $SrO$ is a basic oxide and $TiO_2$ is an acidic oxide, a pH-controlled wet etch solution may selectively dissolve the $SrO$ layer. A $TiO_2$ terminated surface with a coverage factor of 100 % and steps of full unit cell height has been reported. In principle, the $SrO$ termination can be obtained by layer-by-layer homoepitaxial growth. However, a recent theoretical study of the double-layered $SrTiO_3$(001) surfaces [56], have concluded that the $SrO$ and $TiO_2$ oxide films would grow on the $SrTiO_3$(001) surface preferably through cluster formation rather than in layer-by-layer mode. Moreover, increase of the chemical potential of Sr atoms will lead to precipitation of (bulk) $SrO$ rather than Sr on the $SrTiO_3$ surface, under equilibrium conditions. This suggests that even if a flat $TiO_2$ terminated surface can be fabricated by chemical etching, subsequent deposition of a $SrO$ monolayer (the $SrO$ termination) may not result in a smooth surface. To my knowledge, experimental and theoretical studies of this kind on the $SrHfO_3$(001) surface are lacking. In particular, the formation of $SrO$ clusters on the surface needs to be investigated.

It is interesting to note that on a $SrHfO_3$(001) surface with both types of surface terminations (and steps), the periodicity of a Sr 1ML film will not be maintained across steps of half unit cell height. This is because, in principle, a Sr film adsorbed on the $HfO_2$ termination will be in registry with the subsurface $SrO$ layer of the oxide, whereas a Sr film formed on the $SrO$ termination will not be in registry with this layer. Thus, from a structural point of view, on a surface with only one type of termination, and steps of full unit cell height, the periodicity of the Sr 1ML film can in principle be maintained across the steps.

Formation of the Sr 1ML film under the growth conditions described above may still be affected by the roughness of the $SrHfO_3$(001) surface, which in this case is $SrO$-terminated. In particular, it is not known whether surface steps may promote oxidation of the Sr 1ML film from the substrate. The role of surface steps on the formation of the unoxidized Sr 1ML film remains to be investigated.

## 3.11 Initial Ge deposition on Sr 1ML

As pointed out in the previous section, the Sr 1ML film formed on the $SrO$ termination of the $SrHfO_3$(001) surface increases the reactivity of the surface. When the Sr 1ML film is used as a template for Ge overgrowth,

it may modify the growth mode and the growth kinetics. In this section I will discuss whether these modifications are useful to achieve layer-by-layer growth of Ge on $SrHfO_3(001)$. The simulations presented in the following sections were carried out considering the Sr 1ML film formed on the $SrO$ termination.

### 3.11.1 The isolated Ge adatom

The study of the isolated Ge adatom provides insight into the growth characteristics of the Ge film. Analogous to the previous studies of isolated adsorbates on the $SrHfO_3(001)$ surface presented in this work (Sections 3.5 and 3.8), the isolated Ge atom adsorbed on the Sr 1ML film was simulated by a Ge 1/4ML coverage, which corresponds to the adsorption of one Ge atom per (2x2) surface unit cell. And, in order to determine the adsorption site and the migration mechanism, the potential-energy surface $E_{tot}^{PES}(\vec{R}_{\parallel})$ was calculated for the Sr 1ML formed on the $SrO$ termination.

The most stable adsorption site for an isolated Ge adatom is at the hollow site between four surface Sr atoms of the Sr 1ML film, shown in Figure 3.21(a). The bond length between Ge and a surface Sr atom is 2.98 Å, 5 % smaller than the sum of the Sr and Ge covalent radii (3.13 Å). The Ge atom is adsorbed close to the surface, with a vertical distance to the Sr 1ML plane equal to 0.59 Å (Figure 3.21(b)). The migration path is defined along the shortest path between closest hollow adsorption sites. The barrier configuration is defined along the migration path at the midpoint between two hollow sites (the bridge site), and determines the diffusion barrier. At the diffusion barrier, the bond length is 2.88 Å to the two closest Sr atoms, and it is 8 % smaller than the sum of the Sr and Ge covalent radii. The diffusion barrier is 2.12 eV. This large diffusion barrier indicates that a high deposition temperature will be needed to initiate diffusion in order to achieve the stable Ge configuration on the surface. On the other hand, an isolated Ge adatom on the bare $SrO$-terminated $SrHfO_3(001)$ surface (Section 3.5) adsorbs on top of a surface oxygen atom, which can be associated with the hollow site on the unoxidized Sr 1ML termination, and thus has a similar migration path but a lower diffusion barrier (equal to 0.5 eV).

The formation energy of the Ge epitaxial film on the Sr 1ML-covered $SrHfO_3(001)$ substrate relative to free Ge atoms is defined analogously to Eqs. (3.1) and (3.3), and it is equal to:

$$E_{atom}^{Ge/Sr+SrHfO_3} = \frac{1}{N^{Ge}}\left(E_{slab}^{Ge/Sr+SrHfO_3} - E_{slab}^{Sr+SrHfO_3}\right) - E_{atom}^{Ge}, \qquad (3.5)$$

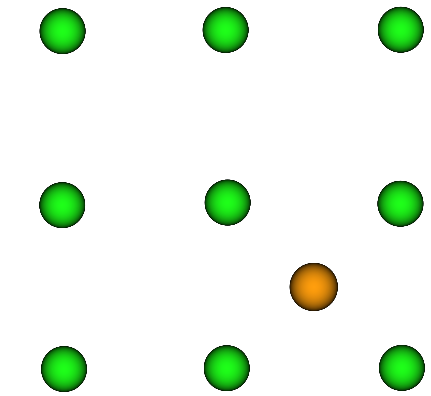

(a)

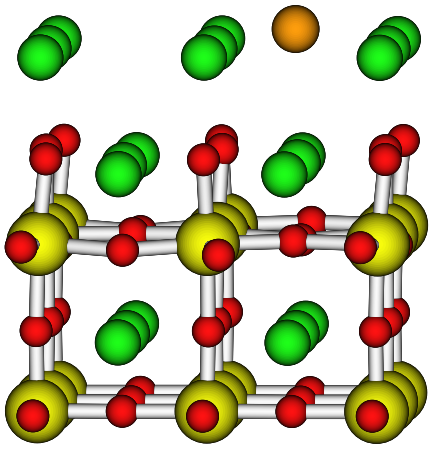

(b)

Figure 3.21: (a) Top view and (b) Side view of an isolated Ge atom adsorbed on the Sr 1ML film formed on the $SrO$-terminated $SrHfO_3(001)$ surface.

where $N^{Ge}$ is the number of Ge atoms within the (2x2) surface unit cell that make up the Ge epitaxial film, $E_{slab}^{Ge/Sr+SrHfO_3}$ is the total energy of the slab containing an adsorbed Ge epitaxial layer, $E_{slab}^{Sr+SrHfO_3}$ is the total energy of the substrate slab which contains the Sr 1ML film formed on the $SrO$-terminated $SrHfO_3$(001), and $E_{atom}^{Ge}$ is the total energy of a free Ge atom (in the gas phase). As mentioned in Section 3.8.1, this energy takes into account the creation of both interfacial and intralayer bonds in the Ge surface configuration when this structure is formed from free Ge atoms, as would occur in molecular beam epitaxy. The adsorption energy of the isolated Ge adatom is obtained from Eq. (3.5) with $N^{Sr} = 1$, and it is equal to -5.59 eV. This large value of the adsorption energy indicates that a free Ge atom that impacts on the surface has a probability to adsorb on it (sticking coefficient) equal to one. Due to the significant interaction of the adsorbed atom with the surface, high temperature will be needed for desorption (higher than that to activate diffusion), which indicates that the Ge epitaxial film has high adhesion to the surface. In contrast, binding of an isolated Ge adatom to the bare $SrO$-terminated $SrHfO_3$(001) surface is weaker, the adsorption energy is equal to -2.5 eV (Section 3.5).

When Ge is adsorbed on the Sr 1ML film, it should passivate its bonds with electrons from the surrounding surface Sr atoms. The $5s$ electrons from Sr saturate the $4p$ half-filled orbitals of Ge. Based on the difference in electronegativies between Sr (0.95 Pauling's) and Ge (2.01 Pauling's), the formation of a covalent bond is expected.

Similar to the definition of $E_{atom}^{Ge/Sr+SrHfO_3}$, Eq. (3.5), the formation energy of the Ge epitaxial film relative to the formation of a bulk Ge structure on the Sr 1ML-covered $SrHfO_3$(001) surface is defined as:

$$E_{clust}^{Ge/Sr+SrHfO_3} = \frac{1}{N^{Ge}}\left(E_{slab}^{Ge/Sr+SrHfO_3} - E_{slab}^{Sr+SrHfO_3}\right) - E_{bulk}^{Ge}, \qquad (3.6)$$

where the notation is the same as in Eq. (3.5), and $E_{bulk}^{Ge}$ is the total energy per atom in bulk Ge (chemical potential). The value of this formation energy for an isolated Ge adatom ($N^{Sr} = 1$) is equal to -1.26 eV. This negative value indicates that Ge (or Ge 1/4ML) wets the substrate and does not cluster. An ordered Ge 1/4ML structure is thus more stable, by 1.26 eV/Ge, than a bulk structure formed on the Sr 1ML-covered $SrHfO_3$(001) surface. In contrast, an isolated Ge adatom (Ge 1/4ML) on the bare $SrO$-terminated $SrHfO_3$(001) surface (Section 3.5) forms clusters, and the value of a similarly defined formation energy, Eq. (3.2), is positive (and equal to 1.8 eV).

Therefore, the Sr 1ML template changes the growth mode of Ge on $SrHfO_3(001)$ to layer-by-layer and, consequently, the epitaxial Ge surface configuration is stabilized. Nevertheless, regarding growth kinetics, a high deposition temperature is needed to achieve the stable epitaxial Ge configuration through diffusion of isolated Ge adatoms on the Sr 1ML surface, due to the large activation barrier for diffusion (2.12 eV). Moreover, before reaching such a high deposition temperature, necessary to initiate Ge diffusion, it is expected that the Sr 1ML film template has already desorbed and divided into free Sr atoms, since its atomization energy is equal to 1.39 eV/Sr (Section 3.8.3). Therefore, Ge diffusion can not be activated if the Sr 1ML template is to be preserved, which may hinder the formation of the stable epitaxial Ge configuration. This issue on the growth kinetics is discussed throughout the following sections.

Since the main difference between the Sr 1ML-terminated and the $SrO$-terminated $SrHfO_3(001)$ surface is the oxygen content of the surface, it is tempting to conclude that wetting of the substrate by Ge is strongly dependent on the passivation of the Ge bonds by the substrate. In the former surface, the electrons from Sr are donated to Ge due to the difference in electronegativities, whereas in the latter surface, the electrons from Sr are donated to oxygen which then makes a bond with Ge.

### 3.11.2 Ge incorporation in the substrate

Note that in Eqs. (3.5) and (3.6) it has been assumed that Ge does not incorporate in the substrate (consisting of the Sr 1ML film formed on the $SrO$-terminated $SrHfO_3(001)$), that means, Ge remains always on top of the Sr 1ML film. I have studied the possibility of Ge (Ge 1/4ML) incorporation through diffusion below the Sr 1ML film to a position between the Sr 1ML film and the $SrO$ termination.

To simulate this surface configuration, a Ge atom adsorbed at the hollow site was vertically shifted to a position below the Sr 1ML plane, and directly on top of a subsurface Sr atom in the $SrO$ oxide layer. Relaxation of this structure with a constraint that forces the Ge adatom to remain below the Sr 1ML film, shows that the Ge avoids bonding to the subsurface Sr atom, and instead bonds to a neighboring oxygen atom, in the $SrO$ termination. As a result, the surface atom in the Sr 1ML film that was originally bonded to oxygen is forced to adopt a higher vertical position above the Sr 1ML plane. A similar behavior of the Ge adatom has been observed in the adsorption on the bare $SrO$ termination (Section 3.5), the stable adsorption site is on top of a surface oxygen atom. A surface configuration with a Ge adatom (Ge 1/4ML) bonded to an oxygen atom in the $SrO$ termination (and below

the Sr 1ML film) is shown in Figure 3.22. This configuration is 1.67 eV/Ge higher in energy relative to the stable configuration with the Ge adatom at the hollow site (on top of the Sr 1ML film). It has been obtained by imposing a constraint that forces the lateral position of Ge and oxygen to be the same, while the Ge height and the coordinates of atoms in the surface layers were allowed to relax. The Ge to oxygen bond length is 2.10 Å, 8 % larger than the sum of the Ge and oxygen covalent radii (1.95 Å), and 11 % larger than the bond length on the bare surface (1.89 Å, Section 3.5). Moreover, after relaxation, the vertical position of Ge is still below the Sr 1ML plane, and the major perturbation on the Sr 1ML film is the raised position of the surface Sr atom that occupied the site on top of oxygen. Finally, when the constraints on the coordinates of the Ge adatom are released, Ge breaks its bond to oxygen and segregates to the surface, to adsorb on top of the Sr 1ML film at the hollow site and form the stable configuration.

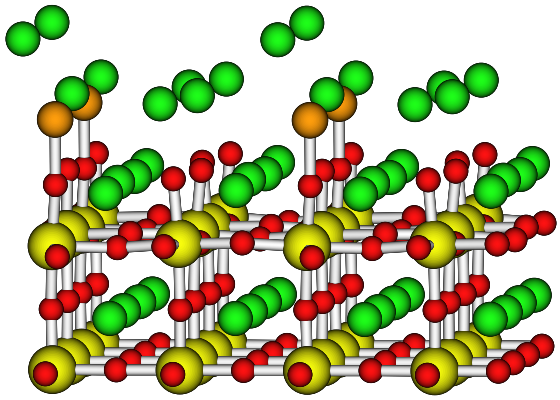

Figure 3.22: Side view of a surface structure with Ge incorporated in the substrate, between the $SrO$ layer of the oxide and the Sr 1ML film. A constraint is imposed on the coordinates of the Ge adatom so that the lateral position of Ge and oxygen are the same.

From a structural point of view, it is interesting to note that the hollow sites of the Sr 1ML film, where Ge adsorbs, are laterally aligned with the Sr atoms in the $SrO$ termination of the oxide, which in turn supports the

Sr 1ML film. When Ge tries to diffuse below the Sr 1ML film through the hollow site, it interacts with a subsurface Sr atom in the $SrO$ termination but avoids making a bond with this atom. Similar interaction between Ge and Sr has also been observed in the Ge adsorption on the bare $SrO$ termination. At the stable configuration, with Ge adsorbed at the hollow site on the Sr 1ML film, the distance to the subsurface Sr atom is 3.21 Å, 3 % larger than the sum of the Sr and Ge covalent radii (3.13 Å), and when the vertical position of Ge is at the Sr 1ML plane the distance is 2.65 Å, 15 % smaller than the sum of the covalent radii. The interaction of the Ge adatom with a subsurface Sr atom in the $SrO$ termination may hinder its diffusion below the Sr 1ML film and incorporation in the substrate.

Therefore, a Ge adatom adsorbed at the hollow site on the Sr 1ML film will not incorporate in the substrate and instead remain on top of the surface. This indicates that the Sr 1ML-covered $SrHfO_3$(001) substrate should be stable during Ge overgrowth (no Ge diffusion in the substrate oxide) at high temperatures which is a requirement for transistor applications. An example of this effect was observed by Seo et al. [42], during Ge growth, $SrHfO_3$ remained stable at high growth temperature (690 °C) whereas $SrHf_xTi_{1-x}O_3$ was unstable and led to Ge diffusion through the oxide, making this gate stack unsuitable for transistors.

### 3.11.3 The Ge 1/2ML surface configuration

At Ge 1/2ML coverage on the Sr 1ML film, there are two Ge adatoms in the (2x2) surface unit cell. The stability of the possible Ge configurations in the (2x2) surface unit cell was investigated. Since the adsorption site of an isolated Ge atom is at the hollow site, it is expected that the stable configuration contains at least one Ge atom adsorbed at a hollow site. Moreover, it is interesting to note that the interfacial layer of an epitaxial Ge film consists of Ge atoms occupying all the available hollow sites on the surface. Apparently, another favorable Ge configuration is the formation of dimers. The stable configuration is obtained by adsorbing one Ge atom at the hollow site and the second atom is adsorbed at any of the non-equivalent hollow sites within the unit cell, including the site already occupied by a Ge atom (this is the Ge dimer configuration). All the surface structures were relaxed without constraints on the coordinates of atoms in the first five surface layers (only the bottom layer was frozen at the bulk configuration).

As expected, the stable configuration consists of Ge atoms adsorbed at hollow sites, shown in Figure 3.23(a). In this configuration, the Ge adatoms

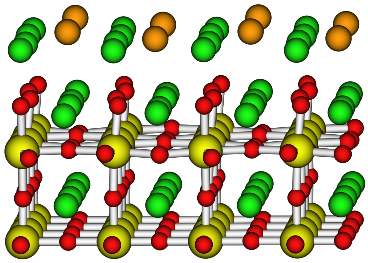

(a)

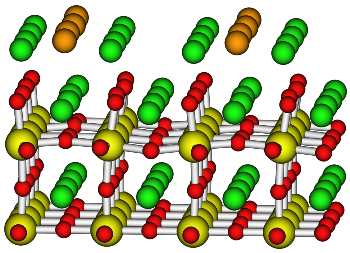

(b)

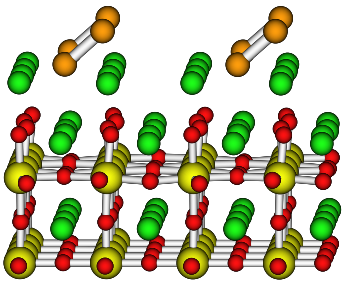

(c)

Figure 3.23: Side view of three Ge 1/2ML surface structures formed on the Sr 1ML film on the *SrO*-terminated oxide surface. (a) Equilibrium structure. (b) Structure almost degenerate with (a). (c) Ge dimer configuration (not stable).

occupy the farthest possible neighbouring hollow adsorption sites. The distance between Ge adatoms is 5.82 Å (half the diagonal length of the cubic surface unit cell), much larger than double the covalent radius of Ge (2.44 Å). The bond length between Ge and a surface Sr atom is equal to 2.99 Å, the same as for the isolated Ge adatom (Section 3.11.1). Another configuration with Ge at hollow sites is almost degenerate with the stable one, higher in energy by 0.05 eV per *adsorbed* Ge (eV/Ge), and it is shown in Figure 3.23(b). The Ge adatoms occupy the closest possible neighbouring hollow adsorption sites, and the distance between Ge atoms is 4.09 Å (half the surface unit cell length). This configuration was also obtained after relaxing a structure with a Ge dimer formed through the bridge site, thus, the dimer bond was broken. Finally, the Ge dimer configuration is shown in Figure 3.23(c), with one Ge adatom at the hollow site and the other at the bridge site, and it was obtained after relaxing a structure with a vertical dimer. In this case the dimer bond was not broken and the dimer length is equal to 2.40 Å, 2 % smaller than double the covalent radius of Ge (2.44 Å). This dimer configuration is 0.58 eV/Ge higher in energy relative to the stable one, and can still be identified as an epitaxial configuration. Since it was obtained after relaxation, starting from a different dimer structure, it can be considered as a metastable configuration (local minimum). Normally, such a configuration should not form on the surface since it is not the stable configuration (global minimum). Nevertheless, as argued above, diffusion of Ge on the surface should not be activated, consequently, the system can not achieve its stable configuration, in this way, due to the suppression of diffusion, metastable configurations (local minima) may form on the surface.

The value of the formation energy $E_{atom}^{Ge/Sr+SrHfO_3}$ of the Ge 1/2ML stable configuration relative to free Ge atoms is obtained from Eq. (3.5) with $N^{Ge} = 2$, and it is equal to -5.16 eV/Ge. It is 0.43 eV/Ge higher than the adsorption energy of the isolated Ge adatom (Ge 1/4ML), indicating that the interaction with the substrate may have been reduced whereas the intralayer interaction may continue to be low due to the large separation between Ge adatoms. Nevertheless, the large value of $E_{atom}^{Ge/Sr+SrHfO_3}$ indicates that the Ge 1/2ML film still has high adhesion to the substrate.

The formation energy $E_{clust}^{Ge/Sr+SrHfO_3}$, Eq. (3.6), of the stable configuration at Ge 1/2ML coverage relative to the bulk Ge configuration on the surface is equal to -0.84 eV/Ge, 0.42 eV/Ge higher than that of the isolated Ge adatom so the stability is decreased. The negative value indicates that Ge wets the substrate, and so the Ge 1/2ML film configuration is more stable than the bulk configuration.

Therefore, at Ge 1/2ML coverage on the Sr 1ML-covered $SrHfO_3(001)$ surface, the stable configuration is epitaxial and consists of Ge atoms adsorbed at hollow sites. Nevertheless, metastable configurations may form on the surface due to the suppression of diffusion.

### 3.11.4 The Ge 3/4ML surface configuration

Increasing the Ge coverage does not necessarily result in a surface structure with increased occupation of hollow sites. I have studied the equilibrium configuration of a Ge 3/4ML film on the Sr 1ML template, and found that the stable configuration consists of a short chain. This short chain structure is epitaxial and is an structural element of the Ge(001) 2ML film.

In order to simulate the Ge 3/4ML coverage, three Ge atoms where considered within the (2x2) surface unit cell. The equilibrium configuration is shown in Figure 3.24(a). It is a short chain with two Ge atoms in adjacent hollow sites and the third atom at the bridge site. The bond length of the two bonds is 2.55 Å, 4.5 % larger than twice the covalent radius of Ge (2.44 Å). A second Ge surface configuration is shown in Figure 3.24(b), it is 0.11 eV/Ge higher in energy relative to (almost degenerate with) the equilibrium one. This structure consists of a Ge dimer perpendicular to the surface formed at the hollow site, and a third Ge atom at an opposite hollow site, so that it is not possible to achieve the short chain equilibrium configuration. A third configuration with the three Ge atoms in the (2x2) surface unit cell occupying the hollow sites (Figure 3.24(c)) is also almost degenerate with the equilibrium configuration, 0.12 eV/Ge higher in energy.

The short chain equilibrium configuration has a formation energy relative to free Ge atoms, $E_{atom}^{Ge/Sr+SrHfO_3}$, equal to -4.89 eV/Ge, obtained from Eq. (3.5) with $N^{Ge} = 3$. Compared to the same value for the Ge 1/2ML, it is 0.27 eV/Ge higher in energy, indicating a decrease in the interaction with the substrate. Nevertheless, this structure is strongly bound to the substrate.

The formation energy $E_{clust}^{Ge/Sr+SrHfO_3}$, Eq. (3.6), of the short chain configuration relative to the bulk Ge configuration on the surface is equal to -0.57 eV/Ge. Ge wets the substrate and formation of a short chain is thermodynamically favorable over formation of the Ge bulk configuration on the surface.

It is interesting to note that the short chain equilibrium configuration is an epitaxial one. As can be seen in Figure 3.13(b), the Ge(001) surface structure is made out of parallel infinite chains joined by (buckled) dimers. These parallel infinite chains also constitute the bulk structure. Thus the

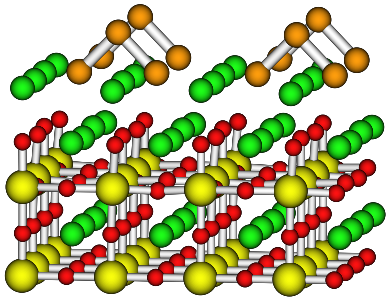

(a)

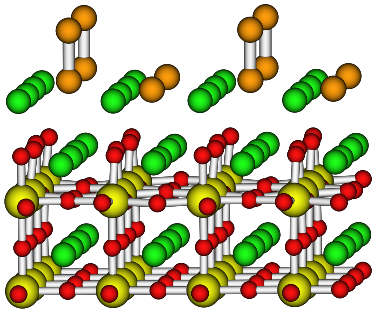

(b)

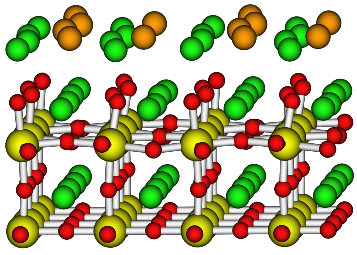

(c)

Figure 3.24: Side view of three almost degenerate Ge 3/4ML surface structures formed on the Sr 1ML film on the $SrO$-terminated oxide surface. (a) Short chain (equilibrium structure). (b) Ge dimer and Ge at hollow site. (c) Occupation of the hollow sites.

short chain is a structural element of the Ge(001) and bulk Ge structures. If the short chains are able to grow and coalesce then an epitaxial Ge 2ML film will be formed on the surface. In fact, a Ge(001) 2ML film is made out of parallel (infinite) chains joined by dimers on the first and second monolayers (both surfaces). Moreover, the structure with Ge adatoms at hollow sites can be considered epitaxial, since these are the sites that the interfacial atoms of the Ge(001) film will ideally occupy. On the other hand, the structure with a Ge dimer is not clearly epitaxial but can originate an epitaxial configuration when the Ge coverage increases. At low temperatures, any of the above mentioned Ge 3/4ML structures can be formed locally on the surface and coexist with other structures. At this coverage, the migration mechanism of Ge on the surface may be affected (locally) by the significant presence of Ge structures on the surface.

The formation of the short chain structure indicates that the initial stages of Ge growth may not be layer-by-layer. Ge layer-by-layer growth would correspond, in this case, to the occupation of all the available hollow sites on the Sr 1ML template to form the first monolayer; at 3/4ML, the structure with Ge adatoms at hollow sites has been shown, however, to be almost degenerate with the short chain structure. In the short chain structure, the Ge atom at the bridge site belongs to the second monolayer. Thus, during the initial stages of Ge growth, there seems to be a tendency to form a Ge(001) 2ML film directly via the growth and coalescence of chains; for coverages higher than 2ML, normal layer-by-layer growth is expected to occur. There is, however, no preferred growth direction for the Ge chains, so chains with perpendicular directions may in principle be formed on a surface terrace. In the following sections it will be shown that during the initial stages of Ge growth and at coverages higher than 3/4ML, Ge forms a compound with Sr that seems to stabilize the Ge epitaxial growth. The formation of such a compound may also promote the local growth of chains in only one direction.

### 3.11.5 The Ge 1ML surface configuration

At Ge 1ML coverage on the Sr 1ML film, I have found several almost degenerate structures consisting of short chains, adatoms occupying hollow sites, long (infinite) chains and diagonal-rows of dimers, shown in Figures 3.25 and 3.26. At this coverage, the size of the (2x2) unit cell influences the obtained geometries. Nevertheless, it can be seen that there is a tendency to form chains and dimers. Moreover, in the lower energy structures, Figures 3.25 and 3.26(a), a Sr atom from the Sr 1ML template has segregated to the forming Ge surface, as can be seen in Figure 3.25(a); this corresponds

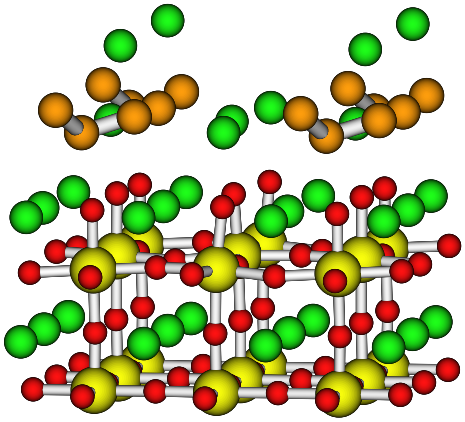

(a)

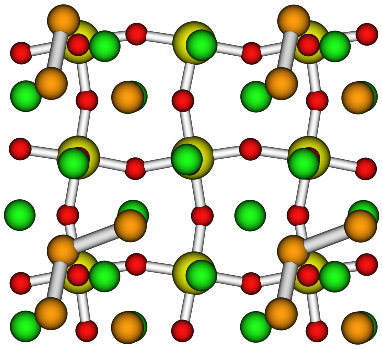

(b)

Figure 3.25: Most stable Ge 1ML structure, with diffusion of Sr from the Sr 1ML film to the surface: (a) side view, and (b) top view.

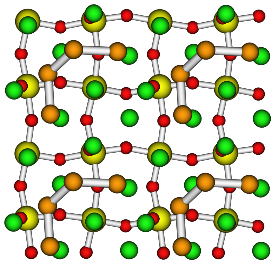

(a) $\Delta E = 0.10$ eV/Ge

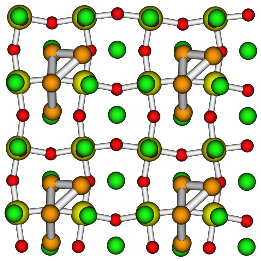

(b) $\Delta E = 0.17$ eV/Ge

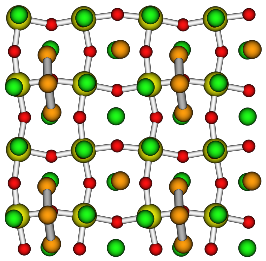

(c) $\Delta E = 0.17$ eV/Ge

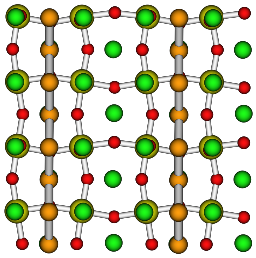

(d) $\Delta E = 0.17$ eV/Ge

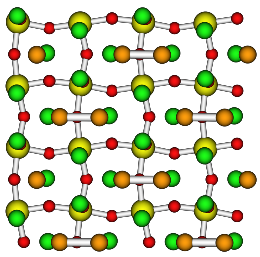

(e) $\Delta E = 0.27$ eV/Ge

Figure 3.26: Top view of relaxed Ge 1ML surface structures formed on the Sr 1ML film on the *SrO*-terminated oxide. They are less stable than the structure in Figure 3.25, as indicated by their relative energies (per Ge atom) to this structure. Only in (a) there is Sr diffusion from the Sr 1ML film to the surface. (b) Short chain and dimer, (c) short chain and hollow site, (d) infinite chain, (e) diagonal-rows of dimers.

to the diffusion of Sr 1/4ML from the interface (reduced to Sr 3/4ML) to the Ge surface. The segregation of Sr atoms to the surface is an indication that a Sr-Ge compound is being formed. The many different surface structures shown in Figures 3.25 and 3.26 may coexist on the surface during growth, due to the small energy difference between them, which is also an indication that a transition to a new structure or compound on the surface is taking place. Thus, at this coverage, regions with and without segregated interfacial Sr atoms may coexist on the surface.

The value of $E_{clust}^{Ge/Sr+SrHfO_3}$, from Eq. (3.6), (and $E_{atom}^{Ge/Sr+SrHfO_3}$, from Eq. (3.5)) can not be obtained for the structure in Figure 3.25 due to the fact that the substrate no longer consits of a Sr 1ML film and a $SrO$-terminated oxide. Nevertheless, for the structure in Figure 3.26(b), the value of $E_{atom}^{Ge/Sr+SrHfO_3}$ is equal to -4.75 eV/Ge, and $E_{clust}^{Ge/Sr+SrHfO_3}$ is equal to $-0.43$ eV/Ge. These values are 0.14 eV/Ge higher than the corresponding values for the Ge 3/4ML, and maintain the same tendency, namely, a high adhesion of the Ge film to the substrate and Ge wetting of the substrate.

I have also found that a surface configuration with a Ge 1ML film buried below the Sr 1ML film template (i.e. between the Sr 1ML film and the $SrO$-terminated oxide) is not thermodynamically stable. This structure is shown in Figure 3.27. It is 0.91 eV/Ge higher in energy than the structure in Figure 3.25. This is also an indication that the tendency is to segregate only part of the interfacial Sr atoms and not the complete 1ML film.

Therefore, at Ge 1ML coverage, there is the tendency to form a Sr-Ge compound and also to form chains and dimers on the surface. Due to the small energy difference between the obtained surface structures, regions with and without segregated interfacial Sr atoms may coexist on the surface. The influence of the segregated Sr atoms on the stabilization of the Ge epitaxial film will be discussed in the following sections.

## 3.12 Stability of Ge epitaxial layers on Sr 1ML

In order to understand the behaviour of the Sr 1ML template during Ge epitaxial growth, I have studied the stability of several surface configurations containing epitaxial Ge 2ML and 3ML films. In particular, the role of the Sr 1ML template for the stabilization of the Ge epitaxial structure was investigated. It has been found that the Sr 1ML film at the interface does not remain complete during Ge growth, and partly segregates to the Ge surface. Sr 1/2ML remains at the interface and the other half diffuses to the Ge surface. Ashman et al. [54] have shown that a Sr 1/2ML film passivates

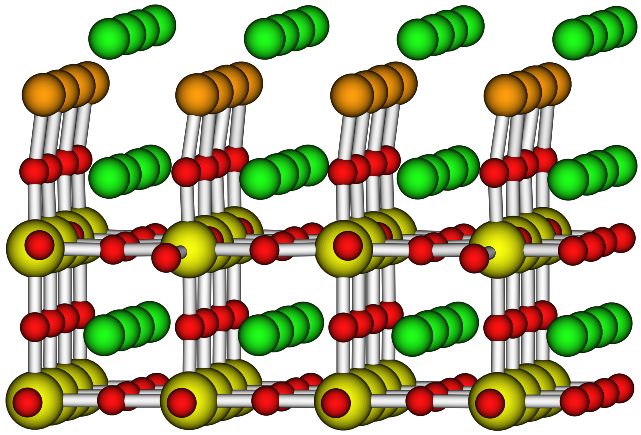

Figure 3.27: Side view of a surface structure with a Ge 1ML film adsorbed between the Sr 1ML template and the *SrO*-terminated oxide. It is 0.91 eV/Ge higher in energy than the structure in Figure 3.25.

all the dangling bonds of the Si(001) surface and that this surface structure has no states in the band gap. The same is observed for the Ge(001) surface. A Ge(001) thin film with Sr 1/2ML on both surfaces is thus a passivated surface structure. This passivated structure is expected to be more stable than other unpassivated surface configurations, e.g. a Ge thin film with a free surface made out of unsaturated dangling bonds and with a Sr 1ML film adsorbed on the other surface of the thin film.

In the following, I argue that Sr 1/2ML at the interface and surface promotes stabilization of the Ge epitaxial structure. Additionally, Sr 1/2ML at the Ge surface can act as surfactant for heteroepitaxial layer-by-layer growth. Therefore, it seems that the Sr 1ML film performs different tasks during Ge deposition on the $SrO$-terminated $SrHfO_3$(001) surface, finally leading to heteroepitaxial surfactant-mediated layer-by-layer growth.

### 3.12.1 The Ge 2ML surface configuration

At Ge 2ML coverage I have found that a structure with Sr 1/2ML passivating both surfaces of the epitaxial film (Figure 3.28(a)) is slightly more stable than another with Sr 1ML at the interface (Figure 3.28(b)). It is important to note that both surface structures are epitaxial Ge(001) 2ML films, and the main difference between them is the passivation of both surfaces of the thin film. The former surface structure is 0.06 eV/Sr lower in energy than the latter. Since this value is too small, it is not possible to conclude whether Sr 1/2ML has completely diffused to the surface at Ge 2ML coverage. Thus, it is likely that both surface structures coexist on the surface. For the structure in Figure 3.28(b), the value of $E_{atom}^{Ge/Sr+SrHfO_3}$, from Eq. (3.5), is -4.56 eV/Ge and $E_{clust}^{Ge/Sr+SrHfO_3}$, from Eq. (3.6), is -0.24 eV/Ge. The high adhesion of the Ge film to the substrate and Ge wetting of the substrate is maintained.

Moreover, I have found another structure slightly lower in energy that resembles a closed chain (i.e. a ring). This chain structure is shown in Figure 3.29 and is 0.06 eV/Ge lower in energy than the structure in Figure 3.28(a). The energy difference is too small to conclude whether an epitaxial Ge 2ML film with Sr 1/2ML passivated surfaces does form. Additionally, the small size of the (2x2) surface unit cell influences the obtained geometries. Nevertheless, from Figures 3.28 and 3.29, it is clear that the Ge atoms have the tendency to form chains and dimers on the surface while, simultaneously, Sr 1/2ML segregates to the surface (but not yet completely). The formation of this Sr-Ge compound leads to the Ge epitaxial film, as will be shown in the next section.

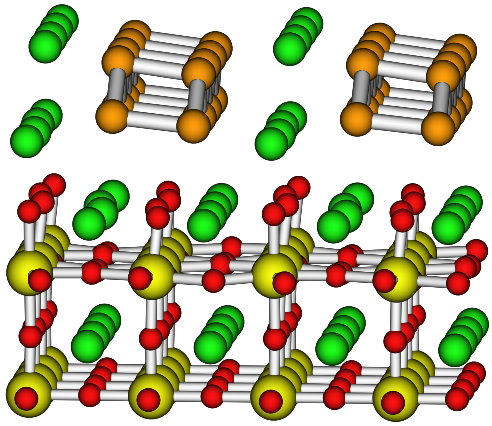

(a)

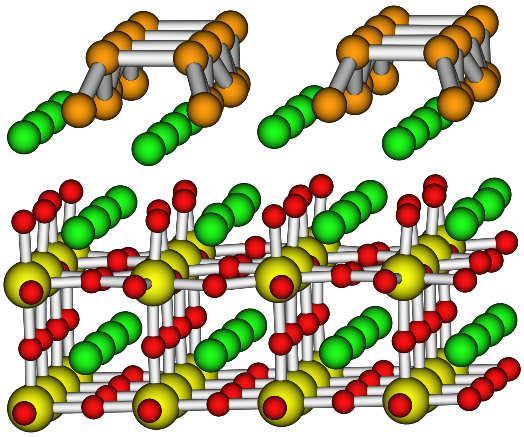

(b)

Figure 3.28: Side view of two almost degenerate epitaxial Ge 2ML surface structures formed on the Sr 1ML film on the *SrO*-terminated oxide surface. (a) Epitaxial Ge 2ML film with Sr 1/2ML-passivated surfaces, after Sr 1/2ML diffusion to the surface. (b) Epitaxial Ge 2ML film formed on the Sr 1ML template (no Sr segregation).

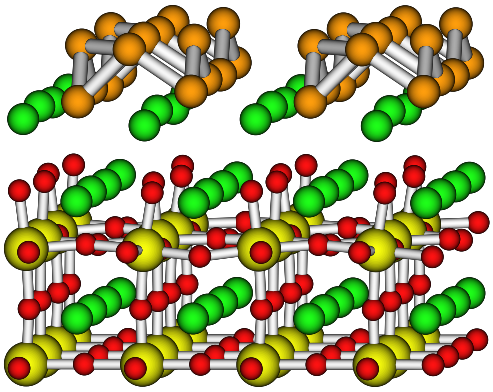

(a)

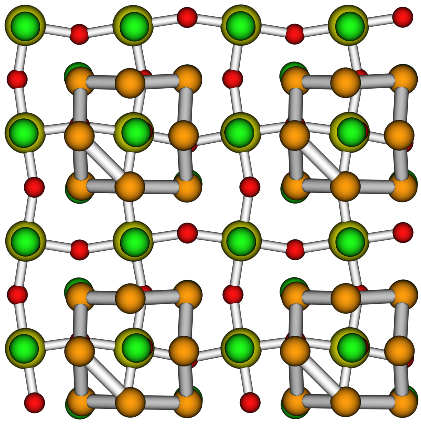

(b)

Figure 3.29: Most stable Ge 2ML structure formed on the Sr 1ML template, with Ge chains arranged in a ring shape and without Sr segregation to the surface: (a) side view, and (b) top view. This surface structure is almost degenerate with the structure in Figure 3.28(a).

### 3.12.2 The Ge 3ML surface configuration

At Ge 3ML coverage, the difference in energy between surface structures containing an epitaxial Ge film with and without Sr 1/2ML passivation is more apparent. A passivated configuration (Figure 3.30(a)) is 0.30 eV/Sr more stable than an unpassivated configuration (Figure 3.30(b)). This result indicates that at Ge coverages higher than 2ML, the Sr 1/2ML passivated Ge(001) film may be stabilized. In this way, the Sr 1ML template promotes the formation of the Ge epitaxial structure on the oxide surface.

For the structure in Figure 3.30(b), the value of $E_{atom}^{Ge/Sr+SrHfO_3}$, from Eq. (3.5), is -4.53 eV/Ge and $E_{clust}^{Ge/Sr+SrHfO_3}$, from Eq. (3.6), is -0.21 eV/Ge. As for lower Ge coverages, the high adhesion of the epitaxial film to the substrate and Ge wetting of the substrate is maintained.

It is interesting to note that once a continuous Ge film is formed on the surface, the large atomic radius of Sr (2.45 Å) may hinder diffusion from the interface to the surface. Thus, Sr segregation should be promoted to occur (e.g. thermal treatment) at an adequate stage of Ge growth, between 1ML and 2ML in order to minimize the possibility of desorption of the Sr 1ML template.

Therefore, it has been shown that the Sr 1ML template has the tendency to segregate to the Ge surface in order to passivate it. The Ge epitaxial structure with both surfaces of the thin film passivated by Sr 1/2ML has been found to be stable for coverages higher than 2ML. Although the Sr tendency to segregate increases with Ge coverage, the large atomic radius of Sr may hinder its segregation to the surface with increasing Ge coverage. A thermal treatment at a suitable stage of growth may in principle be used to promote Sr segregation and stabilization of the Ge epitaxial structure.

## 3.13 Mechanism for Ge growth on a Sr-covered oxide surface

The presented results indicate that even though Ge wets the Sr 1ML surface, the initial formation of the Ge epitaxial film may not occur layer-by-layer but rather via the formation of a Sr-Ge compound. This compound is formed when the Sr atoms in the Sr 1ML template start diffusing to the Ge surface and remain there. It has been shown that a passivated Ge epitaxial film is more stable than an unpassivated one, however, this difference seems to be more apparent for coverages higher than 2ML.

The Zintl-Klemm concept [63] can be used to gain insight into the formation process of the intermediate compound. It states that an element with

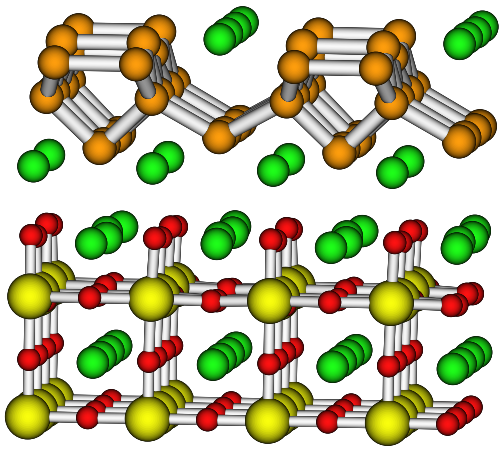

(a)

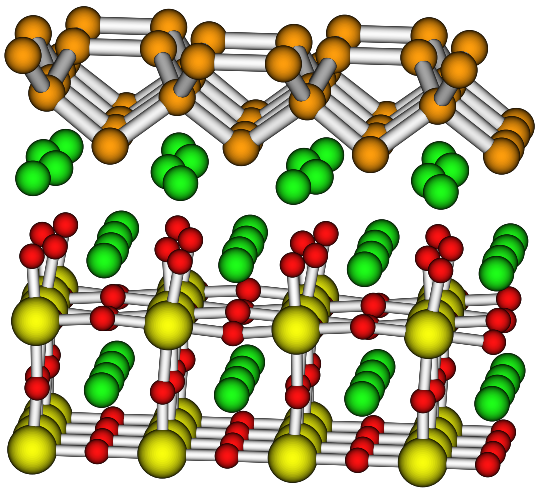

(b)

Figure 3.30: Side view of two epitaxial Ge 3ML surface structures formed on the Sr 1ML film on the *SrO*-terminated oxide surface. (a) Epitaxial Ge 3ML film with Sr 1/2ML-passivated surfaces, after Sr 1/2ML diffusion to the surface (equilibrium configuration). (b) Epitaxial Ge 3ML film formed on the Sr 1ML template (not stable).

an increased number of electrons forms structures that are similar to those formed by elements with the corresponding increase in the atomic number. For example, in $SrGe_2$ the Ge atoms have a structure similar to that of phosphorous and in $SrGe$, the Ge structures are chains, similar to that of sulfur. This type of structures can be identified in many of the stable Ge surface structures presented above, most importantly, the Ge chain structure found at 3/4ML and 1ML coverage. Nevertheless, as pointed out above, it is possible that many of these structures coexist on the surface.

After the formation of the passivated epitaxial Ge film, what is the role of Sr? Sr 1/2ML at the interface stabilizes the Ge epitaxial film and passivates the dangling bonds to unpin the Fermi level, analogously to the $SrTiO_3/Si(001)$ interface [52], discussed in Section 3.7.4. Sr 1/2ML at the Ge(001) surface should passivate the dangling bonds but also may act as a surfactant since it lowers the surface energy of Ge(001). Moreover, due to the large atomic radius of Sr (2.45 Å) it is expected that it does not incorporate in bulk Ge during growth. In this case, a surfactant should improve the efficiency of Ge growth, since Ge already wets the $SrHfO_3(001)$ surface.

## 3.14 The Sr-interfaces of $SrHfO_3/Ge(001)$

The Sr 1/2ML oxidized and unoxidized interfaces of $SrHfO_3/Ge(001)$ have been studied. A first estimate of the valence band offset was obtained through a thick slab consisting of five layers of the oxide and five layers of the semiconductor, plus the interface. Bulk Ge and bulk $SrHfO_3$ were calculated separately with the same accuracy and parameters used in the slab calculations. The layer projected density of states of the bulk materials was aligned to the corresponding bulk layers in the slab. Low energy atomic states in bulk Ge and bulk $SrHfO_3$ were aligned to the same states in the bulk layers of the slab. In the case of Ge the slab bulk layer is the frozen back plane layer and for $SrHfO_3$, it is the uppermost (farthest from the interface) layer. For transistor applications, the potential barrier at each band (the band offset) must be over 1 eV in order to inhibit conduction by the emission of electrons or holes from the semiconductor into the oxide conduction and valence bands, respectively.

For the oxidized Sr 1/2ML interface (Figure 3.31(a)) I found that the hole injection barrier or valence band offset is too small (0.45 eV) for transistor applications since this value should be larger than 1 eV. This result is in contrast with the $SrTiO_3/Si(001)$ interface [52] where the oxidized interface provided adequate band offsets. On the other hand, the unoxidized interface has a valence band offset of 1.68 eV, and a corresponding conduction band

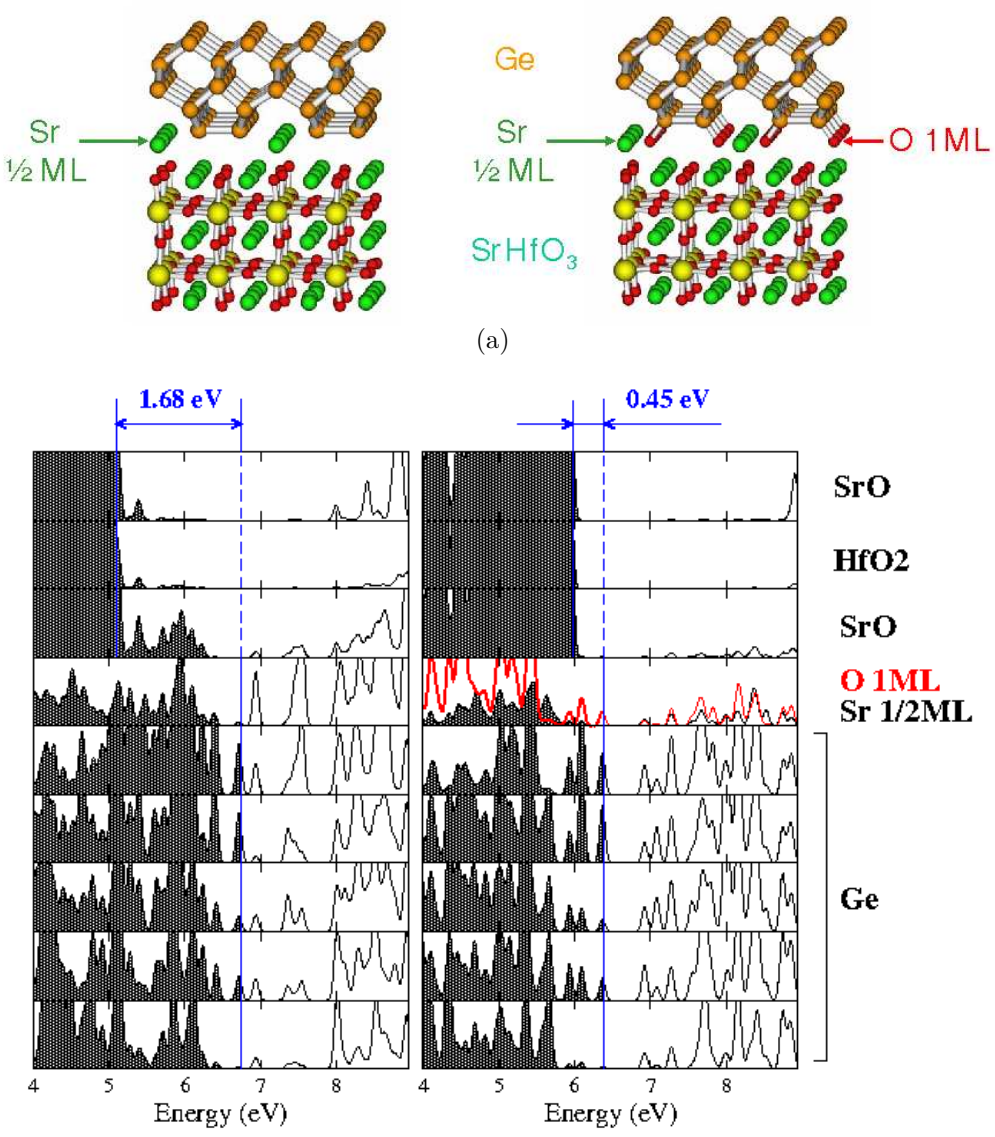


Figure 3.31: Top: Atomic structure of the Sr 1/2ML unoxidized (left) and oxidized (right) $SrTiO_3/Si(001)$ interfaces. Bottom: Layer projected density of states and valence band offsets of the Sr 1/2ML unoxidized (left) and oxidized (right) $SrTiO_3/Si(001)$ interfaces.

offset of 4.06 eV (taking into account the experimental band gap of $SrHfO_3$, 6.5 eV [35], and Ge, 0.76 eV [38]) which are suitable for transistor applications (Figure 3.31(b)). The Sr 1/2ML interface can be identified with part of the Sr 1ML template that remained at the interface after Ge overgrowth.

## 3.15 Summary

In this chapter, the feasibility of using Sr for heteroepitaxial growth of Ge on the $SrHfO_3(001)$ surface has been investigated. It has been confirmed that Ge does not wet the oxide and therefore clusters. It has been found that Sb may not be a suitable surfactant to initiate Ge growth on the oxide. On the other hand, Sr is an interesting candidate for this task. There are indications that an ordered Sr 1ML film can be formed on the oxide surface to be used as template for Ge overgrowth. This film passivates the Ge adatoms and promotes Ge wetting of the surface, however, diffusion is hindered on this template which may induce the formation of Ge metastable structures. At high Ge coverages, it is found that Ge forms epitaxial structures and that Sr diffuses from the interface to the surface. It is likely that between coverages of 1ML and 2ML a Sr-Ge compound is formed that will originate the Ge epitaxial film since there are indications that this film is not formed in a layer-by-layer fashion at the initial stages of growth. At Ge coverages higher than 2ML the stabilization of the Ge epitaxial film is more apparent and a stable configuration should consist of Sr 1/2ML at the interface and at the Ge surface. Sr 1/2ML at the interface stabilizes the Ge epitaxial structure, unpins the Fermi level by passivating the Ge dangling bonds and provides suitable band offsets for transistor applications. On the other hand, Sr 1/2ML at the Ge surface may act as surfactant to improve the efficiency of Ge growth, since Ge already wets the surface.

# Chapter 4

# The $La_2Hf_2O_7/Si(001)$ interface

## 4.1 Introduction

Lanthanum hafniate ($La_2Hf_2O_7$) is a complex oxide that has promising electrical and structural characteristics for transistor applications and integration with silicon (Si). It has a measured dielectric constant between 18 and 23, a large band gap (4.25 eV) and large conduction and valence band offsets [64]. Moreover, growth of ($La_2Hf_2O_7$) on Si has been demonstrated by molecular beam epitaxy [65].

The $La_2Hf_2O_7/Si(001)$ interfacial structure is not known and it is studied theoretically in this work. The influence of the interfacial structure on the band alignment is still debated due to experimental data indicating that the band offsets of some systems are independent of the amorphous or crystalline nature of the oxide [66].

## 4.2 Computational Details

Total energy calculations of the $La_2Hf_2O_7/Si(001)$ interfaces were performed using the Projector Augmented Wave (PAW) method [22] (Section 2.4), based on density-functional theory [12] (Section 2.2), with the generalized gradient approximation (GGA) for the exchange-correlation potential as implemented by Perdew, Burke and Ernzerhof (PBE) [36]. The valence wave functions were expanded in plane waves with a *cut-off* energy of 30 Ry outside the augmentation region, and inside, in partial waves. The following valence electrons were considered: $2s^2 2p^4$ for oxygen, $3s^2 3p^2$ for silicon (Si), $5s^2 5p^6 6s^2 5d^1$ for lanthanum (La), and $5s^2 5p^6 6s^2 5d^2$ for hafnium (Hf). And the following sets of *projector* functions per angular momentum $(s, p, d, f)$ were used: $(2, 2, 1, 0)$ for oxygen, $(2, 2, 1, 0)$ for Si, $(2, 2, 1, 2)$ for La, and

$(2, 2, 2)$ for Hf. The semi-core states of La and Hf were treated as valence states. The frozen core approximation was used (Section 2.4.3).

The $La_2Hf_2O_7$ oxide can grow amorphous or crystalline on the Si(001) substrate depending on the growth temperature. The crystalline oxide is structurally compatible with Si, and cube-on-cube epitaxy is possible. The crystalline interfaces have been constructed by matching tetragonal $La_2Hf_2O_7$ (LHO) to Si(001), with an alignment of $(001)_{LHO} \parallel (001)_{Si}$ and $[110]_{LHO} \parallel [110]_{Si}$ orientations. The lattice constant of the oxide is double that of Si (5.431 Å [38]), and the lattice mismatch is -0.74 % at room temperature (the oxide is slightly strained). The experimental lattice parameter of bulk Si was used. A grid with four k-points per (2x2)Si(001) surface unit cell was used to sample the Brillouin zone. The experimental band gap of bulk $La_2Hf_2O_7$ is 4.25 eV [64], and that of bulk Si is 0.786 eV [38]. The typical underestimation of the band gap by density-functional theory was not corrected in this work.

For the slab calculations, five layers of Si and five layers of the oxide were used to determine the interfacial structure. The back plane of the semiconductor and the passivating hydrogen layer were kept frozen, while all other atomic coordinates were relaxed without symmetry constraints (except for time-inversion symmetry). The vacuum separating adjacent slab images in the direction perpendicular to the surface was never below 8 Å.

Sandwich calculations were performed to determine the band offsets of the interfaces. The initial interfacial configuration was obtained from the slab calculations. The sandwiches consisted of twelve Si layers and eleven $La_2Hf_2O_7$ layers, including the interfacial layers. The eight innermost layers of Si, and the five innermost layers of $La_2Hf_2O_7$ were kept frozen in the bulk configuration. These frozen layers are considered the bulk layers of the sandwich. All other atomic coordinates were allowed to relax without symmetry constraints. The constructed sandwich has inversion symmetry and there is no vacuum separating the repeated images in the direction perpendicular to the interface.

The plane wave part of the potential in the sandwich was averaged in planes parallel to the interface, and similarly for the bulk Si and $La_2Hf_2O_7$ calculations. The averaged potential in the bulk layers of the sandwich is expected to be similar to that of the corresponding bulk material. When the bulk potential of each material in the heterojunction is aligned with the corresponding potential in the bulk layers of the sandwich, a better estimate of the valence band top should be obtained. By comparing the position of the valence band top for both materials, the valence band offset for the interface is obtained. In this way, the valence band maxima at the interface can be related by comparing the averaged bulk potentials (calculated separately) to

the bulk part of the sandwich potential [67]. This approach is analogous to the experimental determination from x-ray photoelectron spectroscopy [68]. The alignment of the averaged bulk potentials can be identified with the alignment of the core level positions used in the experimental analysis.

## 4.3 The $La_3HfO_5$ class of interfaces

The number of possible interface structures can be reduced if only interfaces that are electronically saturated, and that therefore do not pin the Fermi level, are considered. The structure of bulk $La_2Hf_2O_7$ in the [001] direction consists of alternating layers with $La_2Hf_2$ and $O_7$ stoichiometry. The metal layer can in principle provide, formally, fourteen electrons per (2x2) surface unit cell which half saturate the oxygen atoms above and below this metal layer. When $La_2Hf_2O_7$ forms an interface with Si(001), it is possible that the oxygen atoms from the oxide face the Si substrate and passivate it. A reconstructed Si(001) surface, with two dimers per (2x2) surface unit cell can provide four electrons to saturate the oxygen atoms in the oxide, instead of seven as in bulk $La_2Hf_2O_7$. Consequently, the metal layer directly above the interfacial oxygen atoms should provide an uneven number of electrons per (2x2) surface unit cell; seven of these electrons will half passivate the seven oxygen atoms above the metal layer, and the rest should passivate the interfacial oxygen atoms below the metal layer together with the four electrons from the Si substrate. In order to have an oxide with a metal layer without atomic vacancies, the possible interfaces are $La_3HfO_5$ and $LaHf_3O_6$. In the former, the $La_3Hf$ metal layer provides thirteen electrons per (2x2) surface unit cell, seven are used to passivate the oxygen layer above, and the other six electrons together with the four electrons from the Si substrate are used to passivate the five interfacial oxygen atoms. Similarly, in the $LaHf_3O_6$ interface the metal layer provides fifteen electrons per (2x2) surface unit cell, and eight of those electrons plus four from Si passivate six interfacial oxygen atoms.

In this way, electron count arguments determine the possible stoichiometries of the interface without Fermi level pinning as $La_{(2+x)}Hf_{(2-x)}O_{(5.5-0.5x)}$. This implies that, compared to the bulk, the interfacial layer is oxygen deficient. It also indicates that deviations from the La/Hf stoichiometry are necessary for electronically inactive interfaces. One class of interfaces was investigated, namely the one with x=1 ($La_3HfO_5$) and lower oxygen concentration at the interface.

In the $La_3HfO_5$ configuration, four oxygens in the same plane oxidize the four Si atoms arranged in two dimers in the (2x2)Si(001) surface, and

the initial position of the oxide's fifth oxygen is between the $La_3Hf$ metal layer and the $O_4$ layer which oxidize the Si surface . The structural difference between the calculated interfacial structures lies in the Si dimer rows' orientation relative to the oxide, and the position of the oxide's fifth oxygen at the interface. The most stable interfacial configuration (Interface A) is shown at the top of Figure 4.1, where the oxide's fifth oxygen atom has relaxed towards the oxide bulk. This relaxation is large, 1.88 Å, and creates a dipole perpendicular to the interface. In the second structure (Interface B), shown at the middle of Figure 4.1, the Si dimer rows' orientation relative to the oxide is perpendicular to the Interface A, and the oxide's fifth oxygen atom remains close to its initial position. This interfacial structure is only 0.013 eV per 1x1 unit cell of Si(001) higher in energy than the most stable one. We also show at the bottom of Figure 4.1 an interfacial structure (Interface C) with the same Si dimer rows' orientation as in Interface B but with the large oxygen relaxation towards the oxide bulk, this structure is almost degenerate with the most stable one (0.005 eV higher in energy). These small total energy differences are within our error bars. The fact that interfaces A and C are energetically degenerate, suggests that there is no preferred $[110]_{Si}$ orientation of the Si(001) substrate for epitaxial growth of LHO.

From the calculated interfacial structures, sandwichs were constructed in order to determine the valence band offsets of these crystalline interfacial structures. The calculated valence band offset of interface A is equal to $1.81 \pm 0.27$ (the uncertainty corresponds to the fitting procedure), and it is shown in Figure 4.2(a). When the experimental band gaps of bulk $La_2Hf_2O_7$ and Si are taken into account, the conduction band offset can be estimated to be equal to 1.65 eV. On the other hand, for interface B the calculated valence band offset is equal to $2.37 \pm 0.02$ eV (the uncertainty again corresponds to the fitting procedure), and it is shown in Figure 4.2(b). The large difference in band offset is due to the different position of the fifth oxygen atom. Its relaxation induces an electric dipole responsible for the change in the band offsets. On the other hand, similar band offsets for interfaces A and C are expected.

## 4.4 Summary

The atomic structure and the valence band offsets of the crystalline $La_2Hf_2O_7/Si(001)$ interface were studied. The $La_3HfO_5$ class of interfaces unpins the Fermi level which is a requirement for transistor applications. Three interfacial structures of this class were studied and found to be degenerate. These interfacial structures consist of a dimerized (2x2)Si(001) surface

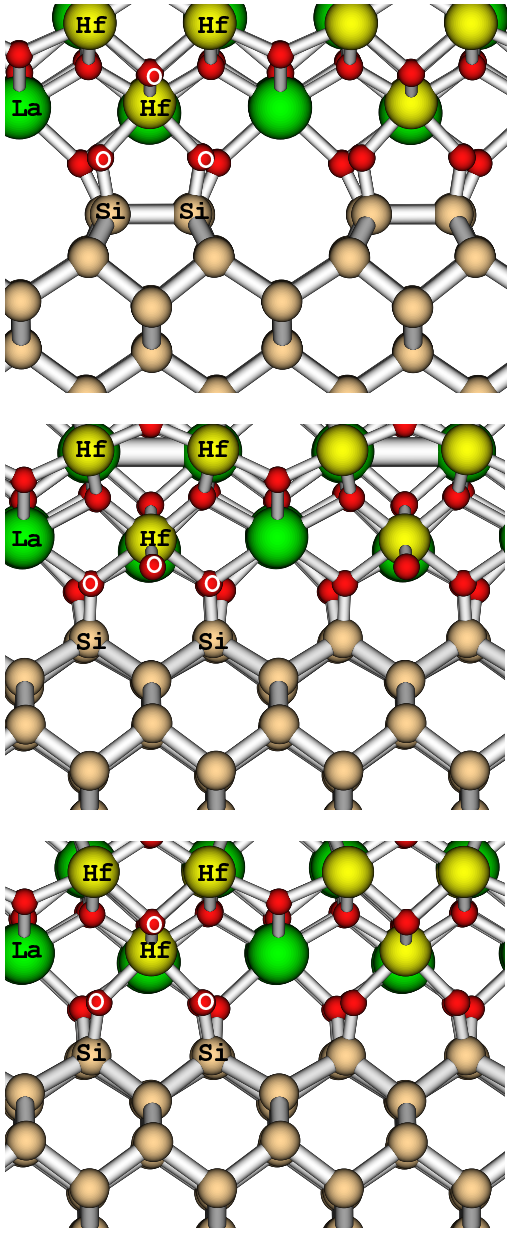


Figure 4.1: Interfacial structures of the $La_2Hf_2O_7/Si(001)$ interface. Top: Interface A. Middle: Interface B. Bottom: Interface C. The orientation of the Si crystal is the same for interfaces B and C. And this interfaces differ in the position of the oxygen atom binding to hafnium in the front of the figure. The labels indicate the type of atoms.

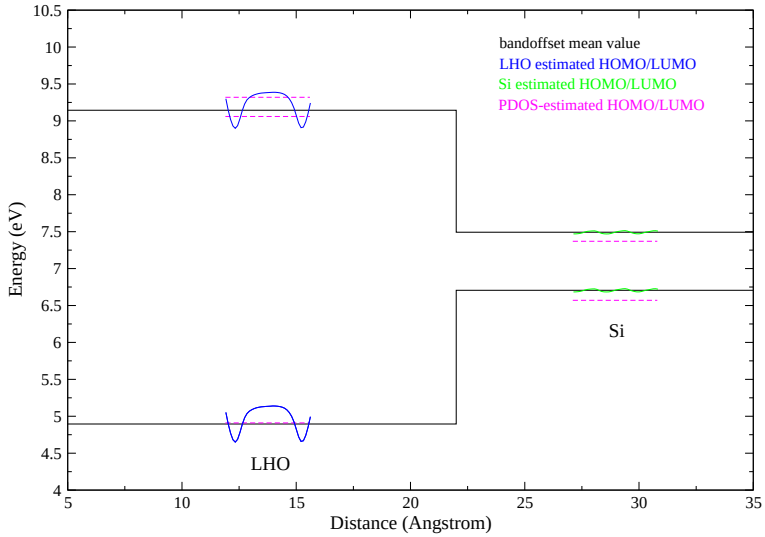


(a)

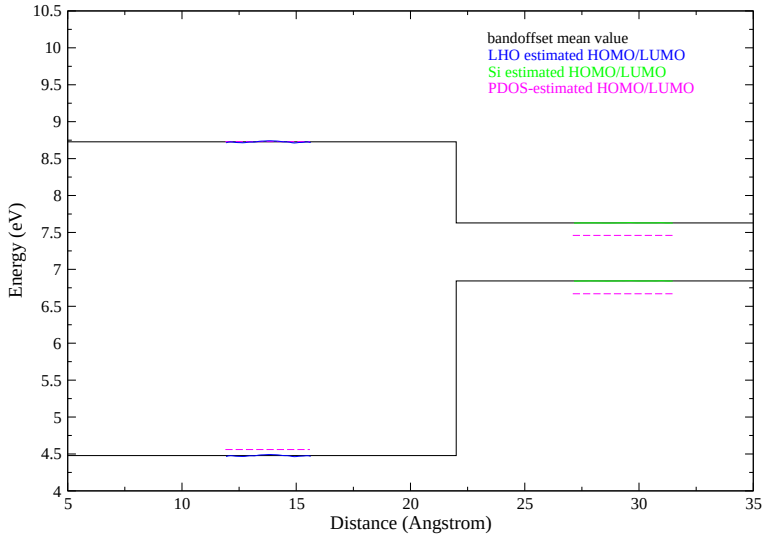


(b)

Figure 4.2: Schematic representation of the band offsets for (a) interface A, and (b) interface B. The blue and green lines are obtained after average bulk potential alignment and subtraction of the bulk potential from the potential in the bulk layers of the sandwich for $La_2Hf_2O_7$ and Si, respectively. The black lines are drawn from the mean values of the blue and green lines. Finally, the magenta broken line represents the alignment of the atomic low energy states in the sandwich to the bulk values obtained through the layer projected density of states.

and five oxygen atoms from the oxide. The position of the oxygen atoms is between the Si substrate and the $La_3Hf$ metal layer. Four of the interfacial oxygen atoms oxidize the dimerized Si atoms, and the fifth does not bind to Si. The studied interfaces differ in the relative orientation of the Si substrate to the oxide and the final relaxed position of the interfacial oxygen atom that does not bind to the Si substrate. The valence band offsets were determined for two interfaces using a method analogous to the experimental determination from x-ray photoelectron spectroscopy. It has been found that an interface where the interfacial oxygen atom has relaxed into the oxide, has a calculated valence band offset equal to $1.81 \pm 0.27$. And for the interface with a different Si orientation and where the interfacial oxygen atom remains at the inerface, the calculated valence band offset is $2.37 \pm 0.02$ eV. This large difference in the band offset is due to the presence of an electric dipole perpendicular to the interface, originated by the relaxation of the interfacial oxygen atom from the interface into the oxide.

# Chapter 5

# The $SrTiO_3$/GaAs(001) interface

## 5.1 Introduction

Crystalline metal-oxide/semiconductor systems are currently considered as alternatives to traditional silica-based technologies for transistor applications. Gate stacks made out of oxides grown on III-V semiconductors, such as gallium arsenide (GaAs), could in principle provide additional superior optical and electronic properties. The GaAs surface structures have been investigated in great detail by Penev et al. [69]. These studies show a large variability in structure and stoichiometry depending on the environment conditions. Nevertheless, it is possible that growth of the oxide film stabilizes one of the GaAs surface terminations.

Epitaxial growth of strontium titanate ($SrTiO_3$) on GaAs(001) has been successfully demonstrated by Liang [70, 71, 72]. Growth could be achieved both on gallium (Ga) terminated and arsenic (As) terminated GaAs(001) surfaces. However, for Ga-terminated substrates, outdiffusion of Ga has been detected. On the other hand, on the As-terminated substrates, important for an epitaxial growth mode was the deposition of titanium (Ti) prior to strontium (Sr). Using Ti 1/2ML as template, resulted in $SrTiO_3$ epitaxial growth. Z-contrast images of the $SrTiO_3/GaAs$(001) interface have been reported [71], providing important information on the interfacial structure. These Z-contrast images have been interpreted as indicating an interface consisting of an As-terminated GaAs(001) substrate facing a $SrO$ layer (followed by a $TiO_2$ layer) of the oxide. Thus, no interfacial Ti or $TiO_2$ layer was found. Moreover, it was shown that the Ti prelayer formed on an As-terminated GaAs(001) substrate resulted in band bending and Fermi level pinning. Nev-

ertheless, subsequent growth of epitaxial $SrTiO_3$ on the Ti-covered GaAs substrate alleviated the pinning at the interface. The band alignment of the interface has been studied using photoelectron spectroscopy [72]. The experiments indicate a conduction band offset of 0.6 eV and a valence band offset of 2.5 eV.

A detailed atomistic model of the interface and the driving force that unpins the Fermi level remain unclear. I have studied ab-initio the interfacial structure, stoichiometry and band offsets of the unpinned $SrTiO_3/GaAs$(001) interfaces, and the initial stages of $SrTiO_3$ growth on the As-terminated GaAs(001) substrate.

## 5.2 Computational Details

Total energy calculations were performed using the Projector Augmented Wave (PAW) method [22] (Section 2.4), which is based on density-functional theory [12] (Section 2.2). The generalized gradient approximation (GGA) as implemented by Perdew, Burke and Ernzerhof (PBE) [36] was used for the exchange-correlation potential. The valence wave functions were expanded in plane waves outside the augmentation region and inside, in partial waves. The plane wave *cut-off* was 30 Ry. The following valence electrons were considered: $2s^2 2p^4$ for oxygen, $3s^2 3p^6 4s^2 3d^2$ for titanium (Ti), $3d^{10} 4s^2 4p^1$ for gallium (Ga), $4s^2 4p^3$ for arsenic (As), and $4s^2 4p^6 5s^2$ for strontium (Sr). And the following sets of *projector* functions per angular momentum $(s, p, d)$ were used: $(2, 2, 1)$ for oxygen, $(2, 2, 2)$ for Ti, $(2, 2, 2)$ for Ga, $(2, 2, 1)$ for As, and $(3, 2, 2)$ for Sr. The semi-core states of Ti and Sr were treated as valence states. The frozen core approximation was used (Section 2.4.3). The typical underestimation of the band gap using density-functional theory was not corrected in this work.

The experimental lattice parameter of bulk GaAs is 5.654 Å(and band gap is 1.52 eV) [38] and that of bulk $SrTiO_3$ is 3.903 Å(and band gap is 3.2 eV) [73]. Thus, cube-on-cube epitaxy is not possible due to the large lattice mismatch (45 %), however, if the primitive vectors in the plane parallel to the (001) interface are rotated by 45 °, the lattice mismatch can be reduced to 2.4 %. The experimental lattice parameter of bulk GaAs was used.

The GaAs(001) substrate was simulated by a slab with five layers, that is, As-terminated on both sides of the slab. The periodicity of the surface unit cell corresponds to c(4x2)GaAs(001). A grid with four k-points per c(4x2)GaAs(001) surface unit cell was used to sample the Brillouin zone. There is a difficulty in passivating the back plane of the slab due to the fractional charge (1.25 e) of the As-dangling bonds at the surface. Each As

atom requires 0.75 e per dangling bond to become passivated (two dangling bonds per atom), thus hydrogen can not be used since it provides 1.0 e. An approach proposed by Shiraishi [74], that uses fractionally charged hydrogen atoms, *pseudo hydrogen* (Z=0.75), to terminate the back plane, has been used. This ensures that the back plane neither reconstructs nor is it electronically active. Three layers of $SrTiO_3$ were placed on top of the Sr-passivated GaAs(001) surface. The As-terminated back plane and the pseudo hydrogen layer were kept frozen, all other atomic coordinates were relaxed without symmetry constraints (except for time-inversion symmetry). The vacuum separating adjacent slab images in the direction perpendicular to the surface was never below 8 Å.

A first estimation of the valence band offsets determined by each interface was obtained through the analysis of the layer projected density of states. Bulk GaAs and bulk $SrTiO_3$ were calculated separately with the same accuracy and parameters used in the slab calculations. Subsequently, the layer projected density of states of the bulk materials was aligned to the corresponding bulk layers in the slab. Low energy atomic states in bulk GaAs and bulk $SrTiO_3$ were aligned to the same states in the bulk layers of the slab. In the case of GaAs the slab bulk layer is the frozen As-terminated back plane layer and for $SrTiO_3$, it is the uppermost (farthest from the interface) layer. It is interesting to note that the difference between the experimental band gap of bulk GaAs and bulk $SrTiO_3$ is equal to 1.68 eV. If the valence and conduction band offsets are symmetric, they are equal to 0.84 eV which may not be sufficient for transistor applications. Thus, only one type of charge carrier (electrons or holes) can be inhibited to occupy the conduction bands in the oxide.

## 5.3 The unpinned interfaces

Stable interfaces without Fermi-level pinning and adequate band offsets are required for transistor applications. Fermi level unpinning in the $SrTiO_3/GaAs$(001) system is in principle equivalent to the passivation of the As-terminated surface, since $SrTiO_3$ consists of neutral $SrO$ and $TiO_2$ layers along the [001] direction. On the other hand, the conduction and valence band offsets must be over 1 eV in order to inhibit conduction by the emission of electrons or holes from the semiconductor into the oxide conduction and valence bands, respectively.

As is pentavalent, thus, it can be assumed that each tetrahedral bond has a formal fractional charge of 1.25 e; similarly, for Ga the fractional charge is 0.75 e. At the surface, each As atom has two bonds saturated by the

subsurface Ga atoms and two dangling bonds sticking out of the surface, each formally charged with 1.25 e and requiring 0.75 e to become passivated. As mentioned above, the passivation of the As-terminated back plane of the slab required the use of fractionally charged pseudo hydrogen atoms, similarly, the other As-terminated, but chemically active, surface has to be passivated with a suitable species.

Since the experimental observations indicate an interface made out of an As layer and an $SrO$ layer, even though oxygen can not be resolved by the Z-contrast images, I have studied the passivation of the As-terminated surface with Sr and with variable amounts of oxygen, that is, the limiting cases of a fully oxidized and unoxidized interface.

To passivate the As-terminated surface, a charge transfer of 0.75x2=1.5 e per As atom is necessary, and in a c(4x2)GaAs(001) surface unit cell that amounts to 6 e. If Sr is used to passivate the surface (oxidation state is 2), then three Sr atoms per c(4x2) surface unit cell which corresponds to a coverage of 3/4ML will be necessary. Moreover, if the surface As atoms form dimers then 1 e per As atom is used to form the dimer, and then 2 e per c(4x2) surface unit cell need to be provided to passivate the surface. This amounts to one Sr atom per c(4x2) surface unit cell or a 1/4ML coverage.

Incorporation of oxygen into the interface layer will not change the charge count, because the charge transfer from Sr to As may still be accomplished via the oxygen layer. Nevertheless, the dipole formed at the interface will be different between an oxidized and unoxidized interface which will affect the band offsets.

Thus, four limiting cases were investigated: the As-dimerized interface with Sr 1/4ML, the undimerized interface with Sr 3/4ML, and both interfaces oxidized and unoxidized. In principle, mixtures of the four limiting cases may coexist at the interface. In order to minimize the electrostatic repulsion, an ordering of the interfacial Sr atoms in a c(4x2) pattern is anticipated, with the Sr atoms located in the valley between the As dimer rows, and occupying every alternate site in the center of four As dimers.

I have found that the unoxidized Sr 1/4ML interface with As dimers (Figure 5.1(a)) has a valence band offset of $0.97 \pm 0.25$ eV (Figure 5.1(b)), roughly in the limit for an adequate hole injection barrier (which should be larger than 1 eV). There are no states in the band gap (the calculated band gap is 0.9 eV), and the states in the vicinity of the band gap are interfacial states localized mainly in the As dimers and have antibonding character. This interface determines almost symmetric valence and conduction band offsets.

When the Sr 1/4ML interface is fully oxidized (Figure 5.2(a)), interfacial states appear in the band gap and pin the Fermi level. These states originate

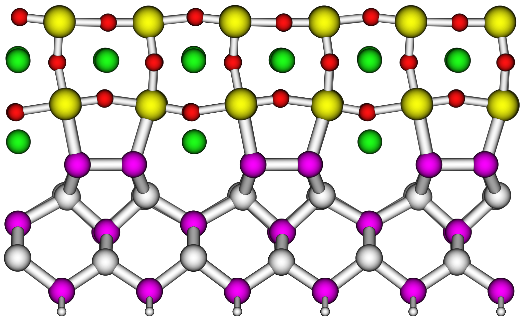

(a)

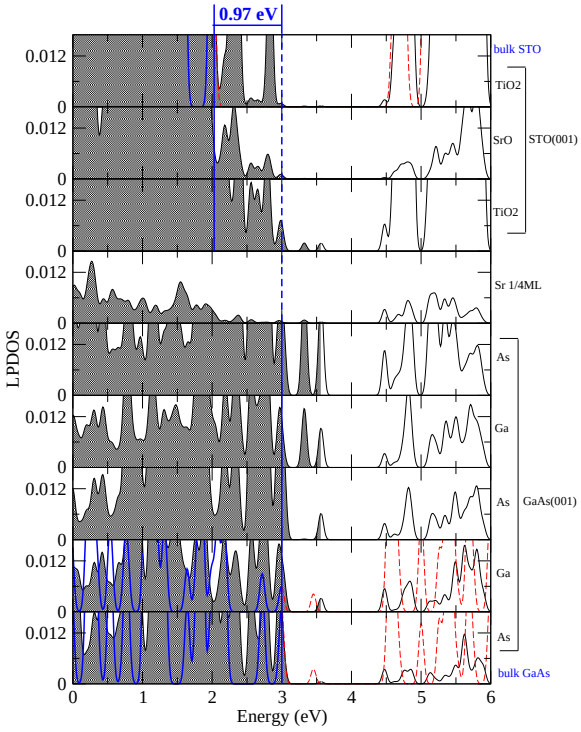


(b)

Figure 5.1: The Sr 1/4ML interface of $SrTiO_3/GaAs(001)$. (a) Interfacial structure. Oxygen, Ti, Sr, As, Ga, and pseudo hydrogen atoms are represented in red, yellow, green, purple, grey, and white, respectively. (b) Layer projected density of states and valence band offset. The shaded region indicates the occupied bands of the slab, and the blue line the occupied bands in the bulk material.

from the interaction between the antibonding orbitals of the As dimers and the oxygen atoms. Moreover, this interface exhibits a small negative valence band offset, $-0.23 \pm 0.10$ eV (Figure 5.2(b)). This indicates that holes from the semiconductor are injected into the oxide valence bands creating a large surface dipole. This structure is likely to be unstable and needs further investigation.

Oxidation produces the opposite effect in the undimerized Sr 3/4ML interface. The unoxidized Sr 3/4ML interface (Figure 5.3(a)) has states in the band gap, and thus Fermi level pinning, making it unsuitable for transistor applications (Figure 5.3(b)). These states are localized at the interface and have bonding character between Sr and As, and Ti and As.

Oxidation of the Sr 3/4ML interface (Figure 5.4(a)) results in a strong interaction between oxygen and As and the opening of the bandgap; the calculated band gap is 1.9 eV. The estimated valence band offset is 1.53±0.25 eV (Figure 5.4(b)). This valence band offset is suitable to prevent injection of holes into the oxide bands. However, when the value of the calculated band gap is added to that of the valence band offset, the resulting value is slightly larger than that of the band gap of bulk $SrTiO_3$, which means that the conduction band offset is negative and can not prevent injection of electrons into the oxide bands. Nevertheless, these calculated band offsets are in qualitative agreement with the experimentally measured ones [72]. Moreover, the atomic structure of this undimerized interface, has strong similarities with the Z-contrast images and structural model proposed by Klie et al. [71], and taking into consideration that oxygen is not visible in these images. The comparison is shown in Figure 5.5.

Finally, Klie's observation that $SrTiO_3$ growth on the As-terminated GaAs(001) surface by direct Sr and Ti co-deposition in the presence of molecular oxygen resulted in Fermi level pinning, might be explained by a higher concentration of oxygen vacancies (relative to 1ML) and/or a lower concentration of Sr (relative to 3/4ML) at the interface. This is because the unoxidized Sr 3/4ML and the oxidized Sr 1/4ML interfaces have states in the band gap.

## 5.4 The initial stages of $SrTiO_3$ growth on GaAs(001)

Klie et al. [71] reported that the epitaxial growth of $SrTiO_3$ on GaAs(001) could be achieved using two different growth methods: By deposition of Ti 1/2ML on the As-terminated GaAs(001) followed by co-deposition of both Sr

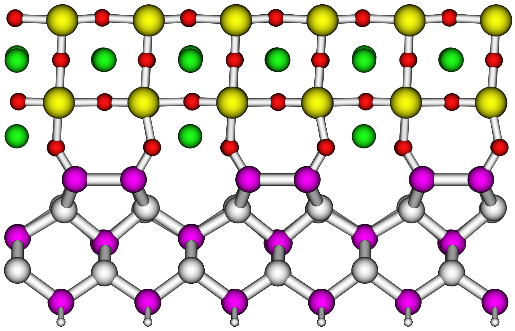

(a)

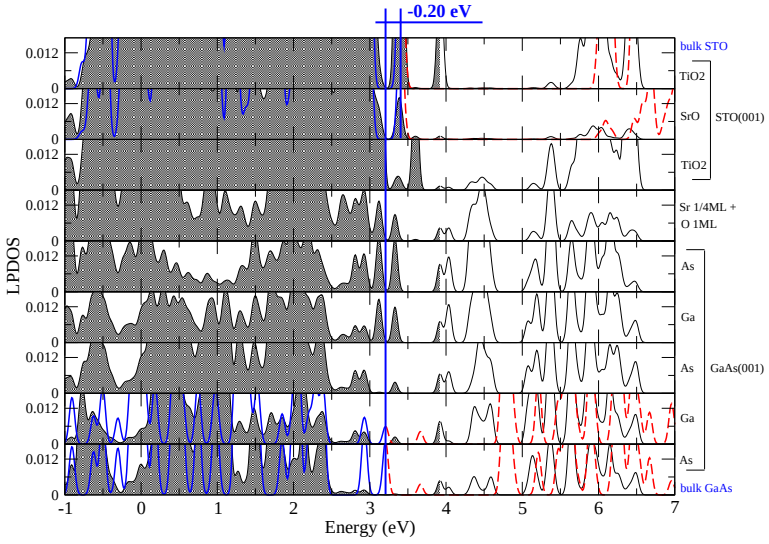


(b)

Figure 5.2: The Sr 1/4ML oxidized interface of $SrTiO_3/GaAs$(001). (a) Interfacial structure. (b) Layer projected density of states indicating slightly negative valence band offset. The color scheme is the same as in Figure 5.1.

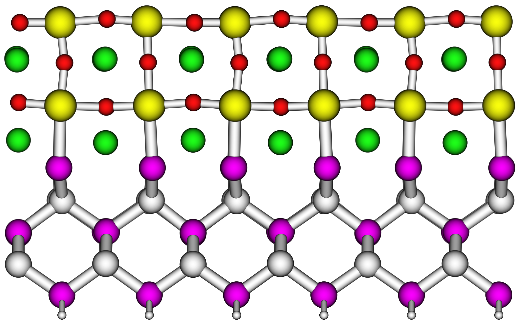

(a)

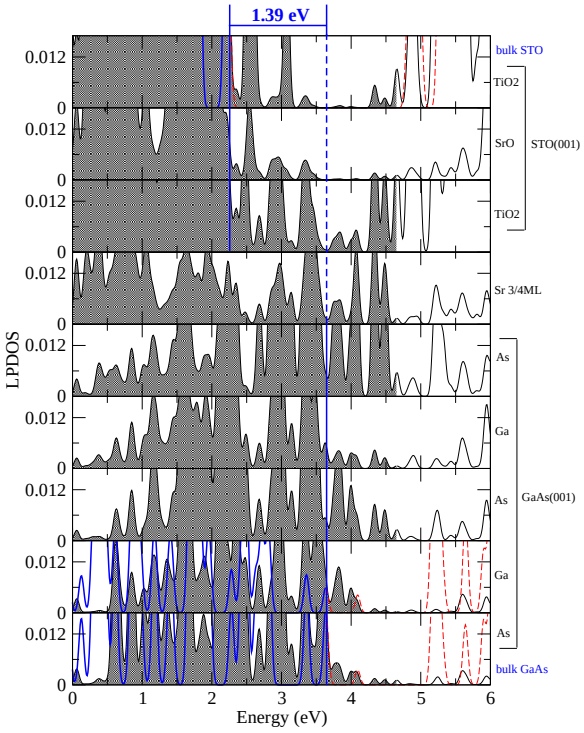


(b)

Figure 5.3: The Sr 3/4ML interface of $SrTiO_3/GaAs$(001). (a) Interfacial structure. (b) Layer projected density of states and valence band offset. The color scheme is the same as in Figure 5.1.

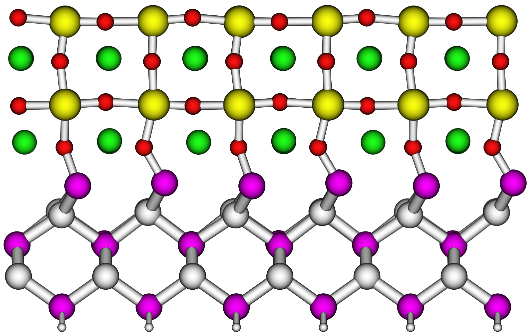

(a)

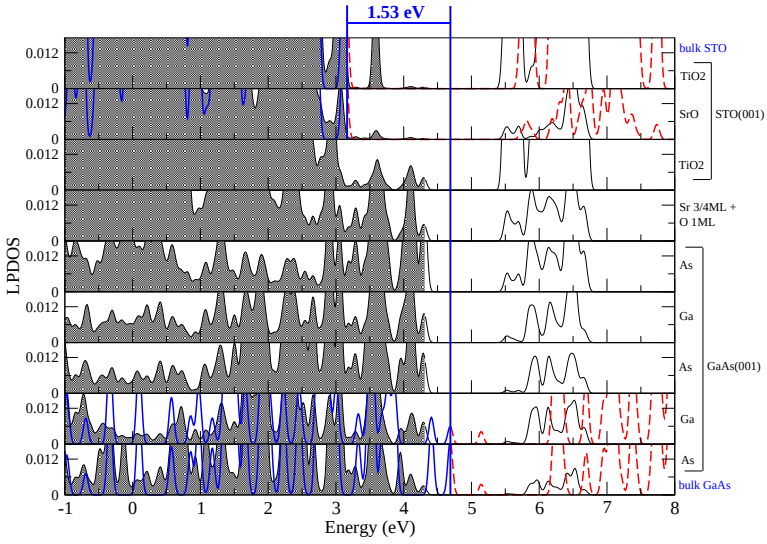


(b)

Figure 5.4: The Sr 3/4ML oxidized interface of $SrTiO_3/GaAs$(001). (a) Interfacial structure. (b) Layer projected density of states and valence band offset. The color scheme is the same as in Figure 5.1.

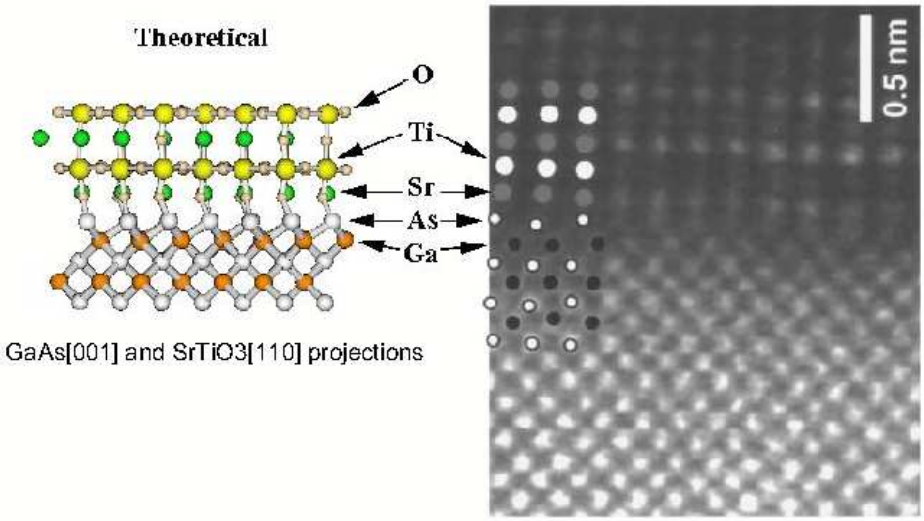


Figure 5.5: Comparison of the calculated Sr 3/4ML oxidized interfacial structure (left) with the Z-constrast image and proposed structural model of Ref. [71] (right).

and Ti in the presence of molecular oxygen (first method), and by direct Sr and Ti co-deposition in the presence of molecular oxygen (second method). Both methods resulted in the presence of Sr at the interface after $SrTiO_3$ growth, which indicates the possibility of Ti diffusion in the presence of Sr and oxygen in the first method. I have simulated the deposition of Ti 1/2ML on the As-terminated GaAs(001) substrate in order to gain insight into the initial stages of oxide growth through the first method.

At Ti 1/2ML coverage, a passivated and undimerized As-terminated GaAs(001) surface requires that the oxidation state of Ti is +3. Ti adsorbs at interstitial sites on the surface and seems to be incorporated which might be due to its small ionic radius (Figure 5.6(a)). This surface structure has states in the bandgap which is in agreement with the Fermi level pinning observed after deposition of Ti 1/2ML in the experiments by Klie et al. [71]. Oxidation of this surface structure with 1ML oxygen results in the opening of the band gap (the calculated value is 1 eV) in a way similar to the undimerized As terminated surface saturated by Sr 3/4ML. The oxygen atoms bind to the Ti and As atoms on the surface (Figure 5.6(b)). At this coverage, the stoichiometry of the materials deposited on the GaAs surface, Ti 1/2ML and oxygen 1ML, corresponds to $TiO_2$, nevertheless, this is not yet one layer of the $SrTiO_3$ oxide (which should consist of Ti 1ML and O 2ML).

When oxygen and Sr are co-deposited, Ti may make a transition to its

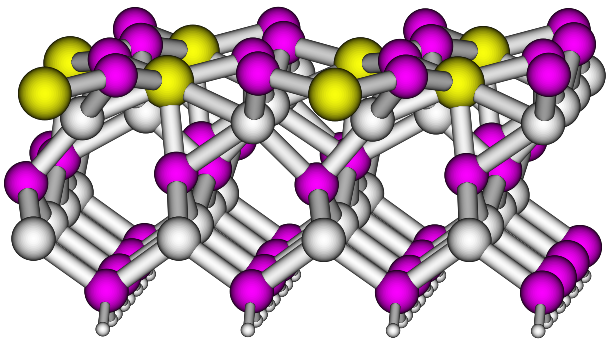

(a)

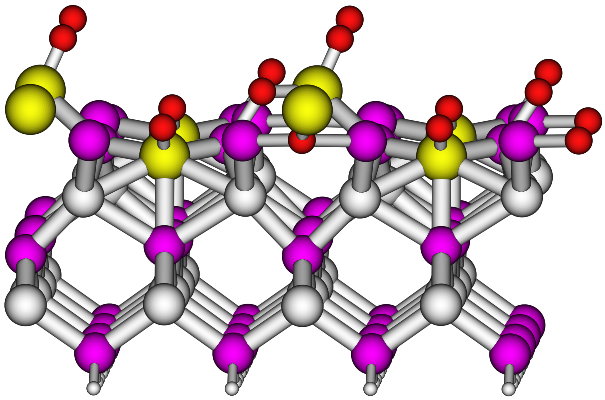

(b)

Figure 5.6: The structure of Ti 1/2ML deposited on the As-terminated GaAs(001) surface. (a) Unoxidized. (b) Oxidized. The color scheme is the same as in Figure 5.1.

most stable +4 oxidation state, and then a reduced Ti 3/8ML coverage will be necessary to passivate the undimerized As-terminated GaAs(001) surface. On the other hand, as discussed above, a higher Sr 3/4ML coverage will passivate the same undimerized surface. The lower coverage and the small ionic radius and high diffusivity of Ti, may promote diffusion of Ti and Sr out of and into the interface, respectively. Finally, as discussed above, the fully oxidized Sr 3/4ML interface structure determines a large band gap which might corroborate Klie's observation that in the first method the Fermi level pinning is alleviated after $SrTiO_3$ growth.

## 5.5 Summary

The $SrTiO_3/GaAs$(001) interfaces without Fermi level pinning have been investigated. At the interface, the As-terminated GaAs(001) substrate has been reported to face the $SrO$ layer of the oxide. Therefore, passivation of the GaAs(001) surface with variable amounts of Sr and oxygen were studied. Four limiting cases were identified: the As-dimerized interface with Sr 1/4ML, the undimerized interface with Sr 3/4ML, and both interfaces oxidized and unoxidized. It was found that the oxidized Sr 1/4ML and the unoxidized Sr 3/4ML interfaces have states in the band gap originating from the interaction between As and oxygen and the metal atoms in the oxide, respectively. These interfaces have Fermi level pinning and are unsuitable for transistor applications. The two interfaces without Fermi level pinning are: The unoxidized Sr 1/4ML interface with a band gap of 0.9 eV and a valence band offset of $0.97 \pm 0.25$ eV, and the oxidized Sr 3/4ML interface with a band gap of 1.9 eV and a valence band offset of $1.53 \pm 0.25$ eV. The former determines almost symmetric valence and conduction band offsets which are in the limit of being suitable for transistor applications. On the other hand, the latter interface has a suitable valence band offset and the band alignment is qualitatively similar to that measured experimentally. Moreover, the atomic structure of this interface has strong similarities with the reported Z-contrast images, suggeting that the real interface may be close to being stoichiometric, as a $SrO$ layer from the oxide. And deviations from the oxidized Sr 3/4ML may lead to Fermi level pinning. The initial stages of $SrTiO_3$ growth on a GaAs surface covered with Ti 1/2ML has also been investigated. It was found that at Ti 1/2ML coverage the surface is undimerized and the Fermi level is pinned. Oxidation of this surface results in opening of the bandgap. During deposition of the oxide, the oxidation state of Ti may change from +3 to +4 (the most stable one), which determines a lower Ti coverage necessary to passivate the surface. On the other hand, the Sr 3/4ML coverage is higher

and also passivates the surface. The lower Ti coverage relative to Sr (due to the change in oxidation state) and the small ionic radius and high diffusivity of Ti, may be responsible for the observed presence of Sr at the interface and complete absence of the initial Ti layer.

# Chapter 6

# Summary

In this work the growth process of the technologically relevant system $Ge/SrHfO_3(001)$ has been studied theoretically by means of the Projector-Augmented Wave (PAW) method. The PAW method is based on *Density Functional Theory* and it is implemented in the Car-Parrinello Ab-Initio Molecular Dynamics. It is an *all-electron* method that treats explicitly the core and valence electrons and gives access to the complete (also close to the nucleus) wave function. Direct heteroepitaxial growth of Ge on an oxide results in a Ge film with a large density of defects, unsuitable for transistor applications, due to the fact that the semiconductor grows in 3D-islands on the oxide. In order to obtain high quality Ge films, the growth mode of Ge has to be changed to layer-by-layer growth. A surfactant is a third material that could in principle change the growth mode, and I have investigated the possibility of using such an approach to achive layer-by-layer growth of Ge on the $SrHfO_3(001)$ substrate.

The stable $SrO$ and $HfO_2$ terminations of the $SrHfO_3(001)$ surface have been taken into account by using two differently terminated slabs. I have found that direct Ge deposition on these surfaces results in clustering. The Ge adatoms seek to minimize their energy by saturating their dangling bonds and so they prefer to make bonds to other Ge adatoms on the surface and form clusters, than to make bonds to the surface oxygen atoms. Nevertheless, at Ge 1ML coverage, a metastable epitaxial structure made out of diagonal-rows of dimers was found on the $SrO$ surface. This epitaxial structure could in principle be stabilized by reducing the mobility of Ge atoms on the surface (e.g. low temperature growth).

For heteroepitaxial growth, the structural compatibility between growing film and substrate is essential. A suitable surfactant should segregate to the surface, reduce the surface free energy, and modify the growth kinetics to improve the surface morphology. The feasibility of using Sb as surfactant

for Ge layer-by-layer heteroepitaxial growth was investigated, since Sb is a traditional surfactant for Ge growth. It was found that Sb does not wet the $SrHfO_3(001)$ substrate, and may have low adhesion to it. Consequently, formation of ordered Sb structures on the surface, that could modify the growth mode and growth kinetics of Ge on the surface, is difficult. Thus, deposition of Sb prior to Ge on the $SrO$-terminated $SrHfO_3(001)$ surface does not lead to epitaxial Ge layer-by-layer growth. On the other hand, previous studies have indicated that Sr can passivate the Si(001) surface and provide a technologically relevant interface for the $SrTiO_3/Si(001)$ system. Consideration of these findings in the context of surfactant-mediated layer-by-layer growth of Ge on $SrHfO_3(001)$, provide indications that Sr could determine a stable interface with good transistor properties, and may act as surfactant for Ge layer-by-layer growth. Therefore, the feasibility of forming an ordered Sr 1ML film on the oxide surface, to be used as template for Ge overgrowth, was investigated.

It was found that, on the $SrO$ termination, careful control of the experimental conditions may lead to the formation of the Sr 1ML film. During Sr deposition, the first and second monolayers may be formed simultaneously, nevertheless, in a small energy window between the activation energy for diffusion (0.65 eV) and the binding energy (1.09 eV) of the isolated adatom on the bare surface, formation of the second monolayer may be hindered in favor of formation of the first monolayer. Moreover, it is unlikely that an ordered Sr 1/2ML film can be formed in this way on the $SrO$ termination.

The formation of a Sr 1ML film on the $SrHfO_3(001)$ substrate increases the reactivity of the surface, which could in principle change the growth mode and growth kinetics of Ge. However, it is expected that such a chemically reactive Sr surface can be easily oxidized. Oxidation of the Sr 1ML template will result in Ge clustering on the surface since the oxidized Sr 1ML film is equivalent to a $SrO$ layer, where it is known that Ge clusters. It has been found that oxidation from the oxide subsurface layer is not thermodynamically favorable. Additionally it is important to maintain the oxygen contamination in the growth chamber at an insignificant level. The atomization energy of the Sr 1ML film is equal to 1.39 eV/Sr, and it determines the upper limit for the diffusion and desorption processes involving the use of the Sr 1ML template.

Deposition of Ge on the Sr 1ML template results in Ge wetting of the substrate and a change of the growth mode to layer-by-layer. However, the diffusion barrier (2.12 eV) is larger than the atomization energy of the Sr 1ML film, so diffusion can not be activated at low coverages of Ge. In addition, it was found that a Ge adatom adsorbed at the hollow site on the Sr 1ML film will not incorporate in the substrate and instead will remain on top of

the Sr 1ML surface.

At Ge 1/2ML coverage on the Sr 1ML-covered $SrHfO_3(001)$ surface, the stable configuration is epitaxial and consists of Ge atoms adsorbed at hollow sites. Nevertheless other metastable configurations may form on the surface due to the suppression of diffusion. Increasing the Ge coverage does not necessarily result in a surface structure with increased occupation of hollow sites. The equilibrium configuration of a Ge 3/4ML film on the Sr 1ML template is a short chain. This short chain structure is epitaxial and is an structural element of the Ge(001) 2ML film. The short chain structure indicates that the initial stages of Ge growth may not be layer-by-layer (which would correspond to the initial occupation of all the available hollow sites on the Sr 1ML template). Instead, it seems that Ge forms initially a compound with Sr that stabilizes the Ge epitaxial growth.

At Ge coverages between 1ML and 2ML there are many degenerate structures that may indicate a disordered configuration on the surface or the formation process of a Sr-Ge compound. Moreover, it has been found that Sr diffuses from the interfacial Sr 1ML film to the Ge surface. So the Sr 1ML film does not remain at the interface during Ge growth and segregates to the Ge surface. Sr 1/2ML remains at the interface and the other half diffuses to the Ge surface. A Ge thin film with Sr 1/2ML on both surfaces is a passivated surface structure, and is expected to be more stable than other unpassivated surface configurations.

After the formation of the passivated epitaxial Ge film, Sr 1/2ML at the interface stabilizes the Ge epitaxial film and passivates the dangling bonds to unpin the Fermi level. Sr 1/2ML at the Ge(001) surface should passivate the dangling bonds but also may act as a surfactant since it lowers the surface energy of Ge(001). Moreover, due to the large atomic radius of Sr (2.45 Å) it is expected that it does not incorporate in bulk Ge during growth.

The Sr interfaces of the $Ge/SrHfO_3(001)$ system were studied. It was found that an unoxidized Sr 1/2ML interface provides suitable band offsets for transistor applications, whereas the oxidized Sr 1/2ML interface determines a hole injection barrier that is too small.

The $La_2Hf_2O_7$ oxide is a complex oxide that has promising electrical and structural characteristics for transistor applications and integration with Si. The interfacial structure and valence band offsets of the $La_2Hf_2O_7/Si(001)$ crystalline system were studied. For the $La_3HfO_5$ class of interfaces, three interfacial structures that unpin the Fermi level were investigated and found to be degenerate. These interfacial structures consist of a (2x2)Si(001) dimerized surface and five oxygen atoms from the oxide, with four of them oxidizing the Si atoms, and they differ in the relative orientation of the Si substrate

and the relaxed position of the interfacial oxygen atom that does not bind to the Si substrate. The valence band offsets were determined for two interfaces using a method analogous to the experimental determination from x-ray photoelectron spectroscopy. For the interface where the interfacial oxygen atom has relaxed into the oxide, the calculated valence band offset is equal to $1.81 \pm 0.27$ eV. And for the interface with different Si orientation and where the interfacial oxygen atom remains at the interface, the calculated valence band offset is $2.37 \pm 0.02$ eV. The large difference is due to the presence of an electric dipole perpendicular to the interface, originated by the relaxation of the interfacial oxygen atom from the interface into the oxide.

The $SrTiO_3/GaAs(001)$ gate stack may provide superior optical and electronic properties compared to the oxide grown on Si. The technologically relevant $SrTiO_3/GaAs(001)$ interfaces, without Fermi level pinning, have been investigated. Passivation of the GaAs(001) surface with variable amounts of Sr and oxygen were studied due to the experimental evidence that the As-terminated GaAs(001) substrate faces the $SrO$ layer of the oxide. Four limiting cases were identified: the As-dimerized interface with Sr 1/4ML, the undimerized interface with Sr 3/4ML, and both interfaces oxidized and unoxidized. It was found that the oxidized Sr 1/4ML and the unoxidized Sr 3/4ML interfaces have states in the band gap, and Fermi level pinning, originating from the interaction between As and oxygen and the metal atoms in the oxide, respectively. The interfaces without Fermi level pinning are the unoxidized Sr 1/4ML interface with a valence band offset of $0.97 \pm 0.25$ eV, and the oxidized Sr 3/4ML interface with a valence band offset of $1.53 \pm 0.25$ eV. The former determines almost symmetric valence and conduction band offsets which are in the limit of being suitable for transistor applications. On the other hand, the latter interface determines a suitable valence band offset but insufficient conduction band offset. The band alignment and atomic structure of this interface are qualitatively similar to the experimental reports. The initial stages of $SrTiO_3$ growth on a Ti 1/2ML covered GaAs(001) surface has also been investigated. It was found that at Ti 1/2ML coverage the surface is undimerized and the Fermi level is pinned. Oxidation of this surface results in opening of the bandgap. Moreover, during deposition of $SrTiO_3$, the oxidation state of Ti may change from +3 to +4 (the most stable one) which determines a lower Ti coverage necessary to passivate the surface. Sr 3/4ML, on the other hand, is a higher coverage and also passivates the surface. The complete absence of the initial Ti layer at the interface after $SrTiO_3$ growth, may be due to the small ionic radius and high diffusivity of Ti but also to the lower Ti coverage (when the oxidation state is +4) necessary to produce a passivated GaAs(001) surface.

# Bibliography


[1] G. E. Moore. *Electronics*, 38:114, 1965.

[2] Semiconductor Industry Association. *International Technology Roadmap for Semiconductors, at http://public.itrs.net/.* International SEMATECH, Austin, 2003.

[3] B. Vincent, J.-F. Damlencourt, P. Rivallin, E. Nolot, C. Licitra, Y. Morand, and L. Clavelier. *Semicond. Sci. Technol.*, 22:237, 2007.

[4] T. Akatsu, C. Deguet, L. Sanchez, F. Allibert, D. Rouchon, T. Signamarcheix, C. Richtarch, A. Boussagol, V. Loup, F. Mazen, J.-M. Hartmann, Y. Campidelli, L. Clavelier, F. Letertre, N. Kernevez, and C. Mazure. *Mat. Sci. Semicond. Proc.*, 9:444, 2006.

[5] S. W. Bedell, A. Reznicek, K. Fogel, J. Ott, and D. K. Sadana. *Mat. Sci. Semicond. Proc.*, 9:423, 2006.

[6] T. Tezuka, N. Sugiyama, and S. Takagi. *Appl. Phys. Lett.*, 79:1798, 2001.

[7] Y. Liu, M. D. Deal, and J. D. Plummer. *Appl. Phys. Lett.*, 84:2563, 2004.

[8] M. Copel, M. C. Reuter, E. Kaxiras, and R. M. Tromp. *Phys. Rev. Lett.*, 63:632, 1989.

[9] H. J. Osten, J. Klatt, G. Lippert, E. Bugiel, and S. Hinrich. *Appl. Phys. Lett.*, 60:2522, 1992.

[10] N. W. Ashcroft and N. D. Mermin. *Solid State Physics.* Saunders College, Philadelphia, 1976.

[11] R. G. Parr and W. Yang. *Density-Functional Theory of Atoms and Molecules.* Oxford University Press, New York, 1989.

[12] P. Hohenberg and W. Kohn. *Phys. Rev.*, 136:B864, 1964.

[13] W. Kohn and L. J. Sham. *Phys. Rev.*, 140:A1133, 1965.

[14] W. Kohn. *Rev. Mod. Phys.*, 71:1253, 1999.

[15] R. Car and M. Parrinello. *Phys. Rev. Lett.*, 55:2471, 1985.

[16] G. Pastore, E. Smargiassi, and F. Buda. *Phys. Rev. A*, 44:6334, 1991.

[17] J. F. Janak. *Phys. Rev. B*, 18:7165, 1978.

[18] G. W. Fernando, G.-X. Qian, M. Weinert, and J. W. Davenport. *Phys. Rev. B*, 40:7985, 1989.

[19] R. P. Feynman. *Phys. Rev.*, 56:340, 1939.

[20] P. Bendt and A. Zunger. *Phys. Rev. Lett.*, 50:1684, 1983.

[21] P. E. Blöchl and M. Parrinello. *Phys. Rev. B*, 45:9413, 1992.

[22] P. E. Blöchl. *Phys. Rev. B*, 50:17953, 1994.

[23] H. M. Petrilli, P. E. Blöchl, P. Blaha, and K. Schwarz. *Phys. Rev. B*, 57:14690, 1998.

[24] O. K. Andersen. *Phys. Rev. B*, 12:3060, 1975.

[25] D. R. Hamann, M. Schlüter, and C. Chiang. *Phys. Rev. Lett.*, 43:1494, 1979.

[26] P. E. Blöchl, C. J. Först, and J. Schimpl. *B. Mater. Sci.*, 26:33, 2003.

[27] D. D. Koelling and B. N. Harmon. *J. Phys. C: Solid State Phys.*, 10:3107, 1977.

[28] L. Verlet. *Phys. Rev.*, 159:98, 1967.

[29] R. E. Allen, G. P. Alldredge, and F. W. de Wette. *Phys. Rev. B*, 4:1648, 1971.

[30] M. L. Cohen, M. Schlütter, J. R. Chelikowsky, and S. G. Louie. *Phys. Rev. B*, 12:5575, 1975.

[31] P. E. Blöchl. *J. Chem. Phys.*, 103:7422, 1995.

[32] J. R. Chelikowsky, M. Schlüter, S. G. Louie, and M. L. Cohen. *Solid State Commun.*, 17:1103, 1975.

[33] M. Schlüter, J. R. Chelikowsky, S. G. Louie, and M. L. Cohen. *Phys. Rev. B*, 12:4200, 1975.

[34] J. Neugebauer and M. Scheffler. *Phys. Rev. B*, 46:16067, 1992.

[35] C. Rossel, B. Mereu, C. Marchiori, D. Caimi, M. Sousa, A. Guiller, H. Siegwart, R. Germann, J. P. Locquet, J. Fompeyrine, D. J. Webb, Ch. Dieker, and J. W. Seo. *Appl. Phys. Lett.*, 89:053506, 2006.

[36] J. P. Perdew and K. Burke e M. Ernzerhof. *Phys. Rev. Lett.*, 77:3865, 1996.

[37] B. J. Kennedy, C. J. Howard, and B. C. Chakoumakos. *Phys. Rev. B*, 60:2972, 1999.

[38] C. S. Wang and B. M. Klein. *Phys. Rev. B*, 24:3393, 1981.

[39] G. Fabricius, E. L. Peltzer y Blanca, C. O. Rodriguez, A. P. Ayala, P. de la Presa, and A. Lopez Garcia. *Phys. Rev. B*, 55:164, 1997.

[40] P. W. Tasker. *J. Phys. C.: Solid State Phys.*, 12:4977, 1979.

[41] J. Goniakowski and C. Noguera. *Surf. Sci.*, 365:L657, 1996.

[42] J. W. Seo, Ch. Dieker, A. Tapponnier, C. Marchiori, M. Sousa, J. P. Locquet, J. Fompeyrine, A. Ispas, C. Rossel, Y. Panayiotatos, A. Sotiropoulos, and A. Dimoulas. *Microelectron. Eng.*, 84:2328, 2007.

[43] J. W. Seo, J. Fompeyrine, and A. Dimoulas. *private communication.*

[44] D. J. Eaglesham, F. C. Unterwald, and D. C. Jacobson. *Phys. Rev. Lett.*, 70:966, 1993.

[45] J. Neugebauer, T. K. Zywietz, M. Scheffler, J. E. Northrup, H. Chen, and R. M. Feenstra. *Phys. Rev. Lett.*, 90:056101, 2003.

[46] D. Kandel and E. Kaxiras. *Phys. Rev. Lett.*, 75:2742, 1995.

[47] E. Kaxiras. *Mater. Sci. Eng. B*, 30:175, 1995.

[48] B. Voigtländer and A. Zinner. *Surf. Sci. Lett.*, 292:L775, 1993.

[49] N. A. Bojarczuk, M. Copel, S. Guha, V. Narayanan, E. J. Preisler, F. M. Ross, and H. Shang. *Appl. Phys. Lett.*, 83:5443, 2003.

[50] S. Guha, N. A. Bojarczuk, and V. Narayanan. *Appl. Phys. Lett.*, 80:766, 2002.

[51] Y. Panayiotatos. *private communication.*

[52] C. J. Först, C. R. Ashman, K. Schwarz, and P. E. Blöchl. *Nature*, 427:53, 2004.

[53] R. A. McKee, F. J. Walker, and M. F. Chisholm. *Phys. Rev. Lett.*, 81:3014, 1998.

[54] C. R. Ashman, C. J. Först, K. Schwarz, and P. E. Blöchl. *Phys. Rev. B*, 69:075309, 2004.

[55] A. Franciosi, P. Soukiassian, P. Philip, S. Chang, A. Wall, A. Raisanen, and N. Troullier. *Phys. Rev. B*, 35:910, 1987.

[56] E. Heifets, S. Piskunov, E. A. Kotomin, Y. F. Zhukovskii, and D. E. Ellis. *Phys. Rev. B*, 75:115417, 2007.

[57] T. Kubo and H. Nozoye. *Surf. Sci.*, 542:177, 2003.

[58] L. M. Liborio, C. G. Sanchez, A. T. Paxton, and M. W. Finnis. *J. Phys.: Condens. Matter*, 17:L223, 2005.

[59] F. Bottin and F. Finocchi. *Phys. Rev. B*, 76:165427, 2007.

[60] J. A. Venables. *Introduction to Surface and Thin Film Processes.* Cambridge University Press, Cambridge, 2000.

[61] A. Molle. *private communication.*

[62] M. Kawasaki, K. Takahashi, T. Maeda, R. Tsuchiya, M. Shinohara, O. Ishiyama, T. Yonezawa, M. Yoshimoto, and H. Koinuma. *Science*, 266:1540, 1994.

[63] E. Zintl. *Angew. Chem.*, 52:1, 1939.

[64] A. Dimoulas, G. Vellianitis, G. Mavrou, G. Apostolopoulos, A. Travlos, C. Wiemer, M. Fanciulli, and Z. M. Rittersma. *Appl. Phys. Lett.*, 85:3205, 2004.

[65] G. Vellianitis, G. Apostolopoulos, G. Mavrou, K. Argyropoulos, A. Dimoulas, J. C. Hooker, T. Conard, and M. Butcher. *Mat. Sci. Eng. B*, 109:85, 2004.

[66] S. Spiga, C. Wiemer, G. Tallarida, G. Scarel, S. Ferrari, G. Seguini, and M. Fanciulli. *Appl. Phys. Lett.*, 87:112904, 2005.

[67] K. Kunc and R. M. Martin. *Phys. Rev. B*, 24:3445, 1981.

[68] E. A. Kraut, R. W. Grant, J. R. Waldrop, and S. P. Kowalczyk. *Phys. Rev. B*, 28:1965, 1983.

[69] E. Penev, P. Kratzer, and M. Scheffler. *Phys. Rev. Lett.*, 93:14602, 2004.

[70] Y. Liang, J. Kulik, T. C. Eschrich, R. Droopad, Z. Yu, and P. Maniar. *Appl. Phys. Lett.*, 85:1217, 2004.

[71] R. F. Klie, Y. Zhu, E. I. Altaman, and Y. Liang. *Appl. Phys. Lett.*, 87:143106, 2005.

[72] Y. Liang, J. Curless, and D. McCready. *Appl. Phys. Lett.*, 86:082905, 2005.

[73] F. Bottin, F. Finocchi, and C. Noguera. *Phys. Rev. B*, 68:035418, 2003.

[74] K. Shiraishi. *J. Phys. Soc. Jpn.*, 59:3455, 1990.

# List of Total Energies

A list of the total energies of all the calculations used in Chapter 3 are presented in the following tables. The reference (total) energies used to calculate adsorption and formation energies are presented first.

| System | Notation | Total Energy (Hartree) | Reference energy |
|---|---|---|---|
| Isolated Ge atom | $E^{Ge}_{atom}$ | -3.8894264 | Eqs. (3.1) and (3.5) |
| Bulk Ge (64 atoms) | $E^{Ge}_{bulk} \times 64$ | -259.0964038 | Eqs. (3.2) and (3.6) |
| Isolated Sr atom | $E^{Sr}_{atom}$ | -31.0586147 | Eq. (3.3) |
| Bulk Sr atom | $E^{Sr}_{bulk}$ | -31.1073816 | Eq. (3.4) |
| Bare $SrO$-terminated $SrHfO_3$(001) surface ($SrO$-termination) | $E^{SrHfO_3}_{slab}$ | -1040.9382584 | Eqs. (3.1), (3.2), (3.3) and (3.4) |
| Bare $HfO_2$-terminated $SrHfO_3$(001) surface ($HfO_2$-termination) | $E^{SrHfO_3}_{slab}$ | -1040.9118525 | Eqs. (3.1) and (3.2) |
| Sr 1ML film formed on $SrO$-termination | $E^{Sr+SrHfO_3}_{slab}$ | -1165.3770087 | Eqs. (3.5) and (3.6) |

| System | Total Energy (Hartree) | Details |
|---|---|---|
| Ge adatom at oxygen site on $SrO$-termination | -1044.9173121 | Section 3.5.1 Figure 3.4(a) |
| Ge adatom at oxygen site on $HfO_2$-termination | -1044.9072301 | Section 3.5.1 Figure 3.4(b) |
| Ge at barrier configuration on $SrO$-termination | -1044.8979306 | Section 3.5.1 |
| Ge at barrier configuration on $HfO_2$-termination (Path A) | -1044.9023416 | Section 3.5.1 |
| Ge at barrier configuration on $HfO_2$-termination (Path B) | -1044.8958878 | Section 3.5.1 |
| Ge 1ML adsorbed on $HfO_2$-termination (most stable structure) | -1057.0370098 | Section 3.5.2 Figure 3.9 |
| Ge 1ML adsorbed on $HfO_2$-termination | -1057.0114250 | Section 3.5.2 Figure 3.10(a) |
| Ge 1ML adsorbed on $HfO_2$-termination | -1057.0007397 | Section 3.5.2 Figure 3.10(b) |
| Ge 1ML adsorbed on $HfO_2$-termination | -1056.9776272 | Section 3.5.2 Figure 3.10(c) |
| Ge 1ML adsorbed on $HfO_2$-termination | -1056.9730854 | Section 3.5.2 Figure 3.10(d) |
| Ge 1ML adsorbed on $SrO$-termination (most stable structure) | -1057.0070944 | Section 3.5.2 Figure 3.11 |
| Ge 1ML adsorbed on $SrO$-termination | -1057.0034639 | Section 3.5.2 Figure 3.12 |

| System | Total Energy (Hartree) | Details |
|---|---|---|
| Ge(001) diagonal-rows of surface dimers | -85.4075530 | Section 3.5.2 Figure 3.13(a) |
| Ge(001) straight-rows of surface dimers (stable structure) | -85.4089994 | Section 3.5.2 Figure 3.13(b) |
| Ge 2ML adsorbed on $SrO$-termination | -1073.2240081 | Section 3.5.2 Figure 3.14 |
| Ge 3ML adsorbed on $SrO$-termination | -1089.3875787 | Section 3.5.2 Figure 3.15 |
| Sb 1ML adsorbed on $SrO$-termination | -1063.6814410 | Section 3.7.3 Figure 3.16(a) |
| Sb 1ML adsorbed on $SrO$-termination (chain structure) | -1063.6628639 | Section 3.7.3 Figure 3.16(b) |
| Sb 2ML adsorbed on $SrO$-termination (epitaxial structure) | -1086.4381040 | Section 3.7.3 Figure 3.17 |
| Sr adatom at oxygen site on $SrO$-termination | -1072.0368921 | Section 3.8.1 |
| Sr adatom at bridge site on $SrO$-termination (barrier configuration) | -1072.0131369 | Section 3.8.1 |
| Sr 1/2ML adsorbed on $SrO$-termination (most stable structure) | -1103.1388025 | Section 3.8.2 Figure 3.18(a) |
| Sr 1/2ML adsorbed on $SrO$-termination | -1103.1303197 | Section 3.8.2 Figure 3.18(b) |
| Sr 1/2ML adsorbed on $SrO$-termination | -1103.0943267 | Section 3.8.2 Figure 3.18(c) |

| System | Total Energy (Hartree) | Details |
|---|---|---|
| Sr 1ML adsorbed on $SrO$-termination ($E_{slab}^{Sr+SrHfO_3}$) | -1165.3770087 | Section 3.8.3, and reference energy for Eqs. (3.5) and (3.6) |
| Sr 5/4ML adsorbed on $SrO$-termination (Sr adatom at hollow site) | -1196.4598881 | Section 3.8.4 |
| Sr 5/4ML adsorbed on $SrO$-termination (Sr adatom at bridge site) | -1196.4524850 | Section 3.8.4 |
| Sr 1ML with oxygen 1/4ML on $SrO$-termination with 1/4ML oxygen vacancies | -1165.3531527 | Section 3.9 Figure 3.20 |
| Ge adatom at hollow site on Sr 1ML + $SrO$ substrate | -1169.4717036 | Section 3.11.1 Figure 3.21 |
| Ge adatom at bridge site on Sr 1ML + $SrO$ substrate (barrier configuration) | -1169.3938906 | Section 3.11.1 |
| Ge adatom between Sr 1ML film and $SrO$ substrate | -1169.4102754 | Section 3.11.2 Figure 3.22 |
| Ge 1/2ML adsorbed on Sr 1ML + $SrO$ substrate (equilibrium structure) | -1173.5354498 | Section 3.11.3 Figure 3.23(a) |
| Ge 1/2ML adsorbed on Sr 1ML + $SrO$ substrate | -1173.5316031 | Section 3.11.3 Figure 3.23(b) |
| Ge 1/2ML adsorbed on Sr 1ML + $SrO$ substrate (dimer configuration) | -1173.4926779 | Section 3.11.3 Figure 3.23(c) |
| Ge 3/4ML adsorbed on Sr 1ML + $SrO$ substrate (equilibrium structure) | -1177.5846753 | Section 3.11.4 Figure 3.24(a) |
| Ge 3/4ML adsorbed on Sr 1ML + $SrO$ substrate | -1177.5721186 | Section 3.11.4 Figure 3.24(b) |
| Ge 3/4ML adsorbed on Sr 1ML + $SrO$ substrate | -1177.5714274 | Section 3.11.4 Figure 3.24(c) |

| System | Total Energy (Hartree) | Details |
|---|---|---|
| Ge 1ML adsorbed on Sr 1ML + $SrO$ substrate (Sr diffusion) | -1181.6584117 | Section 3.11.5 Figure 3.25 |
| Ge 1ML adsorbed on Sr 1ML + $SrO$ substrate (Sr diffusion) | -1181.6442642 | Section 3.11.5 Figure 3.26(a) |
| Ge 1ML adsorbed on Sr 1ML + $SrO$ substrate | -1181.6333921 | Section 3.11.5 Figure 3.26(b) |
| Ge 1ML adsorbed on Sr 1ML + $SrO$ substrate | -1181.6331034 | Section 3.11.5 Figure 3.26(c) |
| Ge 1ML adsorbed on Sr 1ML + $SrO$ substrate | -1181.6329861 | Section 3.11.5 Figure 3.26(d) |
| Ge 1ML adsorbed on Sr 1ML + $SrO$ substrate | -1181.6189262 | Section 3.11.5 Figure 3.26(e) |
| Ge 1ML between Sr 1ML film and $SrO$ substrate | -1181.5247405 | Section 3.11.5 Figure 3.27 |
| Ge 2ML adsorbed on Sr 1ML + $SrO$ substrate (Sr 1/2ML segregation) | -1197.8419843 | Section 3.12.1 Figure 3.28(a) |
| Ge 2ML adsorbed on Sr 1ML + $SrO$ substrate | -1197.8331567 | Section 3.12.1 Figure 3.28(b) |
| Ge 2ML adsorbed on Sr 1ML + $SrO$ substrate | -1197.8582247 | Section 3.12.1 Figure 3.29 |
| Ge 3ML adsorbed on Sr 1ML + $SrO$ substrate (Sr 1/2ML segregation) | -1214.0931079 | Section 3.12.2 Figure 3.30(a) |
| Ge 3ML adsorbed on Sr 1ML + $SrO$ substrate | -1214.0487816 | Section 3.12.2 Figure 3.30(b) |

# Curriculum Vitae

## Personal Data

Surnames: Reyes Huamantinco
First Name: Andrei
Citizenship: Peruvian
Place of Birth: Moscow, Russia
Date of Birth: 28 June 1975

## Contact

E-mail: andrei.reyes.huamantinco@tu-clausthal.de
Phone: +49-5323-722375
Fax: +49-5323-723116
Address: Institute of Theoretical Physics, Clausthal University of Technology, Leibnizstr. 10, D-38678 Clausthal-Zellerfeld, Germany

## Languages

Russian: Mother language (not spoken since 1980).
Spanish: Mother language.
English: High level. First Certificate in English, FCE, December 1995.
Portuguese: High level. Primeiro Certificado de Proficiencia em Lingua Portuguesa para Estrangeiros, CELPE-BRAS, October 2000 (First Certificate of Proficiency in the Portuguese Language for Foreigners). Master Thesis written in Portuguese.
German: Good understanding.

# Education

03.1981-12.1986: Elementary School in Lima, Peru.
03.1987-12.1991: Secondary School in Lima, Peru.
08.1992-07.1995: Faculty of Science General Studies at Pontificia Universidad Catolica del Peru.
08.1995-12.1997: Mechanical Engineering at Faculty of Science and Engineering, Pontificia Universidad Catolica del Peru (not finished).
03.1998-07.2000: Physics at Faculty of Science and Engineering, Pontificia Universidad Catolica del Peru.
Degree: Bachiller en Ciencias con Mencion en Fisica (Bachelor in Science specialized in Physics).
Graduated with honors on 30.01.2001.
09.2000-09.2003 Master studies at Instituto de Fisica da Universidade de Sao Paulo, Brazil.
Advisor: Helena M. Petrilli.
Scholarship: Bolsa de Mestrado da Fundacao de Amparo a Pesquisa do Estado de Sao Paulo, FAPESP (Processo: 2000/07538-6).
Thesis: "Estudo da Superficie Au(111) e da Adsorcao de $CH_3S$ em Au(111) atraves do Metodo PAW" (Study of the Au(111) surface and the Adsorption of $CH_3S$ on Au(111) through the PAW method), in portuguese.
Degree: Mestre em Ciencias - Area: Fisica (Master of Science - Area of study: Physics).
02.2004-present: PhD studies at Institute of Theoretical Physics, Clausthal University of Technology, Germany.
Advisor: Peter E. Blöchl.

# Professional Experience

02.2004-12.2006: Scientific employee for the European Project IST-ET4US, "Epitaxial Technologies for Ultimate Scaling".

# Research

Study of the Real Space Linear Muffin-Tin Orbital Atomic Sphere Approximation (RS-LMTO-ASA) and the Projector Augmented Wave (PAW) methods (Master studies).

Ab-initio study of the adsorption of CH3S, methanothiolate, on Au(111) using the PAW method (Master studies).
Ab-initio study of the $SrHfO_3/Ge(001)$, $SrTiO_3/GaAs(001)$, $La_2Hf_2O_7/Si(001)$ interfaces, and determination of suitable band offsets for transistor applications by variation of the interfacial composition; with the PAW method (PhD studies).
Theoretical study of the epitaxial growth of Ge on $SrHfO_3(001)$ by means of a surfactant through Kinetic Monte Carlo simulations and the PAW method. Programming of the Kinetic Monte Carlo code, in progress (PhD studies).

## Teaching

08.1998-07.2000: Instructor for the courses (not simultaneously) "Electromagnetism", "General Physics 4", "Laboratory for General Physics 4", "Laboratory for General Physics 3" at the Faculty of Science and Engineering, Pontificia Universidad Catolica del Peru.

## Visits

29-30 March 2007: Laboratorio MDM-INFM, Materials and Devices for Microelectronics, Milan, Italy.
17 September 2007: IBM Laboratory, Zurich, Switzerland.

## Seminars, Workshops and Conferences

XXV Encontro Nacional de Fisica da Materia Condensada, Caxambu, Brazil, 7-11 May 2002.
Poster: "Superficies Metalicas atraves de Calculos Ab-Initio".
VII Escola Brasileira de Estrutura Eletronica, Juiz de Fora, Brazil, 14-18 July 2002.
Poster: "Calculos de Dinamica Molecular Ab-Initio de Au(111) e de CH3S Adsorvido em Au(111)".
Workshop "Dünne Filme und Oberflächen" der TUC, Clausthal-Zellerfeld, Germany, 07 July 2006.
Talk: "Ab-initio Simulation of the Epitaxial Growth of a Semiconductor on a Crystalline Oxide".

1. Harzer Ab Initio Workshop, Clausthal-Zellerfeld, Germany, 23-25 October 2006.
Talk: "Ab-initio Study of the Epitaxial Growth of Ge on SrHfO3(001) Using Sr as Surfactant".
Deutschen Physikalischen Gesellschaft Conference, Regensburg, Germany, 26-30 March 2007.
Talk: "Ab-initio Study of the Epitaxial Growth of Germanium on SrHfO3(001) Using Strontium as Surfactant".
Laboratorio MDM-INFM, Milan, Italy, 29 March 2007.
Seminar: "Ab-initio Study of the Epitaxial Growth of Ge on SrHfO3(001) Using Sr as Surfactant".
National Center on nanoStructures and bioSystems at Surfaces (S3) of INFM-CNR, Modena, Italy, 2 April 2007.
Seminar: "Ab-initio Study of the Epitaxial Growth of Ge on SrHfO3(001) Using Sr as Surfactant".
IBM Laboratory, Zurich, Switzerland, 17 September 2007.
Seminar: "Epitaxial Growth of Ge on SrHfO3(001) Using a Surfactant".
2. Harzer Ab Initio Workshop, Goslar, Germany, 15-17 October 2007.
Talk: "Epitaxial Growth of Ge on SrHfO3(001) Using a Surfactant for MOSFET applications".

# Invited Talks

3rd International Conference on Diffusion in Solids and Liquids, DSL-2007, Algarve, Portugal, 4-6 July 2007.
Title: "Enabling Epitaxial Growth of Ge on a High-K Oxide by Means of a Surfactant: An Ab-Initio Study".

# Publications

## International Journals

G. Seguini, S. Spiga, E. Bonera, M. Fanciulli, A. Reyes Huamantinco, C. J. Först, C. R. Ashman, P. E. Blöchl, A. Dimoulas and G. Mavrou, "Band Alignment at the La2Hf2O7/(001)Si interface", *Appl. Phys. Lett.* **88**, 202903 (2006).

### Master Thesis

"Estudo da Superficie Au(111) e da Adsorcao de $CH_3S$ em Au(111) atraves do Metodo PAW", Universidade de Sao Paulo, Brazil, September 2003.

## Other Interests

Painting/Installation: Contributions to the TUC Students' Art Exhibition, June-August 2006, Clausthal-Zellerfeld, Germany.
Music: Percussion.
Basketball: Member of school and university teams (local league) in Lima, Peru.
Water sports and rock climbing.

# Papers

"Band alignment at the $La_2Hf_2O_7$/(001)Si interface" G. Seguini, S. Spiga, E. Bonera, M. Fanciulli, A. Reyes Huamantinco, C. J. Först, C. R. Ashman, P. E. Blöchl, A. Dimoulas and G. Mavrou, *Appl. Phys. Lett.* **88**, 202903 (2006)